FRACTURE ANALYSIS OF CIRCUM-BIGHORN BASIN ANTICLINES,

WYOMING-MONTANA

by

Julian Stahl

A thesis submitted in partial fulfillment
of the requirements for the degree

of

Master of Science

in

Earth Science

MONTANA STATE UNIVERSITY
Bozeman, Montana

November 2015

DEDICATION

I dedicate this thesis to my brother, Manuel Stahl, who provided me with the inspiration and drive to pursue a degree that I am truly passionate about.

ACKNOWLEDGEMENTS

The research presented in this document would not have been as thought-provoking and thorough without the help of my mentors and peers. My advisor, Dr. David Lageson helped formulate the project idea and was fundamental throughout the course of my study in leading me in the right direction and always being available to answer questions. I would also like to extend my gratitude to my committee members, Dr. Colin Shaw and Dr. Jean Dixon, for providing me with the necessary assistance and expertise.

I would also like to thank my fellow geology peers at Montana State University. Without the constant communication and discussions with Mr. Jacob Thacker, Mr. Travis Corthouts and Mrs. Anita Moore-Nall this project would not have come to fruition. I would also like to offer my sincere appreciation to my two field assistants, Mr. Evan Monroe and Miss Amy Yoder, for taking the time out of their lives to help unravel the geology of the Bighorn Basin in the field.

I would like to express my gratitude to my entire family, Dr. Johannes Stahl, Ms. Gabriele Stahl and Mr. Roman Stahl, for supporting me and giving me inspiration to pursue my passion for geology throughout my undergrad and graduate career.

This project would not have been possible without the financial support of Rocky Mountain Association of Geologists, Tobacco Root Geological Society, American Association of Petroleum Geologists, and Montana Geological Society.

TABLE OF CONTENTS

TABLE OF CONTENTS - CONTINUED

TABLE OF CONTENTS - CONTINUED

LIST OF TABLES

LIST OF FIGURES

LIST OF FIGURES – CONTINUED

LIST OF FIGURES – CONTINUED

ABSTRACT

The Bighorn Basin (BHB), Wyoming-Montana, is an oval Laramide intermontane basin (80-45 Ma) in the Rocky Mountain foreland province. Regional thrust and backthrust faults related to the Laramide orogeny uplifted basement rocks around the basin forming the present Beartooth, Bighorn and Owl Creek Mountains. Within the basin, weak Paleozoic stratigraphy succumbed to the same regional shortening, transforming the once sub-horizontal strata into a series of thrust fault related anticlines around the basin margin. Due to the oblique orientation to Laramide shortening direction of anticlines at the north and south side of the BHB, this study examines local stress regimes through Google Earth Pro lineament analysis and ground trothing these measurements with outcrop fracture analysis. Both lineament and fracture orientations were collected at nine anticlines around the basin shoulder and classified based on their relationship to the hinge line of the anticline: dip (AC), strike (BC) and oblique fractures and lineaments. Data collected was analyzed through a combination of rose diagrams and stereonets to classify the orientations of lineaments and fractures in each anticline. Results indicate that the orientation of the three lineament and fracture sets are strongly influenced by the orientation of the fold axis. Based on the results, the BHB can be divided into two tectonic domains. The first tectonic domain, anticlines adjacent to the east and west side of the basin, displays an average fold axis trend of 154°, aligning well with the suggested Laramide shortening direction of 060° N. Tectonic domain two is situated at the southern extent of the basin and defined by Thermopolis anticline. This domain shows strong influence of the Owl Creek Mountains sinistral accommodation zone to the south by the counterclockwise rotation of the anticline hinge line to 114°. The new anticline orientation is clearly oblique to the Laramide shortening direction and determined by a more local stress regime. Fracture orientations within this anticline also display a counterclockwise rotation indicating the strong relationship to the hinge line trend mentioned above. Overall, the orientations of Laramide structures identified in this study align well with previous research across the Rocky Mountain foreland.

INTRODUCTION

Bighorn Basin, Wyoming-Montana

The Bighorn Basin (BHB), Wyoming-Montana has been studied, mapped and interpreted in published literature since the early work of Eldridge (1893,1894), Fisher (1906), Darton (1906), Dake (1918) and Hewett (1926) up to the present day due to its complex structure, hydrocarbon resources, and sparse uranium and thorium deposits (Harris 1983; as cited in Blackstone, 1986). In map view it is an oval Laramide intermontane basin (80-45 Ma) within the Rocky Mountain foreland province, located mainly in north-central Wyoming with its northern extent reaching into south-central Montana. Its sinuous basin axis trends over 220 km approximately NW-SE, with the basin width extending over 100 kilometers E-W. Overall, the BHB is asymmetric with the thickest succession of over 7000 meters of Cambrian to Eocene sedimentary rocks along the western edge of the basin (Blackstone, 1986; Beaudoin, 2012). It is bounded on all sides by Laramide-age basement arches: the Bighorn Mountains to the east, the Owl Creek/Bridger Mountains to the south, the eastern extent of the ancestral Teton-Gros Ventre uplift/ Buffalo Fork uplift to the west, the Beartooth Mountains to the northwest, the Nye-Bowler lineament to the north, and the Pryor Mountains to the northeast (Figure 1).

During the Laramide orogeny, the central Rocky Mountain region experienced a general NE-SW (040°-055°) transpressional strain regime, widely interpreted to be the result of the low-angle subduction of the Farallon plate along the western margin of the North American plate (Blackstone, 1986; Bird, 2002; Neely, 2009). Early authors

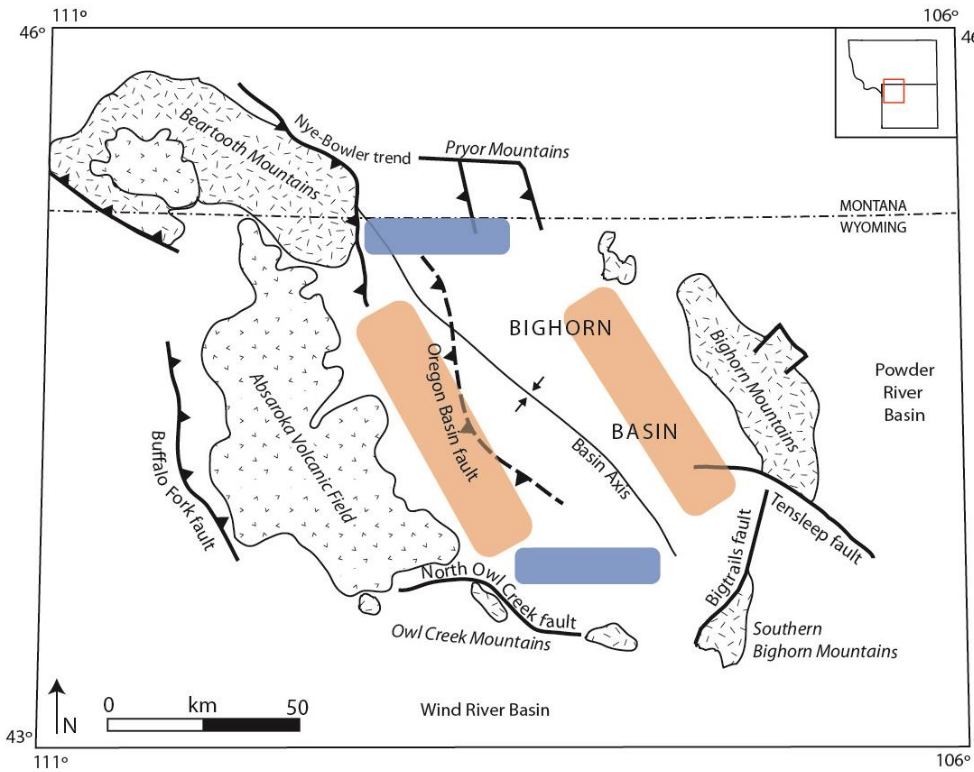

Figure 1: Simplified tectonic map of the Bighorn Basin. Orange areas indicate tectonic domain 1 adjacent to northwest trending Laramide thrust faults. Blue areas indicate tectonic domain 2 adjacent to transpressional accommodation zones. Tertiary Absaroka volcanics cover the Laramide Washakie uplift along the western boundary of the Bighorn Baisn. See the section on research objectives for an explanation of the significance of these domains. Modified from Blackstone (1986).

described the overall structural geometry of general Laramide uplifts as non-crustal shortening piston-like basement uplifts with drape folds or upthrusts due to vertical uplift or wrench faulting (Chamberlain, 1945, Thom, 1947; Berg, 1965; Sales, 1968; Sterns, 1975; Weinberg, 1979). More detailed research based on field mapping, balanced cross-sections and seismic reflection profiles revealed that crustal shortening occurred via thrust and fold-thrust uplifts along basement-cored arches with up to over 10 kilometers of heave separation (Foose, 1961; Keefer and Love, 1963; Berg, 1965; Sterns, 1975; Weinberg, 1979; Blackstone, 1986; Brown, 1993, Neely, 2009). A detailed description of the evolution of thinking on uplift geometry and kinematics for the Laramide province is presented in Chapter 2. These thrusts and related antithetic back-thrusts deformed the overlying Paleozoic and Mesozoic sedimentary successions into a series of synclines and anticlines that occurred along the shoulder of the BHB (Figure 2). The anticlinal structures acted as secondary traps for hydrocarbons in Pennsylvanian-Permian and Early Cretaceous-Paleocene reservoir rocks (Nuccio & Finn, 1998; Finn et al., 2010). Different from the folded margin, the interior of the basin contains sub-horizontal Eocene and Paleocene sedimentary strata (Figure 3).

Research Objectives

Past structural research on the BHB focused on large-scale tectonic features associated with Laramide basement-cored uplifts and bounding faults, resultant folding of overlying strata, and major transverse basin faults associated with adjacent uplifts (Sterns, 1975; Brown, 1993; Bird, 1998; Fiore, 2006; Neely, 2009). Over studies of the Nye-Bowler Lineament, Oregon Basin, Owl Creek, Fivemile, Tatman, Rio, and Tensleep faults provide additional information on the basin-wide tectonic regime (Stone, 2004). Detailed structural studies on small regions within the BHB, such as Rattlesnake Mountain and Sheep Mountain anticline, have yielded valuable insight on confined strain regimes, fracture timing and fluid migration based on comprehensive fracture analyses (Bellahsen et al., 2006; Fiore, 2006; Beaudoin et al., 2011, 2012). The research conducted

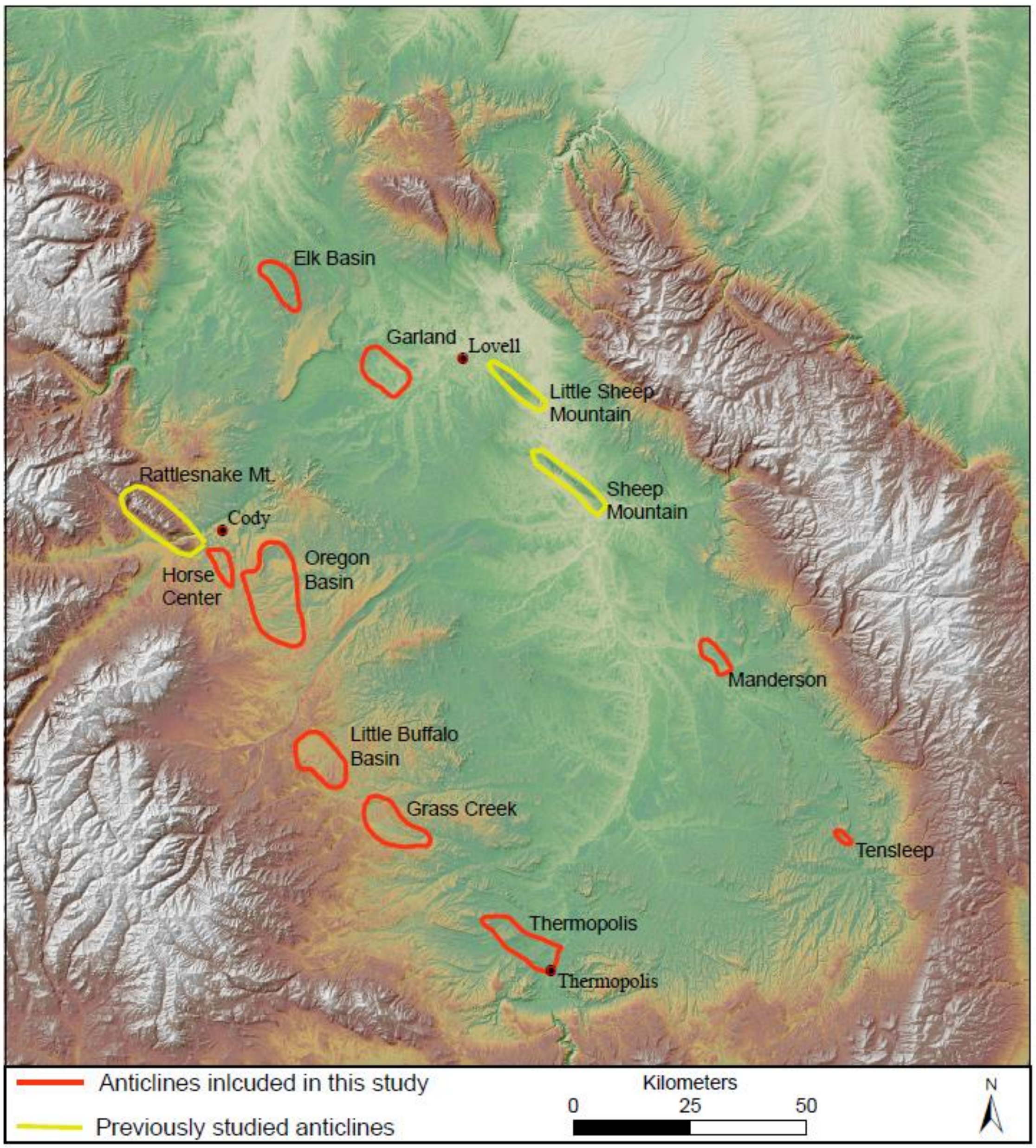

Figure 2: Regional digital elevation model overlain on a hillshade showing anticlines examined in this study (red) and anticlines studied by others for fracture analysis (yellow). Cities shown for geographic reference.

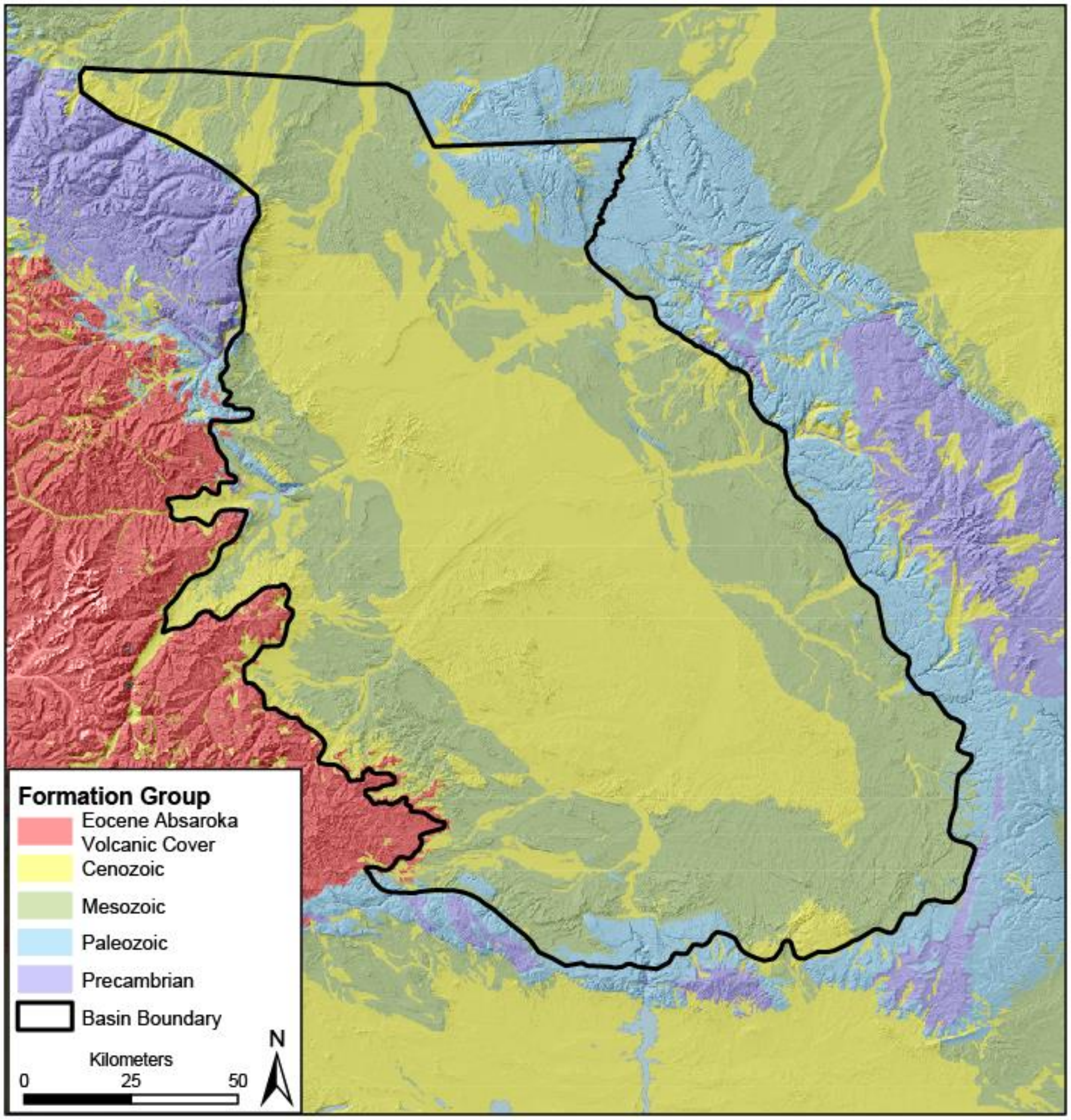

Figure 3: Generalized geologic map of the Bighorn Basin. Black line represents the basin boundary as defined by the United States Geological Survey (Finn et al., 2010). Geology data provided by Wyoming State Geological Survey and Montana Bureau of Mines and Geology.

in this study investigates fracture sets on a basin-wide scale in order to identify possible structural domains within the basin. This intermediate-scale research is important to gain an understanding how different areas within the basin accommodated shortening in an overall transpressive environment. Both Chamberlain (1945) and Brown (1993) suggest that the BHB may be structurally compartmentalized, rather than a cohesive basin, as related to hydrocarbon production. The research agenda in this study further evaluates this idea.

The geometry and orientation of the BHB with respect to the inferred Laramide shortening direction suggests two possible structural domains (Figure 1): (1) domain #1 adjacent to the east and west basin margin (Bighorn Mountains and Absaroka volcanics, respectively) and (2) domain #2 associated with the transpressive, sinistral accommodation zones to the north and the south (Nye-Bowler lineament and Owl Creek Mountains, respectively). These two domains may be further subdivided into smaller subdomains by inter-basin faults (e.g., Tensleep fault, Oregon Basin and Rio thrust fault). By conducting a basin-wide lineament and fracture analysis on basin shoulder anticlines, this research seeks to identify these domains based on fracture style, type and orientation.

Research Questions

This study is designed to investigate the Bighorn Basin in northern Wyoming and southern Montana through systematic fracture analyses of circum-basin anticlines (Figure 2). The BHB is oblique to the inferred regional direction of Laramide shortening (040°-050°) across the central Rocky Mountains and is bounded to the north and south by transverse, sinistral accommodation zones (Brown, 1993). However, as Neely (2009) and Erslev and Koenig (2009) suggest, the northern extent of the Laramide orogeny most likely followed an 060°N shortening direction based on eigenvalues calculated from minor fault kinematics adjacent to the Beartooth Mountains, placing the BHB more perpendicular to the shortening direction. Therefore, the overarching research question is: *Did the BHB act as a structurally cohesive basin during regional Laramide shortening, or was it partitioned into structural domains displaying distinct fracture orientations and sets that reflect obliquity to regional shortening?*

Supporting questions:

1. Do faults, fractures, veins, and R/R'-shears on basin-margin anticlines consistently display orientations compatible with the Laramide stress model with sigma 1 oriented NE-SW (approximately 040°-060°N), as accepted in existing literature (Brown, 1993, Neely, 2009) (Figure 4), or do these structural elements vary in orientation across the suggested tectonic domains?

2. How do the sinistral accommodation zones (domain 2) of the Nye-Bowler lineament in the north and the Owl Creek fault system in the south affect fracture distribution in proximal anticlines versus anticlines along the east-west domains of the basin (domain 1)? Do domain 2 fractures display a counterclockwise rotated trend in comparison with domain 1 due to local sinistral strain

Previous Work

The BHB has been of economic importance since the start of the 20th century after the theory of anticlines as oil-bearing traps became widely tested across the Rocky Mountain foreland (Hunt, 1861; White; 1885). The first quarter of the 20th century mainly involved simple geologic mapping and cross-section construction of basin margin anticlines, with minimal sub-surface correlation from exploration well data. By the mid-19th century, geologists began examining the larger picture of Laramide deformation in order to unravel the tectonic history and further understand the geometry and kinematics of the

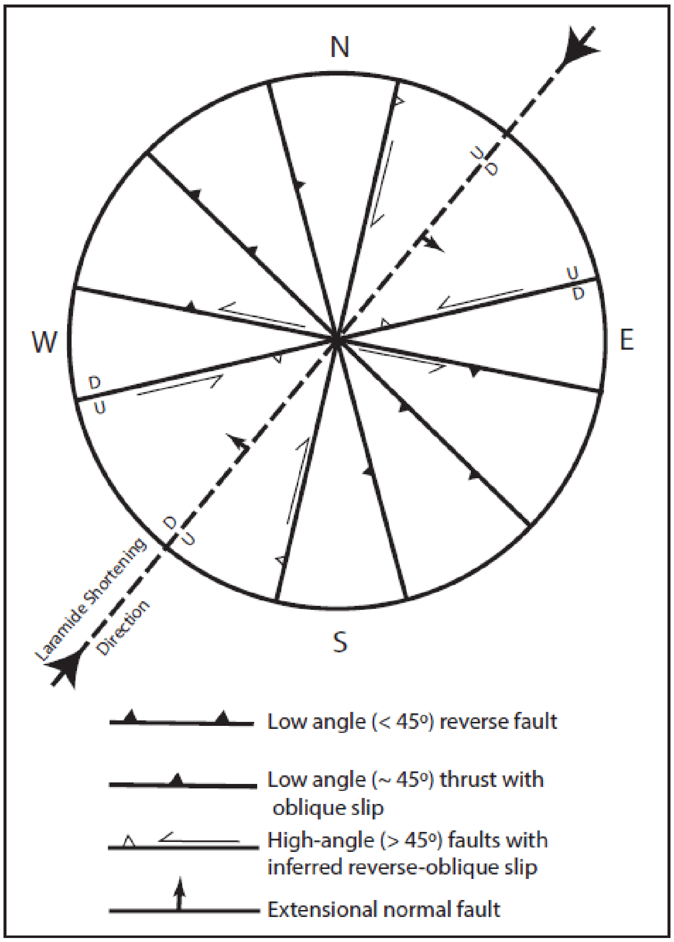

Figure 4: Expected Laramide stress field. Laramide shortening direction (NE-SW) is indicated by the through-going dashed line. Solid black lines within the circle represent the geometry and kinematics of Laramide structures (e.g. faults and fractures). Modified from Brown (1993).

economic anticlines (Chamberlain, 1945). Although early models seemed relevant at the time, increased 2D/3D seismic coverage and higher density well data provided the underlying evidence for the accepted model of Erslev (1991) and Mitra and Mount

(1998). Following Erslev's (1991, 1993) tri-shear zone model explaining the formation and interplay of thrusts and back thrusts, authors have focused their research from studying macroscale to microscale structures and relating them back to the regional tectonic framework. The majority of present day research in the BHB consists of detailed outcrop fracture analysis, calcite paleopiezometry stress and strain rates, and cross-section construction and balancing based on seismic and well data (Fellaheen et al., 2006; Beaudoin et al., 2011; Beaudoin et al., 2012). However this newer research has been largely restricted to two major anticlines, Rattlesnake Mountain and Sheep Mountain anticlines due to their excellent outcrop exposure and relatively easy accessibility.

Research Importance

The research conducted for this thesis extends the outcrop fracture analysis across the entire shoulder of the BHB. Whereas both Rattlesnake and Sheep Mountain anticline have been extensively studied, they provide only a glimpse at the bigger picture of the BHB at spots on the west and east side of the basin, respectively. The anticlines studied both remotely (Google Earth Pro) and in the field for this study include: Elk Basin, Horse Center anticline, Oregon Basin, Little Buffalo Basin, Thermopolis anticline, Manderson anticline, Garland Basin, Tensleep anticline, and Grass Creek (Figure 2). These anticlines fill the gaps on the north and south margins of the basin, as well as providing more fracture outcrop data on the west and east margins. Due to the large number of anticlines covered, analysis is mainly based on fracture geometry with only minimal control from kinematic data, as the latter was often not available due to weathering and the nature of exposures.

GEOLOGIC SETTING

Regional Stratigraphy

Paleozoic

The Paleozoic stratigraphy across the BHB regionally follows the general transgressive and regressive trends of the Sloss Sequences (Figure 5) (Finn et al., 2010). During the Cambrian and Ordovician the Sauk sea was transgressing to the east, depositing sequences of sandstone, shale, limestone and dolomite, due to regional subsidence of western North America (Thomas, 1949). These formations include the Flathead Sandstone, Gros Ventre (shale), Gallatin Limestone and Bighorn Dolomite. Following the Ordovician, Wyoming was mainly emergent resulting in thin sedimentary deposits of which none are preserved today due to basin tilting and subsequent erosion. In the Devonian, thin stratigraphic sections of the Three Forks shale were deposited in northwestern Wyoming. After this, the entire state was widely submerged with deposition of the well-known Madison Limestone across the Rocky Mountain region (Thomas, 1949). Following deposition and erosion of the Madison Limestone, the Pennsylvanian Amsden and Tensleep Formations were deposited, thickening towards the southwest in the BHB mainly due to post-Pennsylvanian erosion of the Tensleep in the northeast. During the Permian, much of Wyoming was submerged which deposited the Phosphoria Formation through a series of sea level highstands and lowstands. On the eastern side of the basin, black shales of the Phosphoria Formation were deposited that provide a valuable source of petroleum in many of the closed anticlinal structures across the basin.

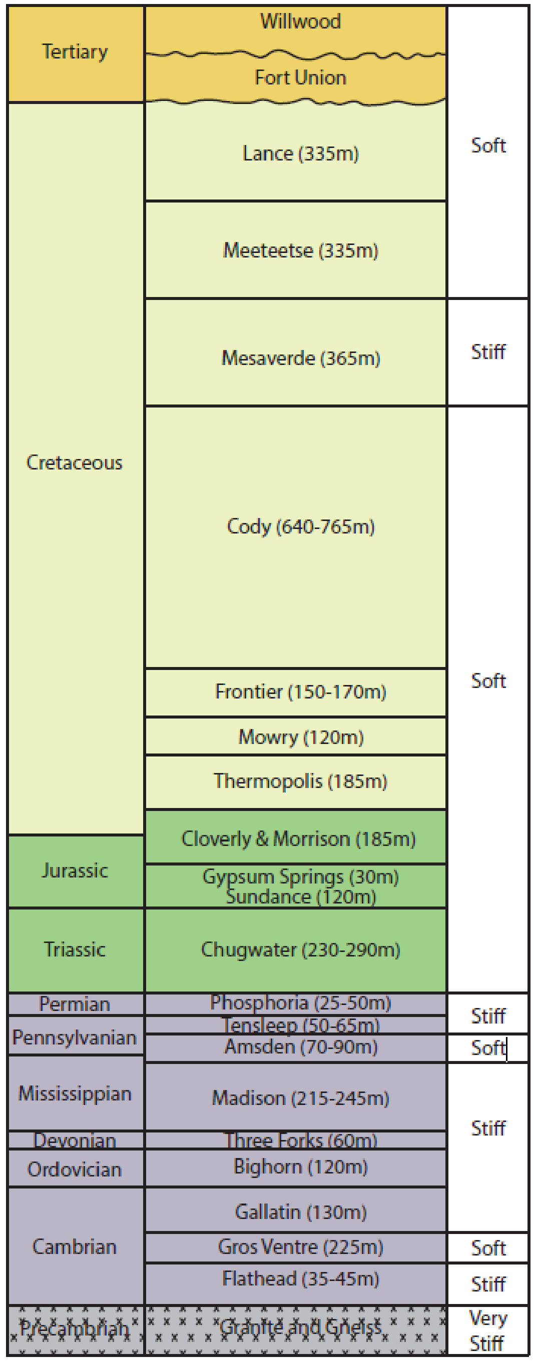

Figure 4: Stratigraphic column of the west flank of the Bighorn Basin. Relative competency based on lithology displayed in right column. Modified from Durdella (2001).

Triassic and Jurassic

Red bed deposition during the Triassic is represented by the red siltstone and shale beds of the Dinwoody and Chugwater Formations. Both of these units produce hydrocarbons in the Grass Creek, Hamilton Dome and Oregon Basin fields. Basin tilting to the southwest resulted in erosion of the units to the northeast. During the Middle Jurassic, the area that would become the BHB was again submerged beneath a shallow sea, depositing the evaporate and red-shale beds of the Gypsum Spring Formation, overlain by interbedded sets of marine sandstone, limestone and shale of the Sundance Formation.

Cretaceous

Throughout the Cretaceous Period, the Rocky Mountain foreland is defined by the stratigraphy of the Western Interior Seaway (WIS), which at its maximum extended from the Arctic Ocean to the Gulf of Mexico. The formation of the WIS resulted from both eustatic sea level rise and foreland basin subsidence to the east of the active Western Cordillera highlands (Finn et al., 2010). The transgressive/regressive cycles of the WIS deposited over 4000 feet of intertonguing marine, marginal marine, and nonmarine deposits (Cloverly, Thermopolis Shale, Muddy Sandstone, Mowry Shale, Frontier, Cody Shale, Mesaverde, Meeteetse and Lance Formation). Through most of the Cretaceous these deposits were wide spread over Wyoming. At the start of Maastrichtian time, the Laramide orogeny began structurally partitioning the region into smaller sub-basins, like the BHB, by a network of interconnected basement arches. The increased uplift rate and compartmentalization of basins resulted in high erosion and subsequent deposition rates of coarse clastic material (Finn et al., 2010).

Cloverly Formation. Because the early-middle Cretaceous rocks were the main focus of outcrops studied for fracture analysis in this thesis, a more elaborate description follows. The basal member of the Cretaceous stratigraphic sequence is the Cloverly Formation. It consists of interbedded sandstone, shale and claystone and in northern parts of the basin is defined by a basal conglomerate. In other regions of the BHB, thick sections of shale interbedded with thin sandstone beds presumably deposited in a flood-plain, fluvial and lacustrine environment defines the base of the Cloverly Formation. The Greybull Sandstone Member overlays the base and consists of a 5 to 70 feet thick medium sandstone that defines the initial marine transgression of the Western Interior Seaway (Keefer et al., 1998; Finn et al., 2010). The top of the Cloverly Formation are referred to as the "Rusty Beds Member" consisting of finely laminated siltstone and shale formed on a tidal flat. Some authors combine this unit with the overlying Thermopolis Shale in certain regions of the basin (Mills, 1956; Eicher, 1962).

Thermopolis Shale. The Thermopolis Shale displays continuing sea-level rise and deposition of marine shale and siltstone across the basin. The contact with the underlying Cloverly Formation is gradational (Finn et al., 2010). Thin beds of sandy claystone and bentonite are also present regionally. The upper contact varies between unconformable or gradational with the overlying Muddy Sandstone.

Muddy Sandstone and Mowry Shale. The Muddy Sandstone is a 7 to 125 feet thick section of mainly sandstone with sparse sections of mudrock. It is thickest in the southeast of the basin and thins to the north-northwest (Finn et al., 2010). The depositional environment is generally interpreted as a complex valley-fill succession. Recent cores indicate both freshwater and marine sediment deposition.

The lower section of Mowry Shale is lithologically similar to the Thermopolis Shale, thus some authors have lumped the two into the Thermopolis Shale unit (Mills, 1956; Haun & Barlow, 1962). Unlike the lower section, the upper Mowry shale defines a 240 to 400 feet thick hard siliceous shale.

Frontier Formation. The Frontier Formation is interpreted to be deposited in a deltaic or shoreface environment evident by its package of marine sandstone, siltstone and shale. It ranges in thickness from 450 feet in the western part of the BHB to 1,075 feet in the southeastern part. This unit contains at least six major sandstone beds with a maximum bed thickness of 130 feet providing good outcrops for fracture measurements (Finn et al., 2010). However, the six beds are never found in a single stratigraphic section since they are locally truncated by erosion on marine-flooding surfaces.

Cody Shale. The Cody Shale is mainly a thick (1,700 to 3,800 feet) section of marine shale deposited during a major marine transgressive-regressive cycle. The base of the Cody Shale commonly consists of homogenous shale, but at higher stratigraphic levels increasing amount of interbedded sandstone appear. Unlike the sandstone intervals in the Frontier Formation, sandstone beds within the Cody Shale can be traced laterally for many miles. Some sandstone beds exhibit hummocky cross-bedding suggesting a nearshore marine origin (Finn et al., 2010).

Mesaverde Formation. The Mesaverde Formation consists of three main units: lower member, middle or main part, and the Teapot Sandstone Member. The lower member conformably overlies and interfingers with the underlying Cody Shale. In general the sequence of beds within the Mesaverde Formation indicates the retreat of the Cretaceous sea to the east across the BHB. The basal member defines the regression of the sea and consists of marginal marine sandstone. The rest of the Mesaverde Formation section consists of non-marine sandstone, siltstone, shale and carbonaceous shale. The formation generally thickens from east to west with the member and Teapot Sandstone Member reaching a thickness of 1,200 feet (Finn et al., 2010).

Meeteetse Formation. The Meeteetse Formation defines a marginal marine to nonmarine depositional environment depositing intertonguing very fine to medium-grained sandstone, siltstone, and shale. It consists of the main Meeteetse Formation body, as well as the Lewis and Bearpaw Shale Members. Maximum thicknesses of 1,000+ feet occur as localized depocenters within the BHB at the northern and southwestern end of the basin. Regionally, the formation exceeds a thickness of 500 feet.

Regional Structural Geology

Sevier and Laramide Orogenies

The Mesozoic was a time of intense mountain building and crustal deformation across the Rocky Mountain region. Starting in the late Jurassic (164-145 Ma) through the early Cretaceous (145-100 Ma), the Sevier orogeny resulted in tectonic transport of large thrust sheets relatively to the east along Proterozoic and lower Paleozoic zones weaknesses, due to increasingly low-angle subduction of the Farallon Plate along the western margin of the North America Plate. The style of deformation associated with the Sevier orogeny is termed “thin-skinned” as Precambrian basement rocks were not involved in the process, except in hinterland areas (Figure 6A). Thrusts tend to have a ramp-flat geometry and are locally stacked, with a basal décollement in the lowermost Cambrian shale. The local region affected by the Sevier orogeny mainly consists of southeast Idaho, western Montana, western/central Utah, and western Wyoming (Armstrong, 1968; Decelles & Mitra, 1995).

Following the Sevier orogeny and overlapping it both spatially and temporally, was the start Laramide orogeny, beginning in the late Cretaceous (100-66 Ma) and persisting through the Eocene (56-50 Ma). Unlike the Sevier-style deformation, the Laramide is defined by basement involved thrust and reverse faults resulting in a “thick-skinned” deformation (Figure 6B). This change in mechanisms is also related to the thickness and nature of rocks involved. Whereas the Sevier orogeny involved thick sequences of sedimentary sequences, as the stress translated to the east, the sedimentary section thinned, resulting in involving the Precambrian basement (Lowell, 1983). The

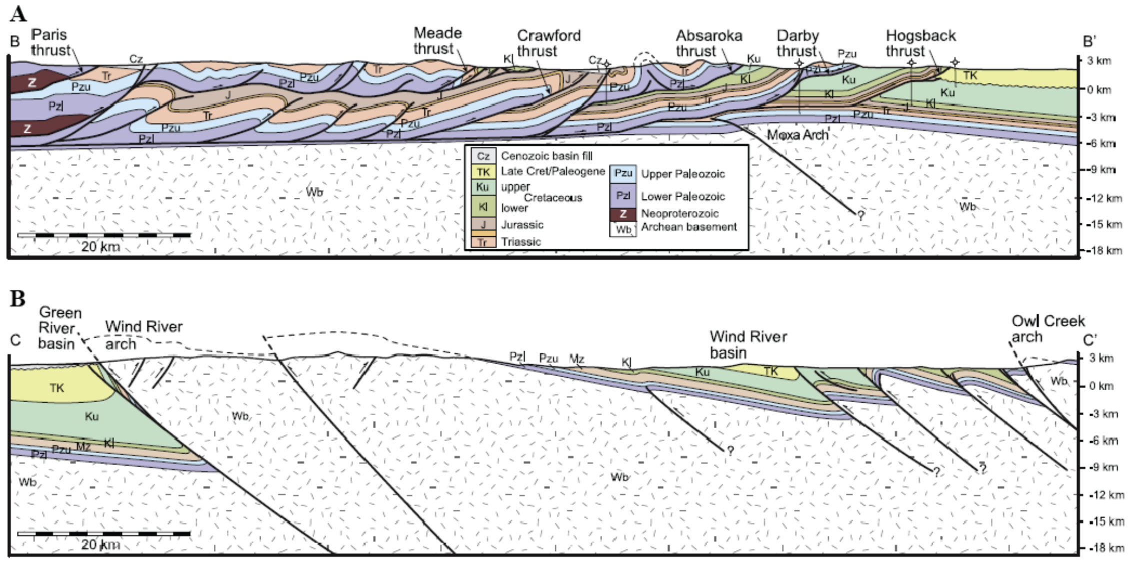

Figure 6: Structural cross-section comparisons of the Sevier (B) and Laramide (C) styles of deformation. B) Section line traverses from east-central Idaho into west-central Wyoming. C) Section lies perpendicular to the Wind River arch. Laramide style is dominantly thick-skinned deformation with sparse thrust faults detaching in Paleozoic shale units. Modified from Weil and Yonkee (2012).

change from the thin-skin Sevier fold-thrust belt to the thick-skin Laramide foreland deformation is suggested by a change of subduction mechanics of the Farallon plate. During the Sevier orogeny the subduction of relatively young oceanic lithosphere likely reduced the rate of trench rollback leading to increased coupling between the subducting plate and the North American Plate at the subduction zone (Weil & Yonkee, 2012). This formed a hinterland plateau and regional thickening of the lower crust that was balanced by the Sevier fold-thrust belt to the east. An increased asthenospheric flow, coupled with higher trench suction underneath the North American Plate, further decreased the slab dip. This modified subduction mechanism increased compressive stresses across the western North American Plate and transmitted shortening further inland, ultimately leading to the flat-slab subduction required for Laramide thick-skin deformation. As the subducting slab cooled, it also increased basal traction aiding in long distance stress transfer across the mantle lithosphere. The stress concentration seems to be focused across the thick Archean cratonic keel of Wyoming. Evidence for flat-slab subduction is identified by a rapid eastward migration of the volcanic arc, as well as eclogite xenoliths incorporated in some of the volcanic centers. These xenoliths are thought to originate from the underlying oceanic lithosphere (Usui et al., 2003). Also, the Farallon Plate has been tomographically imaged beneath the eastern United States (Pavlis et al., 2012).

Foreland Basins of the Rocky Mountain Region

The basement-involved thrust blocks of the Laramide created a series of anastomosing arches throughout the Rocky Mountain foreland. Some of the arches are culminations and define high topographic features (e.g. Beartooth, Owl Creek and Bighorn Mountains), whereas their adjacent lower amplitude saddles reside underneath younger strata and are not exposed at the surface today (e.g. Casper arch) (Erslev, 1993) (Figure 7). This network of arches segmented the previously regionally extensive foreland province into various local basins that became sediment traps (Dickinson et al., 1988; Yin and Ingersoll, 1997). The basins were categorized by Dickinson et al. (1988) into three classes; perimeter basins, axial basins and ponded basins. Perimeter basins define eastern, broad basins that are drained by fluvial systems into the Great Plains (e.g. Powder River and Denver Basin). Axial basins extend in a north-south trending fashion and are coincident with the trend of the younger Rio Grande Rift (e.g. Laramie Basin). Lastly, the ponded basins define the western most basins enclosed by Laramide arches

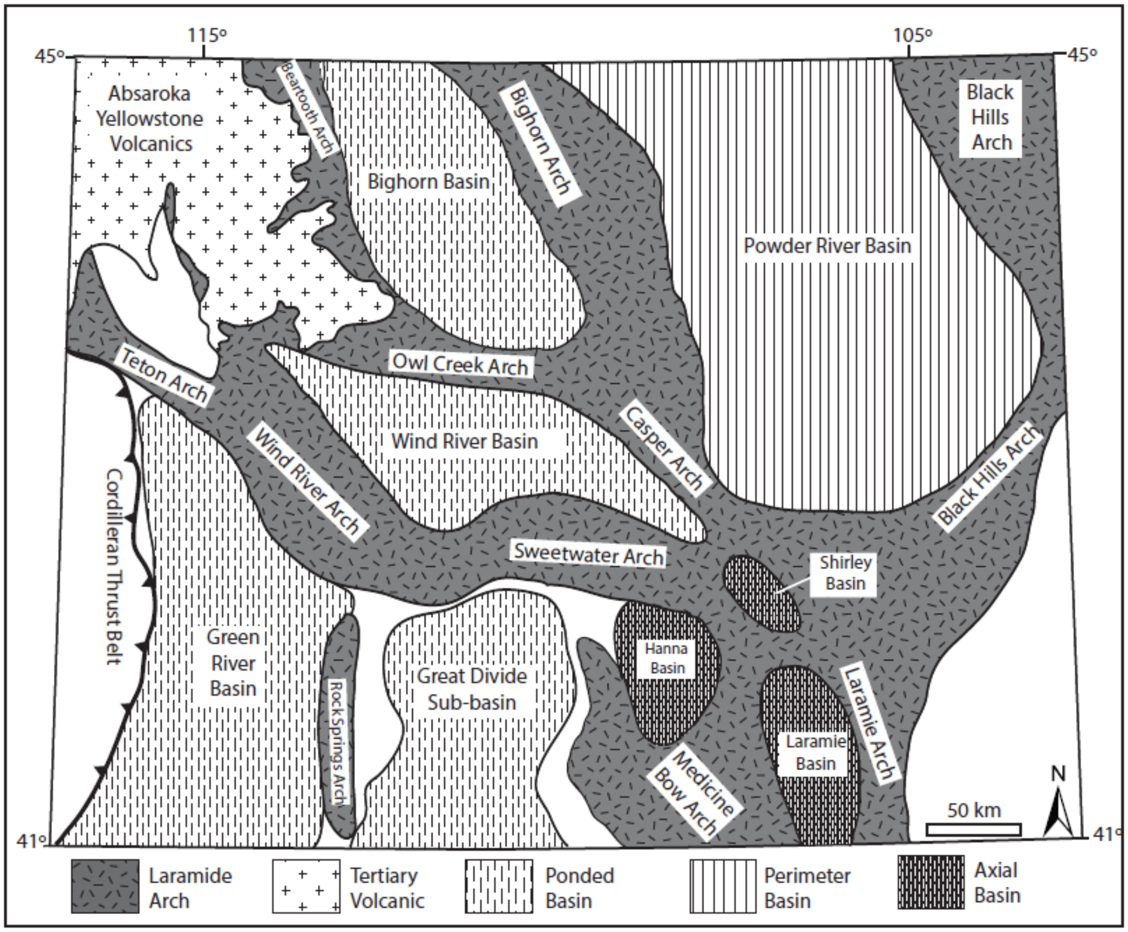

Figure 7: Laramide arches in the central Rocky Mountains of Wyoming and distinguishing types of basins as defined by Dickinson (1988). Locations of Laramide arches taken from Erslev (1993).

and were mainly occupied by lakes that trapped the sediment within the basin (e.g. Bighorn Basin, Wind River Basin, Uinta Basin).

<u>Bounding Tectonic Structures of the Bighorn Basin</u>

Although the regional compressive stress was likely oriented NE-SW (040°-060°) during the Laramide orogeny and many of the thrusted arches are sub-perpendicular to this orientation (e.g. Beartooth and Bighorn Mountains), some east-west trending arches formed along sinistral accommodation zones through transpressive motion (e.g. Owl Creek Mountains). The Beartooth Mountains were uplifted along the west-dipping frontal Beartooth thrust fault system along the eastern flank of the range, with up to 20,000 feet of dip-separation recorded and along the northeast dipping Gardner thrust on the southwest flank of the range (Foose et al., 1961). On the eastern side of the BHB the Bighorn Mountains are bounded on the west side by a system of east-dipping backthrusts (Five Springs fault) as a result of the main west-dipping Bighorn eastern boundary thrust (Stone, 1993; Crowley et al., 2002). Different from eastern and western boundary, the southern margin of the basin is marked by the Owl Creek Mountains transpressive accommodation zone. A positive flower structure with several sub-parallel, sinistral, oblique-slip faults accommodated the transpressive motion on the adjacent Black Mountain thrust and Mud Creek thrust (Stone, 1993; Paylor & Yin, 1993). Similar to the Owl Creek Mountains, the Nye-Bowler lineament defines the northern boundary of the BHB and is also a sinistral accommodation zone. Although it has been largely neglected in recent research, Wilson (1936) described it as a zone of four major faults striking N65°W regionally with a series of northeast-trending, 5 km long en échelon normal faults truncated by the major faults. A later regional aeromagnetic study confirmed Wilson’s notion that the zone was related to faulting in the Precambrian basement (Zietz, 1971). Topography along this lineament is much more subtle than surrounding arches and consist of a chain of aligned domes and monoclines.

Timing of Adjacent Laramide Uplifts

The timing of uplifts around the basin have only been studied for the Beartooth and Bighorn Mountains (Omar et al., 1994; Peyton, 2009). No data on Laramide exhumation of the Owl Creek Mountains has been published. Based on apatite fission dating on the Beartooth and Bighorn Mountains the Bighorn Mountains predated the exhumation of the Beartooth Mountains. According to Peyton (2009), the Bighorn Mountains were exhumed prior~75Ma whereas the Beartooth Mountains were uplifted prior to ~58Ma. The ages for the uplift of the Beartooth Mountains are consistent with ages suggested by Omar et al. (1994) and Cerveny (1990). Formation of anticlines on the BHB shoulder are most likely contemporaneous with the surrounding Laramide uplifts.

Anticline Formation

The anticlines within the BHB most likely resulted from the same regional shortening as the surrounding basement arches. Many of the anticlines display variations in size, topography, ages of units exposed and dip angles. Changes of anticline morphology suggest different fault mechanisms at depth and can be broadly divided into a hierarchy of three classes based on the geometry and depth of bounding faults (Figure 8). The first class (Type I, Oregon Basin) is defined by major, deep thrust faults (e.g. Oregon Basin and Line Creek faults) that extend to the brittle-ductile transition of basement rocks based on two-dimensional seismic reflection profiles (Banerjee, 2008).

The second class (Type II, Horse Center anticline) includes backthrusts off the main, first order faults and often produce high relief, fault-propagation fold structures

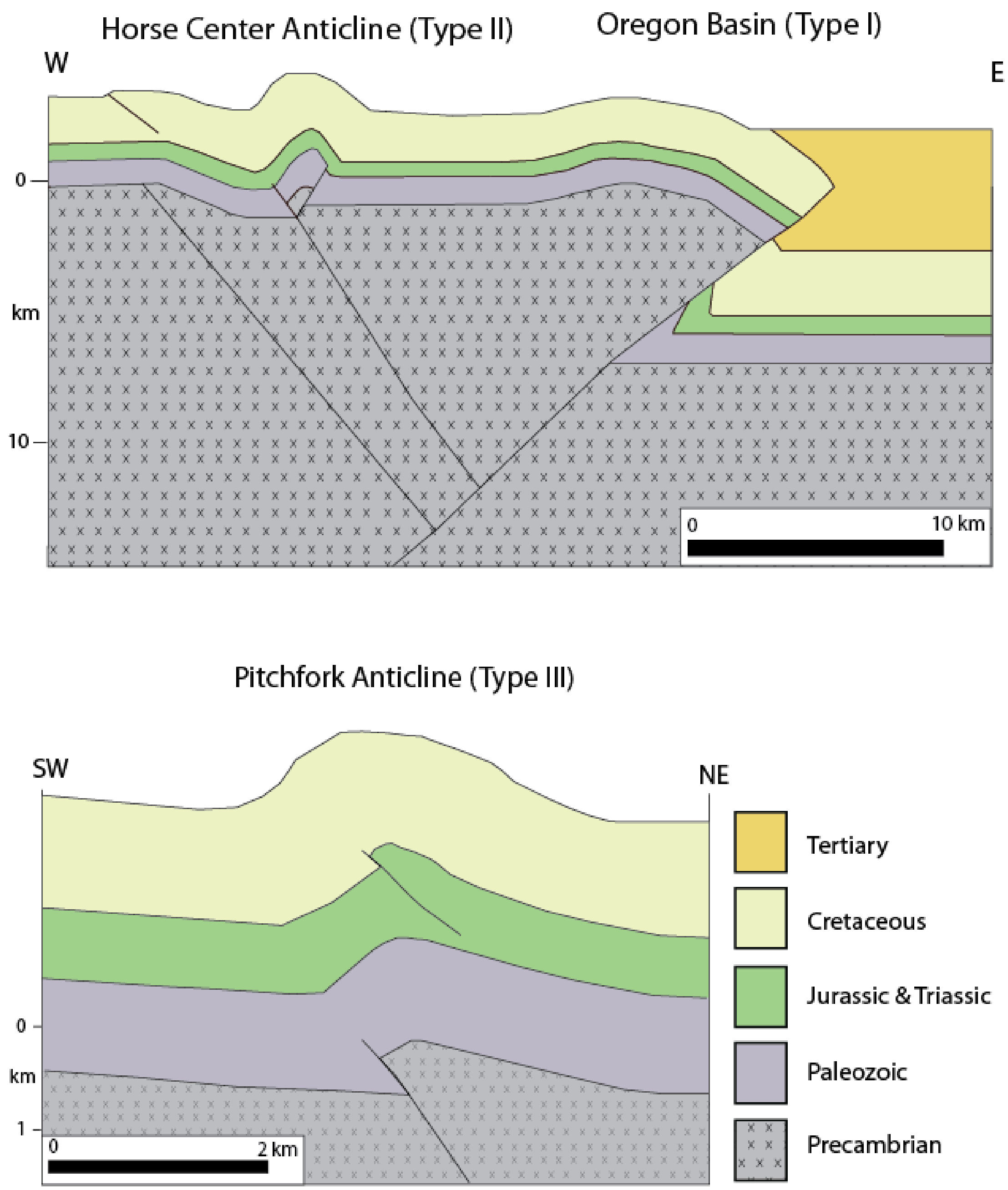

Figure 8: Schematic cross-sections displaying the three types of anticline formation and their respective fault geometries at depth. Cross-sections modified from Banerjee (2008) interpretation of 2D seismic data and well control. Seismic data originally published by Stone (1985), Brittenham and Tadewald (1985), Hennings and Hager (1996), and Mitra and Mount (1998).

(e.g. Rattlesnake Mountain and Grass Creek anticlines). The third class (Type III, Pitchfork anticline) does not involved basement faults, takes advantage of the Phanerazoic stratigraphic largely consisting of interbedded shale and sandstone which provide a competent-incompetent mechanical stratigraphy. For example thrust faults can detach into a shale bed like the Chugwater, Thermopolis, or Cody Formations due to their weak mechanical nature. All anticlines can be classified by Ramsay's fold classification at parallel 1b folds.

Laramide Deformation Styles

Non-Crustal Shortening Models

Since the start of the 20th century, many different deformation mechanisms have been published on the formation of Laramide structures (Hafner, 1951; Prucha et al., 1965; Stearns; 1975; Weinberg, 1979). These models focused on the vertical uplift model, where basement blocks are interpreted to be bounded by near-vertical faults on either side (Figure 9c, 9d), much like a piston to accommodate the basement movement, overlying strata either required normal faulting or ductile thinning (Figure 10) to maintain bed length. Without these two mechanisms, it would be impossible to restore the section and maintain constant volume (Brown, 1993). As research continued across Laramide structures, no significant evidence was found for normal faults or ductile thinning in the sedimentary cover making these models implausible (Brown, 1993).

<u>Crustal Shortening Models</u>

At the time of the vertical uplift theory, other geologists pursued the idea of crustal shortening and thrust faults (Blackstone, 1940, Berg, 1962; Brown; 1993; Erslev, 1991, 1993). Evidence for this model of Laramide deformation exists all over the Rocky Mountain foreland with thrusts and backthrusts bringing basement rocks to high elevations and folding overlying sedimentary units into folds and domes with balanced, structural compatibility (Figure 9a, 9b). Although early models struggled to obtain the right contractive geometry, as subsurface seismic and well data increased, Erslev (1991, 1993) geometrically quantified the concept of the triangular shear zones, or trishear

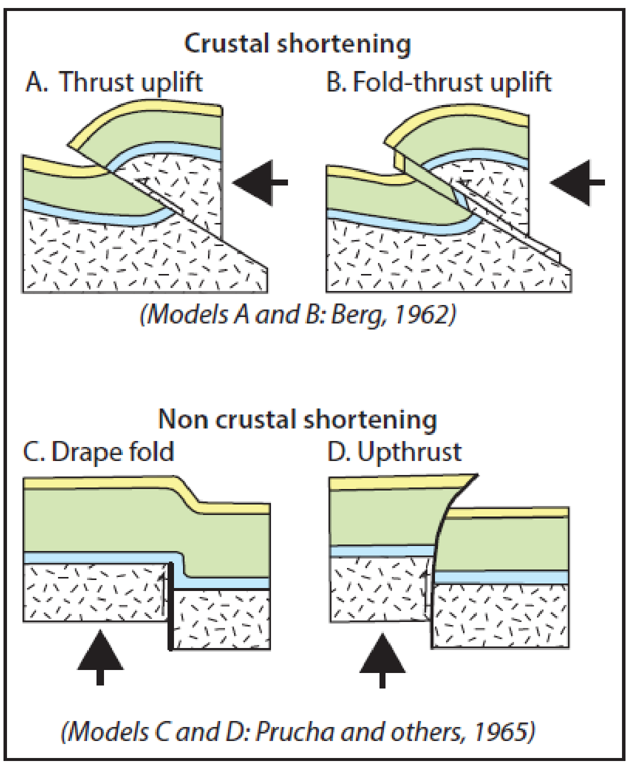

Figure 9: Early shortening and non-shortening models of Laramide deformation styles. Modified from Brown (1993).

zones. The problem of a shortening mechanism that connects fault kinematics to the folded sedimentary strata was solved by this model. As the main thrust reaches the sedimentary cover, movement is split among a series of thrust faults that form a trishear zone. Rather than with a simple shear model, the trishear model's motion vectors are oriented in different orientations. When viewed in cross-section, this mechanism allows the deformed and initial area to remain the same value, solving the problems of the non-crustal shortening models (Figure 11).

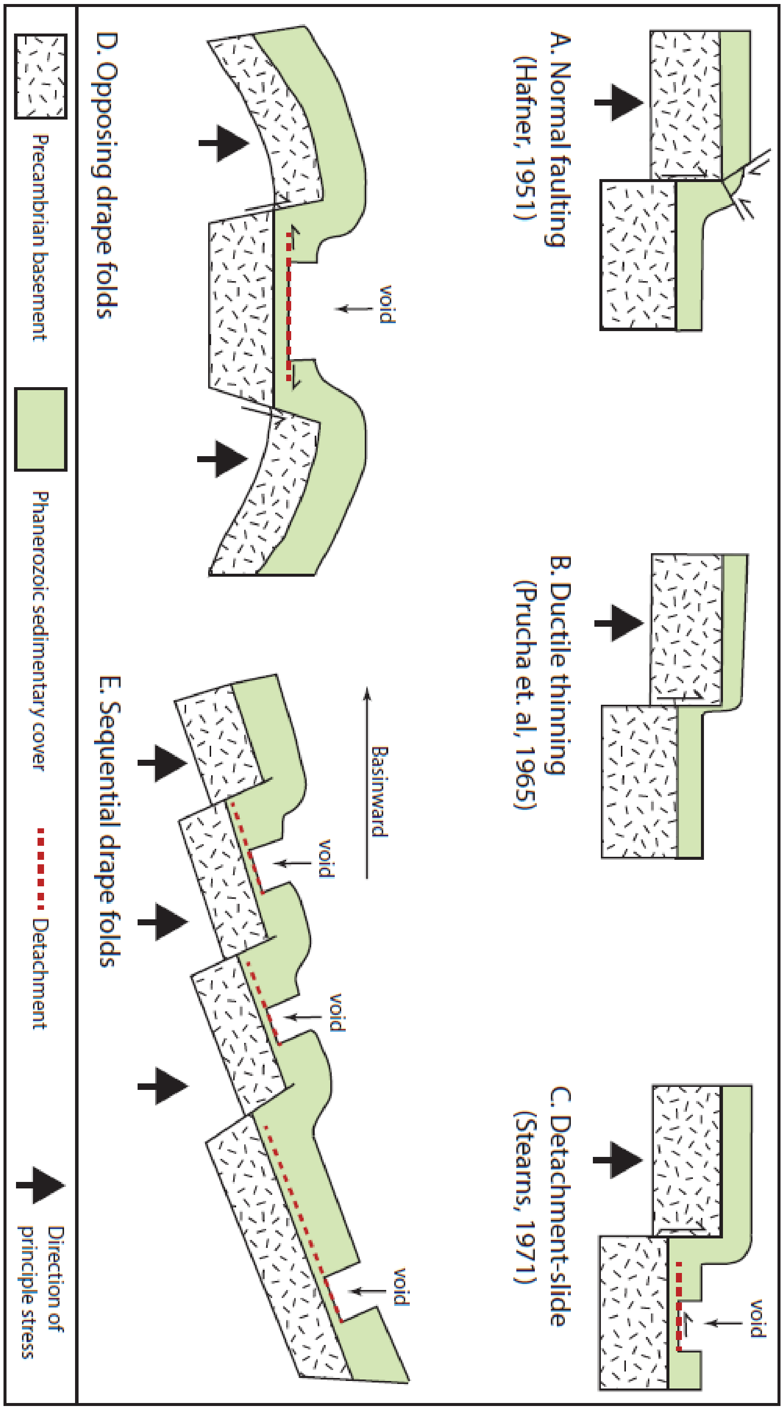

Figure 10: Schematic models showing balancing constraints associated with basement faults and the overlying stratigraphic section. Models A and B are plausible, but no evidence for widespread, deep-seated normal faults or ductile thinning exists within Bighorn Basin folds. Models C, D and E result in regular stratigraphic thickness across the fold, but result in void spaces that are not geologically possible or observed. Diagrams modified from Brown (1993).

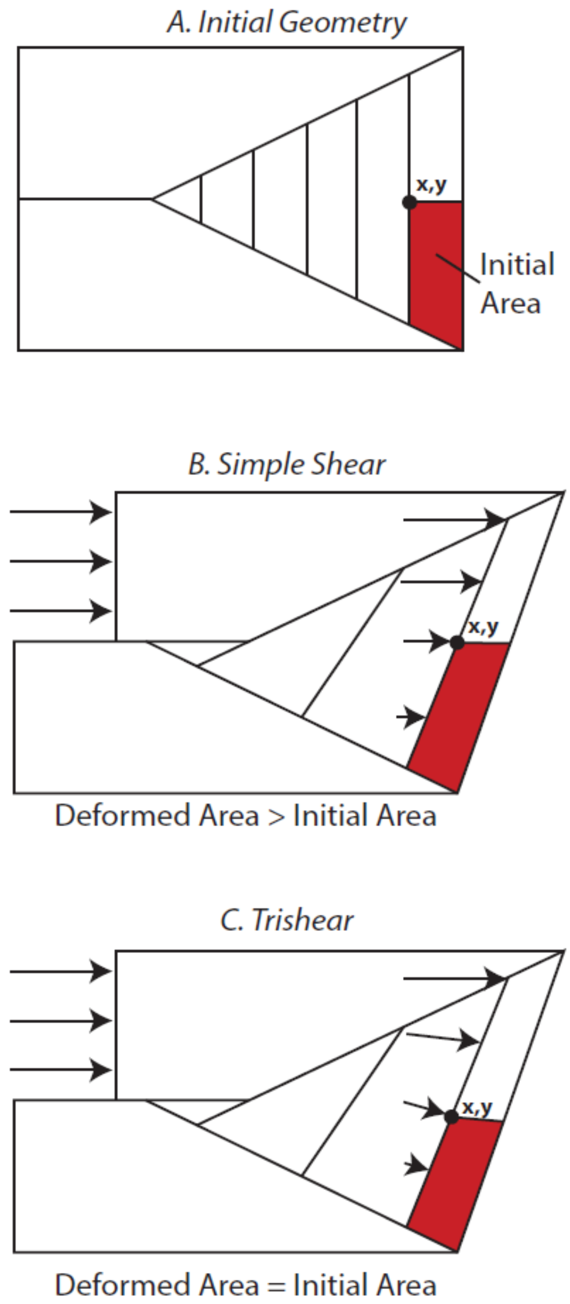

Figure 11: Simple shear and trishear associated with movement across a fault in a triangular shear zone. Simple shear results in a volume imbalance as it expands the base of polygons while contracting the top of the polygons. Trishear maintains constant volume by adding motion oblique to the fault, bringing material from the hanging wall to the footwall side of the shear zone. Figure modified from Erslev (1991).

METHODS

Google Earth Pro

The study of lineaments has been used for the past half century to provide a preliminary structural analysis across the Rocky Mountain foreland (Koenig and Erslev, 2009). With increasingly available, high resolution satellite data and digital elevation models (as incorporated into Google Earth Pro), this method provides a fast, inexpensive initial structural analysis of a field area. For this research selected lineaments are defined as “being linear features at the scale of topographic maps, aerial photos, digital elevation models, satellite images and Google Earth images” (Lageson et al., 2012). These linear features could be large scale faults, dominant fracture sets, abrupt changes in lithology, topographic highs and lows, or vegetation patterns. Lineaments were collected both in map view as well as at an oblique angle to further be able to identify lineaments that may not be visible in map view. Care was taken to exclude any lineaments that may be due to anthropogenic causes (e.g. roads, railroads, water canals).

Data Collection

Google Earth Pro (GEP) was used to identify lineaments due to its easy navigation and combination of satellite imagery overlain on a digital elevation model. Lineaments were extracted from GEP based on a “selection” method as described in van der Pluijm and Marshak (2004). This is a subjective method, whereby lineaments are collected based on systematic repeating features (e.g. orientation) across the structure. Due to the bias of the person conducting the process, the author believes that the resulting data of this approach can only be used for orientation and length analysis and may not accurately represent lineament density. GEP does not provide an option to keep the image at a consistent scale since differences in elevation alter the true ground scale, moreover for the purpose of this research, the scale at which lineaments were extracted ranged between 1:4000 and 1:5000. At this scale it was possible to pick enough lineaments to provide a thorough lineament analysis of each anticline. Lineaments that were present on steep slopes required a larger scale map due to their short map trace.

GIS Processing and Rose Diagrams

After compilation of lineament measurements in GEP, the data was imported in ESRI ArcGIS as a KML file and converted to a polyline feature shapefile. By running GIS geometry tools, the length and orientation of lineaments were calculated and added to the attribute table. To classify the lineaments based on their relationship to the fold axis (strike or dip lineaments), the table was exported to Excel and basic command lines were used to automatically determine each lineament set based on a 20° buffer of either parallel to the hinge line, defined as strike BC lineaments, or perpendicular to the hinge line, defined as dip or AC lineaments (Figure 12) . All other lineaments were classified as oblique to the hinge line. Joining this new data to the original attribute table in ArcGIS allowed for a visual, color coded GIS image overlain on a geologic map (Wyoming State Geological Survey) and hillshade extracted from a 1/3 arc second (10 meter) resolution digital elevation model obtained from the United States Geological Survey National Elevation Dataset (USGS NED). The lineament data for each anticline was then exported into Rich Allmendinger’s Stereonet 9 software for construction of rose diagrams.

Individual pedals were color-coded based on their orientation to the hinge line with a 20° buffer.

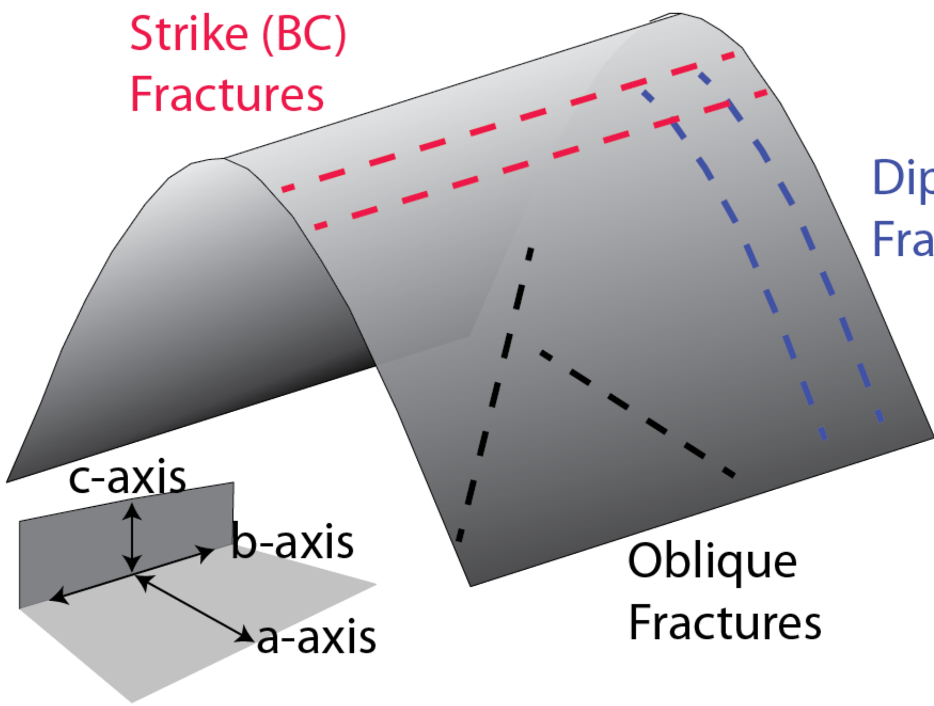

Figure 12: Schematic diagram showing fracture (lineament) orientations as they are classified in this study. The three fracture sets considered are dip (AC), strike (BC), and oblique fractures.

Google Earth Pro Accuracy

GEP is perfectly suitable for preliminary analysis of satellite images, terrain, and a variety of user imported datasets, however, precautions must be taken when using it to extract orientation data. Since the images need to be accessed seamlessly across the entire globe, the developers had to make sacrifices in the type of projection coordinate system they used. Modern projections for smaller scale areas are able to preserve one or two of the map distortions (shape, distance, true direction, area). However, GEP uses a plate carree cylindrical projected coordinate system. This type of projection divides up the spherical surface of the globe by superimposing a Cartesian coordinate system on it that consists of equal size, shape and area grid cells, the standard parallel is the equator. Due to this simple projection style, shape and area distortion increases away from the equator. Direction is only preserved perfectly along the standard parallel; however, distance is accurate along the meridians as well as the parallels.

Understanding this distortion is important for analyzing the orientation of lineaments extracted from GEP. Since the BHB is located approximately between 43°-45° N, the distortion using this coordinate system creates a significant error that can be reduced by reprojection in ArcGIS to a custom Universal Transverse Mercator system with the standard Meridian selected at the center of the mapping area. This method greatly reduces distortion and more accurate orientations can be measured. For this reason, lineament orientations were measured in ArcGIS and not GEP, as described in the methods used by Lageson et al. (2012).

Outcrop Fracture Measurements

The preliminary lineament analysis described above was ground truthed by outcrop fracture orientation analysis in hope of relating the major lineament orientations to dominant fracture sets within each anticline. Six weeks were spent in the field using a GETAC F-110 rugged tablet with a high accuracy GPS incorporated into ArcGIS to collect the spatial data. The lithologic units where most fracture measurements were made were the Jurassic Morrison and Cretaceous Cloverly, Mowry, Thermopolis, Frontier, Cody, Mesaverde and Meeteetse Formations. Although the Mowry, Thermopolis and Cody Formation are technically classified as shale, the units do contain thin (5-50 cm) silty sandstone intervals that display fractures very well. An effort was made to select outcrops equally spaced around the entire anticline to provide the most robust dataset.

Data Collection

At each outcrop a Geo Pocket Transit Brunton compass was used to collect the dip direction and strike of each fracture, as well as bedding orientation. A thin 4 inch x 4 inch piece of wood was used for fractures that did not have a viable plane to measure on, in order to project the plane into space where a Brunton could be used. As with the GEP lineaments, the selection method was used to collect systematic fracture orientations. This method seemed most viable as the large field area required measuring in units of different age, lithology and thickness which made Van der Pluijm and Marshak's (2004) circular inventory impossible because fracture spacing varied greatly between the outcrops. In general, fractures were collected within a 25 meter radius of the GPS location of the outcrop. The number of fractures measured at each station depended on the outcrop quality as well as complexity. Fractures were classified by their mode of opening, although more than 90% of fractures appeared to be mode I tensile fractures (joints) and displayed no evidence of shearing or tearing parallel to the plane of the fracture (Ramsay and Huber, 1987). Only a few fractures had calcite striations from which an orientation and rake was measured. Systematic fracture sets were categorized in the field and abutting relationships recorded when observed to determine relative fracture timing.

Stereonets

The fractures of the individual outcrops were imported into Rick Allmendinger's Stereonet version 9.3.1 software package for construction of both *in situ* and rotated/unfolded stereonet plots. Fractures plotted as poles to the fracture plane were contoured using kamb contouring as described in Cardozo et al. (2013). Based on the contouring, average dominant fracture sets were determined and added as a new plane dataset.

In order unfold the data to their original orientation, the fold axis of each anticline had to be calculated from bedding orientation. Although bedding orientations were collected at each outcrop, the accuracy of the fold axis measurement was increased using past literature and published geologic and oil and gas maps that were mined for additional bedding orientations. Since anticlines within the basin are not perfectly cylindrical and tend to be doubly-plunging, two fold axes were calculated for each half-anticline where possible. Again, the poles to bedding were plotted for each half-anticline and contoured with the kamb method of Cardozo et al. (2013). The Stereonet software incorporates an axial plane finder tool where the two required limbs were specified by the kamb contouring of the bedding planes.

Once the fold axis and axial planes were calculated, *in situ* fracture orientations were unfolded about the fold axis. First the plunge of the fold axis was removed by rotation about a line perpendicular to the fold axis trend, and subsequently bedding dip was removed about the strike-line of the bedding (Marshak and Mitra, 1988).

Statistical Comparison

In order to compare the fracture measurement results within a single anticline, between adjacent anticlines and across the basin, several basic statistical analysis tools were employed. First, fractures were classified, just like the lineaments mentioned above, by their geometric relationship to their respective fold axis (e.g. dip (AC), strike (BC), oblique 1 and oblique 2). At anticlines with two fold axis of different orientations, outcrops were divided based on their spatial proximity to each fold axis for calculation of fracture to fold axis geometry. Based on the fracture classification given, average fracture trend values were calculated along with a standard deviation to understand the spread in the data.

Once all fractures from each individual anticline were averaged, the values were taken to compare the trend of fractures on a basin wide scale. To further aid in this investigation, the angle between the average fracture orientation of each anticline to the fold axis and the angle between dip (AC) and strike (BC) fractures were calculated. Also, the average fracture orientation for each fracture set was calculated across the entire basin. This statistical representation of data allowed for easy comparison of fracture orientations across the basin.

RESULTS

Introduction

Each of the nine anticlines (Elk Basin, Horse Center, Oregon Basin, Little Buffalo Basin, Grass Creek, Thermopolis, Tensleep, Manderson, Garland Basin) within the BHB were examined for fractures in the field (Figure 2). Data including lithology, bedding orientation, fracture orientation and fracture modes were recorded at each anticline. Lithologies ranged from siltstone to coarse grained sandstone. Shale outcrops were avoided due to inherent mechanical weakness and high erosion potential resulting in poor fracture preservation. In general, measured fractures consisted mainly of mode I fractures (joints), although some may have been hybrid fractures with both an opening and shear/sliding movement across the surface but often with no well-preserved movement indicators. Kinematic indicators were often absent with only two outcrops displaying mineral fiber growths on the surface. Age determination of fractures was solely based on cross-cutting and abutting relationships of different fracture sets, and was occasionally impossible to determine at some outcrops. The following lineament and fracture analysis results examine the anticlines in a counterclockwise direction around the BHB starting with the northern-most anticline. Each anticline has a geologic map associated with it. Refer to Appendix A for the legend of the units presented on the geologic map and stratigraphic correlation across Wyoming and Montana. The size of each anticline is based on the youngest tilted formation exposed at the surface at the boundary to the adjacent sub-horizontal Eocene units.

Elk Basin Anticline

Overview

Elk Basin anticline (EBA) is the northern-most within the BHB and is bisected by the Montana and Wyoming state line. It is approximately 14 km long and 5.5 km wide with up to 50 m of topographic relief between the anticline core and adjacent limbs. Since the anticline is mapped based on two different stratigraphic nomenclatures, Wyoming and Montana, correlation of geologic units across the state line is difficult. On the Wyoming side, the anticline exposes Cretaceous Cody Shale at the hinge zone surrounded by resistant Cretaceous Mesaverde Group and Meeteetse Formation forming outward ridges. Tilted Late-Cretaceous Lance Formation defines the outermost extent of the anticline. The Montana segment of the anticline exposes, from oldest to youngest, the Cretaceous Colorado Shale, Eagle Sandstone, Cloverly Formation, Judith River Formation, Bearpaw Shale, Lennep Formation and Hell Creek Formation.

Structurally, the anticline was formed by a west-dipping thrust faults along its eastern margin. Several normal faults oriented NE/NEE, ranging from 0.5 to 5 km in length, segment the anticline, especially at its southern nose. One normal fault follows the trend of the NNW hinge line for 3 km from the southern nose to the center of the anticline. Again, one must note that the faults mapped in Wyoming are not traced into the Montana section of the anticline as they were not mapped on the Montana side.

Fold Classification

Similar to the majority of anticlines within the BHB, EBA is an asymmetric, non-cylindrical, doubly-plunging anticline. Due to the curvature of the hinge line in map view, two different fold axes were calculated from bedding orientations collected in the Mesaverde and Meeteetse Formation on the limbs of the anticline. The north and south hinge line orientations were determined from 94 and 90 bedding orientation measurements, respectively. The southern part of the anticline has an axial surface that strikes at 2° with an 88°W dip and a hinge line that trends at 181° and plunges 10° south. A counterclockwise rotation at the north end of the anticline changes the axial surface to a strike of 155° with an 85°W dip, The northern hinge line plunges 7° towards 334°. The limbs on either side of the anticline closely follow the geometry of the fold axis; however they do display differences in dip along strike. In the northern part of the anticline, the east limb generally has a lower average dip than the west limb.

Lineament Analysis

Across EBA, 569 lineaments were collected from Google Earth Pro imagery. Due to the non-linear geometry of the fold hinge, lineament orientations were divided into the southern and northern half with respect to the fold hinge (Figure 13). For both cases, dip (AC) lineaments dominate the anticline in numbers. Both the north and south halves seem to have a fairly dominant conjugate lineament set oriented NEE and SEE. The features defining the lineaments on the map differ between the strike (BC) and dip (AC) lineaments. Whereas the BC lineaments are usually defined by resistant ridges and eroded valleys, AC lineaments result from drainages most pronounced down the steep limbs of the anticlines. Oblique fractures often acted as small tributaries into the main AC drainages on the limbs. Due to anthropogenic alterations caused by dense construction of

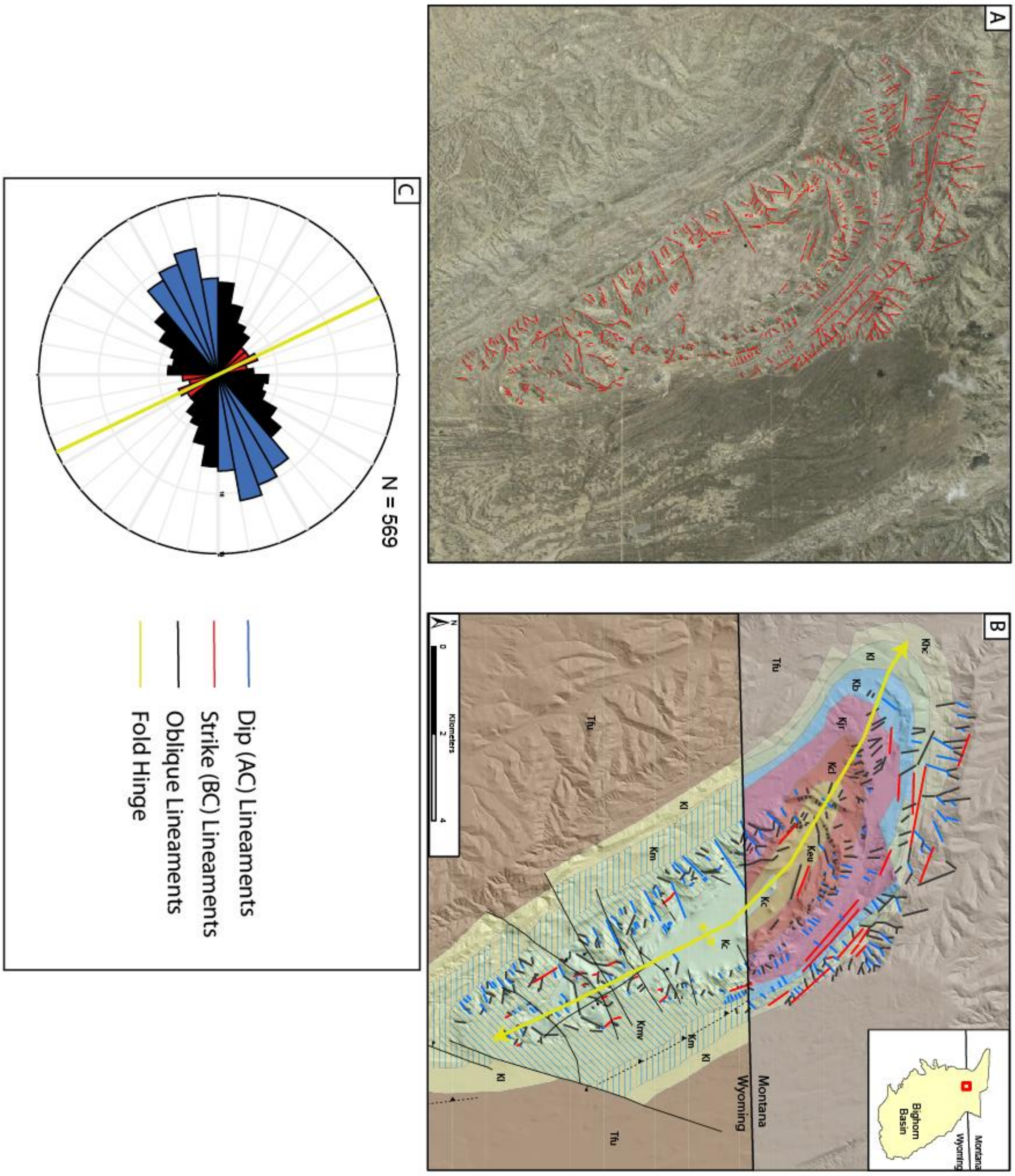

Figure 13: Lineament results of Elk Basin. A) Lineaments compiled from Google Earth Pro satellite imagery. B) Same lineaments classified by their orientation with respect to the fold hinge trend overlain on the Wyoming State Geological Society geologic map and USGS NED hillshade. For geology units symbology and classification refer to Appendix A. C) Rose diagram of lineaments classified by their orientation to the fold axis. Dip (AC) and strike (BC) lineaments represent a 15° buffer to being perpendicular and parallel to the fold hinge orientation, respectively.

roads and infrastructure for oil rigs within the center of the basin, this area was ignored for lineament analysis.

Fracture Analysis

Fracture analysis was performed at nine different outcrops across the extent of EBA. The most southern plunge nose was avoided due to the high density of mapped faults (Figure 14). Outcrops studied included the Mesaverde Group and silt/sandstone beds within the Cody Shale formation or equivalent units in Montana (Eagle Sandstone and Cloverly Formation). In total 153 fractures were recorded (Table 1). For purpose of fracture comparison, all fractures are described here, and in the following sections, with their trend on bedding surfaces rather than their strike.

Rotated Fracture Orientation to Horizontal												
Stereonet #	**AC Strike**	**AC Trend**	**AC Dip**	**BC Strike**	**BC Trend**	**BC Dip**	**O1 Strike**	**O1 Trend**	**O1 Dip**	**O2 Strike**	**O2 Trend**	**O2 Dip**
30							196	16	79	134	134	89
31				179	179	82	51	51	87	121	121	86
32				170	170	85	229	49	79	312	132	75
33	256	76	80	167	167	80	23	23	80	306	126	63
34				308	128	86	209	29	88	155	155	84
35	79	79	86	335	155	88						
36							41	41	77	132	132	82
37				160	160	71	225	45	66	134	134	83
38							46	46	90	295	115	80
Average		**78**	**83**		**160**	**82**		**38**	**81**		**131**	**80**

Table 1: Elk Basin fracture analysis results. Stereonet/outcrop numbers correlate to numbers listed in Figure 13. All fractures are unfolded and rotated back to horizontal bedding orientation.

Since the fractures all display high dip values (80-90°), they can dip into either cardinal direction perpendicular to their trend. Average fracture orientations for each outcrop reveal three systematic fracture sets that relate to the hinge line orientation after

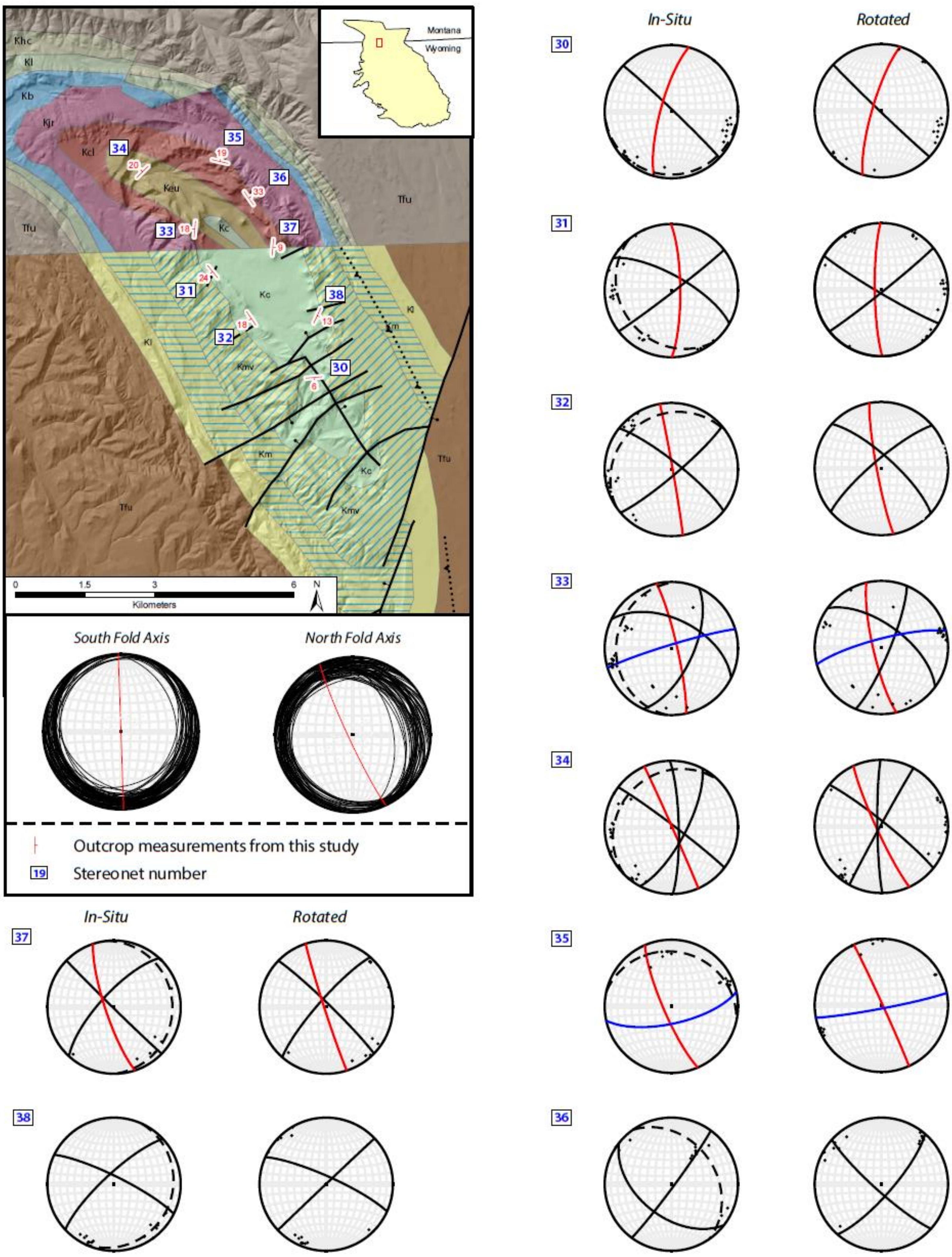

Figure 14: Elk Basin fracture analysis results. Geologic map above displays outcrop locations as well as bedding orientation measurements. Both in-situ and rotated stereonets are presented for each outcrop location. Dots represent the pole to fracture planes. Blue lines represent AC (dip) fractures and red lines represent BC (strike) fractures in relationship to the fold hinge. Black lines are oblique fractures. Dashed lines represent original bedding orientation. Fold axis classification from bedding orientations are divided by the north and south portion of the anticline.

after rotation and unfolding, and to the presumed shortening direction of 040-060°N: 1) dip (AC) fractures (sub-perpendicular to the hinge line, 2) strike (BC) fractures (sub-parallel to the hinge line), and 3) two fracture sets oblique to the fold hinge (oblique 1 and oblique 2). Dip (AC) fractures trend at 76-79° (average 78°) with dips greater than 80° after rotation to horizontal. Strike (BC) fractures trend at 128-179° (average 160°) with a dips greater than 82°. The third fracture set, oblique 1, tends to be oblique to the fold hinge at less than 51° difference in orientation striking to the NNE. When rotated to horizontal the fractures trend 16-51° (average 38°) with an average dip of 81°. The last fracture set, oblique 2, forms an acute angle of approximately 40° striking to the SE. These fractures trend between 115-155° (average 131°) and dip on average at 80°.

Horse Center Anticline

Overview

Horse Center anticline (HCA) is located directly south of Cody, Wyoming extending approximately 9 km along the fold hinge and a width of 4 km across the center of the anticline. On average the anticline has a local vertical topographic relief of 80 m across the structure. Unlike surrounding anticlines, HCA is a smaller, southward extension of the large Rattlesnake Mountain anticline to the north. This is supported by the continuous Jurassic Sundance and Gypsum Spring Formations from the east limb of Rattlesnake Mountain anticline all the way to the western limb and southern nose of HCA, these formations are also partially exposed at the core of HCA. However, the Sundance and Gypsum Spring Formations in Rattlesnake Mountain anticline constitute the younger units exposed, whereas at HCA they are the oldest units at the surface of the anticline. Surface mapped faults are minimal with only one set of faults at the southern plunge-nose. Like other folds within the BHB, HCA is an asymmetric, non-cylindrical fold, plunging only to the south as the northern segment transitions into Rattlesnake Mountain anticline. Important to note is the tightness of the fold. Whereas other folds within the BHB, have limbs with shallow to intermediate dips, HCA's east limb becomes overturned in the northeastern section due to the tight Sage Creek syncline separating HCA from Oregon Basin only 3 km to the east (Banerjee, 2008).

Fold Classification

The hinge line and axial surface of HCA was calculated from nine bedding orientation measurements on the outcrop and 19 orientations adopted from a geologic map by Pierce (1970). The axial surface was determined to strike at 356° with an 78°E dip and the hinge line trends at 165°, plunging 9° to the southeast (Figure 15). The hinge line throughout HCA is linear before rotating approximately 45° counterclockwise at the north end to merge with the Rattlesnake Mountain anticline. Local bedding dips on each limb of the anticline vary between the west and east limb. The west limb dips between 12° and 49° to the west. Bedding orientations around the south nose are surprisingly steep ranging from 37-83°, but may be influence by local fault blocks. The east limb can be divided up into two domains. Directly north of the nose, dips continue to be steep between 41-78°E. However, the northeastern limb dips much more gently (12°-19°E) and is separated from the steep dipping southern half of the limb by a non-printing contact.

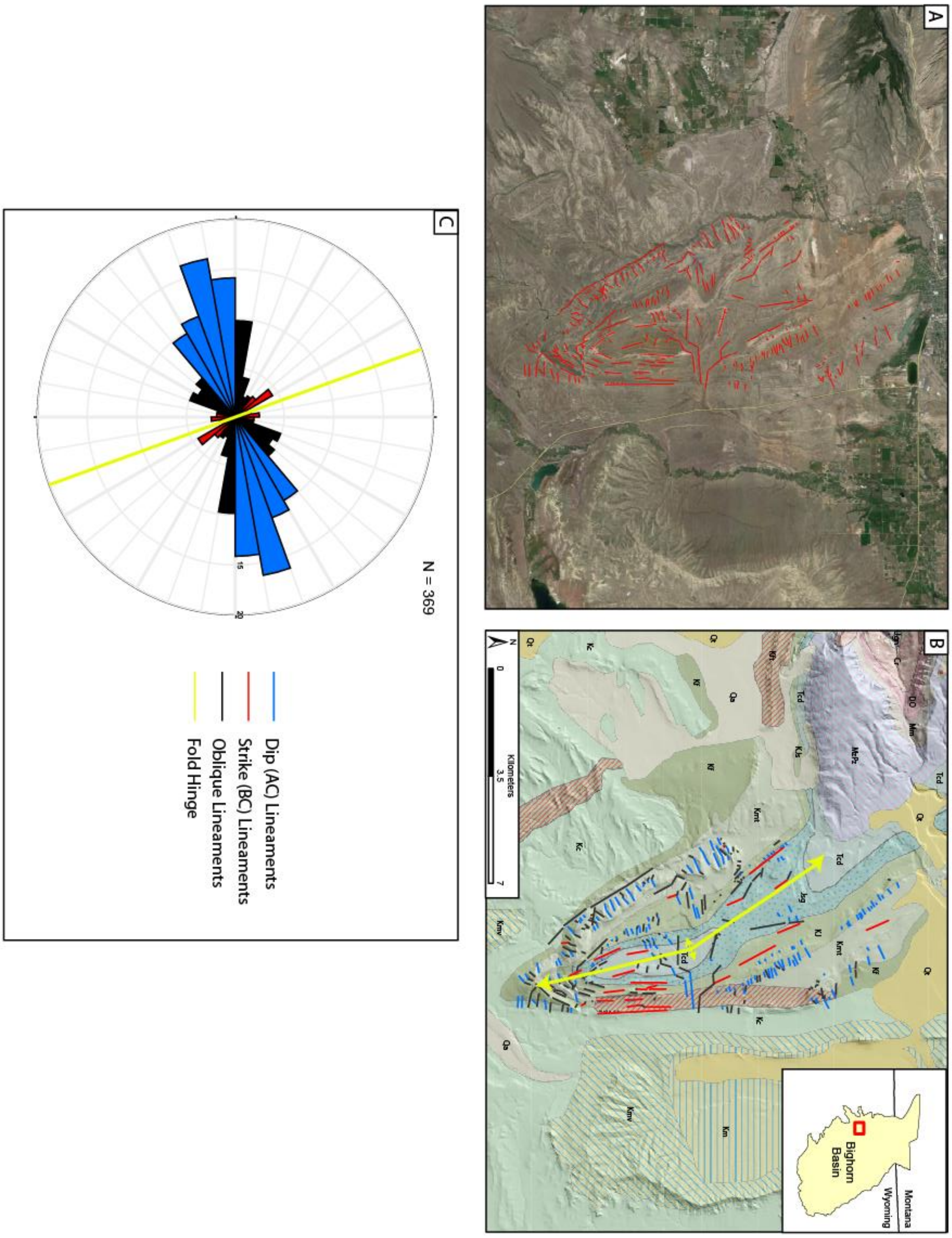

Figure 15: Lineament results of Horse Center Anticline. A) Lineaments compiled from Google Earth Pro satellite imagery. B) Same lineaments classified by their orientation with respect to the fold hinge trend overlain on the Wyoming State Geological Society geologic map and USGS NED hillshade. For geology units symbology and classification refer to Appendix A. C) Rose diagram of lineaments classified by their orientation to the fold axis. Dip (AC) and strike (BC) lineaments represent a 15° buffer to being perpendicular and parallel to the fold hinge orientation, respectively.

Lineament Analysis

369 lineaments were measured on Google Earth Pro (Figure 14). Since the anticline has not been a hydrocarbon producing structure, little surface modification has taken place which allowed for confident identification of lineaments on GEP throughout the anticline. Dip (AC) lineaments outnumber strike (BC) lineaments. Oblique lineaments are not well-defined and are mainly oriented 10° clockwise and counterclockwise from the strike (BC) lineaments. The ridges along the eastern limb generally define the strike (BC) lineaments, whereas drainages off the sides of the dipping limbs define the dip (AC) lineaments.

Fracture Analysis

Across HCA, 145 fractures were measured at 12 different outcrops dispersed evenly across the anticline (Table 2; Figure 16). The following fracture measurements are all rotated back to horizontal about the fold axis and the bedding orientation. Dip (AC)

Rotated Fracture Orientation to Horizontal												
Stereonet #	AC Strike	AC Trend	AC Dip	BC Strike	BC Trend	BC Dip	O1 Strike	O1 Trend	O1 Dip	O2 Strike	O2 Trend	O2 Dip
1	99	99	84									
2	90	90	79				24	24	86	322	142	73
3							42	42	68			
4	85	85	90									
5	91	91	85	0	0	86				141	141	83
6	91	91	79	7	7	78						
7	65	65	84									
8	55	55	90									
9	86	86	73				33	33	87	305	125	84
10							21	21	72	300	120	78
69	98	98	86	187	7	89						
70	100	100	77				18	18	75			
Average		**86**	**83**		**5**	**84**		**28**	**78**		**132**	**80**

Table 2: Horse Center anticline fracture analysis results. Stereonet/outcrop numbers correlate to numbers listed in Figure 15. All fractures are unfolded and rotated back to horizontal bedding orientation.

fractures were the most prevalent with an average trend of 55-100° (average 86°) dipping on average at 83°. Strike (BC) fractures are sub-perpendicular to dip (AC) fractures trending at 5° with an average dip of 84°. Two oblique fracture sets to the fold axis were identified. The first oblique fracture set trends between 18-42° (28° average) with an average dip of 78°. The second oblique fracture set trends between 120-142° (132° average) dipping at 80°, making it sub-perpendicular to the fire oblique fracture set.

Oregon Basin

Overview

Oregon Basin (OB) lies in the west-central part of the basin just southeast of Cody, Wyoming. Unlike other anticlines in the BHB, OB has a lower length to width ratio. It is approximately 25 km long and 14 km wide at its maximum extent. This change in length to width ratio is partially due to the anticline not being fully enclosed by topographic limbs on all sides. Although the eastern side displays a well-defined limb with significant topographic relief, the western limb is not a through-going ridge from north to south, an approximately 4.5 km gap exists between the northern and southern section of the west limb. This gap exposes the Cretaceous Cody Shale that also crops out in the flat core of the anticline. Similar to other BHB anticlines, the limbs of OB are comprised of Cretaceous Mesaverde Group and the Meeteetse Formation. The gap on the western side also creates the odd shape of OB when juxtaposed to other anticlines in this study. Rather than being pseudo-elliptical in map view, Oregon Basin’s southwest limb trends at an angle of approximately 45° to the northwest limb creating a distorted shape.

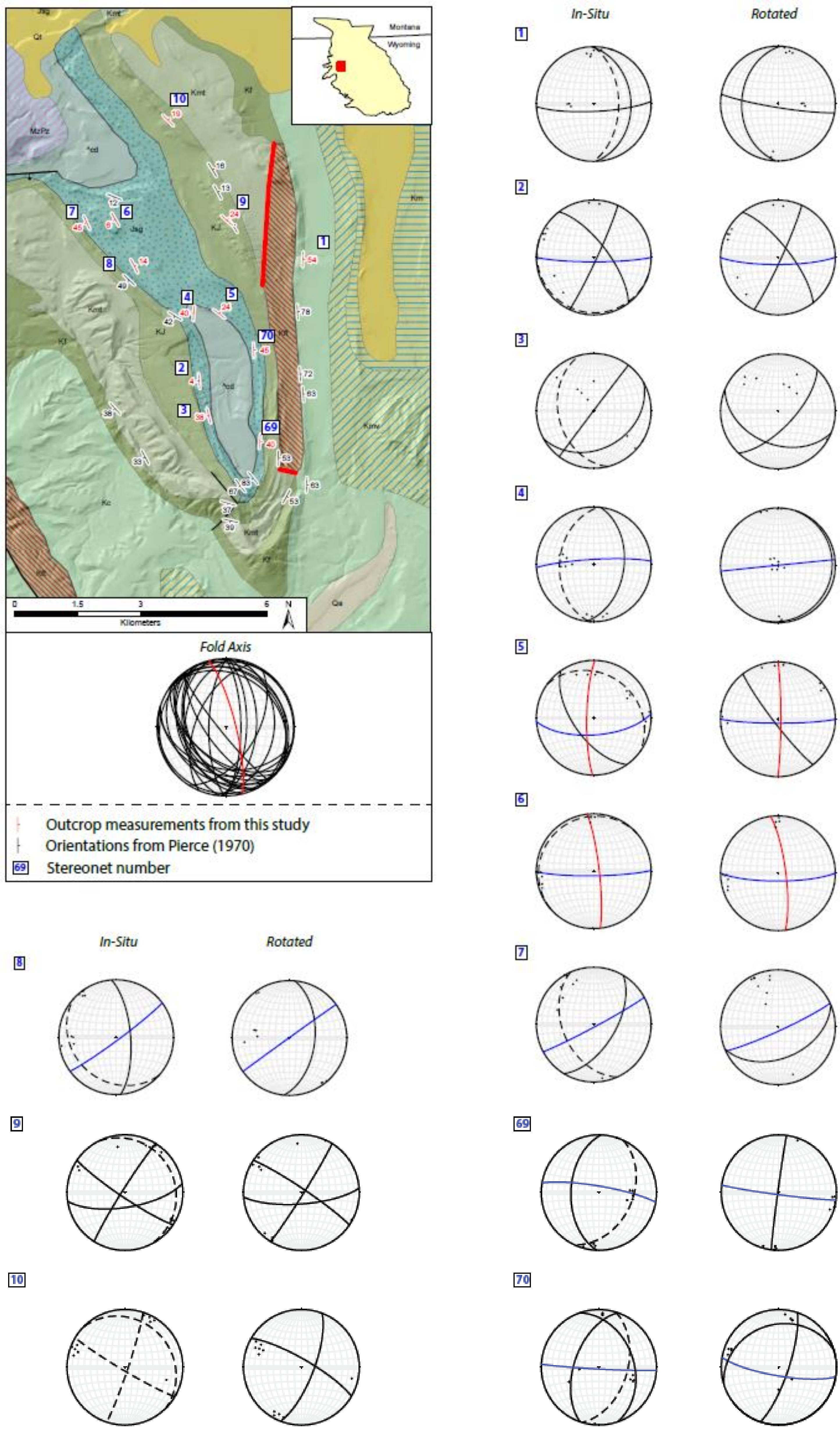

Figure 16: Horse Center anticline fracture analysis results. Geologic map above displays outcrop locations as well as bedding orientation measurements. Both in-situ and rotated stereonets are presented for each outcrop location. Dots represent the pole to fracture planes. Blue lines represent AC (dip) fractures and red lines represent BC (strike) fractures in relationship to the fold hinge. Black lines are oblique fractures. Dashed lines represent original bedding orientation. Fold axis classification calculated from bedding orientations.

In general OB exhibits a higher density of faults when compared to other anticlines. However, the faults tend to be concentrated around the eastern limb and southern nose. All of the faults lie within the Cretaceous Mesaverde Group and Meeteetse Formation and do not extend far into the adjacent Cretaceous Cody Shale and Lance Formation. Most faults trend SW-NE with minor faults trending NW-SE, all of which extend for less than three kilometers.

Fold Classification

As mentioned above, OB has a unique shape when compared to other anticlines in this study which requires calculating both a north and south fold axis. Two hinge lines and axial surfaces were determined using 24 bedding orientation measurements from Hewitt (1926) and nine bedding orientation measurements on outcrops. OB is a non-cylindrical, asymmetric, doubly-plunging anticline with a curved hinge line. The northern axial plane strikes 315° with an 81°SE dip. Its hinge line plunges 6° towards 316°. A minor clockwise rotation to the south, changes the axial plane to a strike of 336° with an 89°SE dip. The southern fold axis plunges 7° towards 156°. Again, the different geometries of the east, southwest and northwest limb are apparent in their relative dips. The northwest limb has dips between 9°W and 21°W whereas the southwest limb dips between 30°W and 42°W. The steepest dips were recorded on the eastern limb at 22°E to 50°E.

Lineament Analysis

Across OB, 897 lineaments were compiled from Google Earth Pro (Figure 17). Unlike other adjacent anticlines (e.g. Horse Center anticline and Little Buffalo Basin), OB's dip (AC) lineaments are not the dominant orientation. Although dip (AC) lineaments are still much more common than strike (BC) lineaments, the most prevalent lineament orientation defines a slightly clockwise rotation from dip (AC) lineaments. Both lineaments within the core of the anticline and drainages off of the northwest limb of the anticline defined this most prevalent last lineament set. However, it is also important to note that the lineament density collected at the northern end is much greater than the rest of the anticline due to the well-defined drainages present. The ridges of the east limb tend to define strike (BC) lineaments. Conversely, the southwest limb displays an oblique set due to its acute angle orientation to the hinge line. Lineaments within the core of the basin were picked with care as anthropogenic alterations are present in certain areas due to oil and gas production infrastructure.

Fracture Analysis

Outcrop fracture analysis in OB was focused on the eastern limb, southern plunge-nose, and southwestern limb (Figure 18). The north plunge-nose and northwest limb were inaccessible due to private landownership and failure to create a contact with the owner about land usage. Across nine outcrops, 80 fracture orientations were measured (Table 3). Four systematic fracture sets were identified after unfolding and rotating the data back to horizontal. Strike (BC) fractures were found within six outcrops with a trend

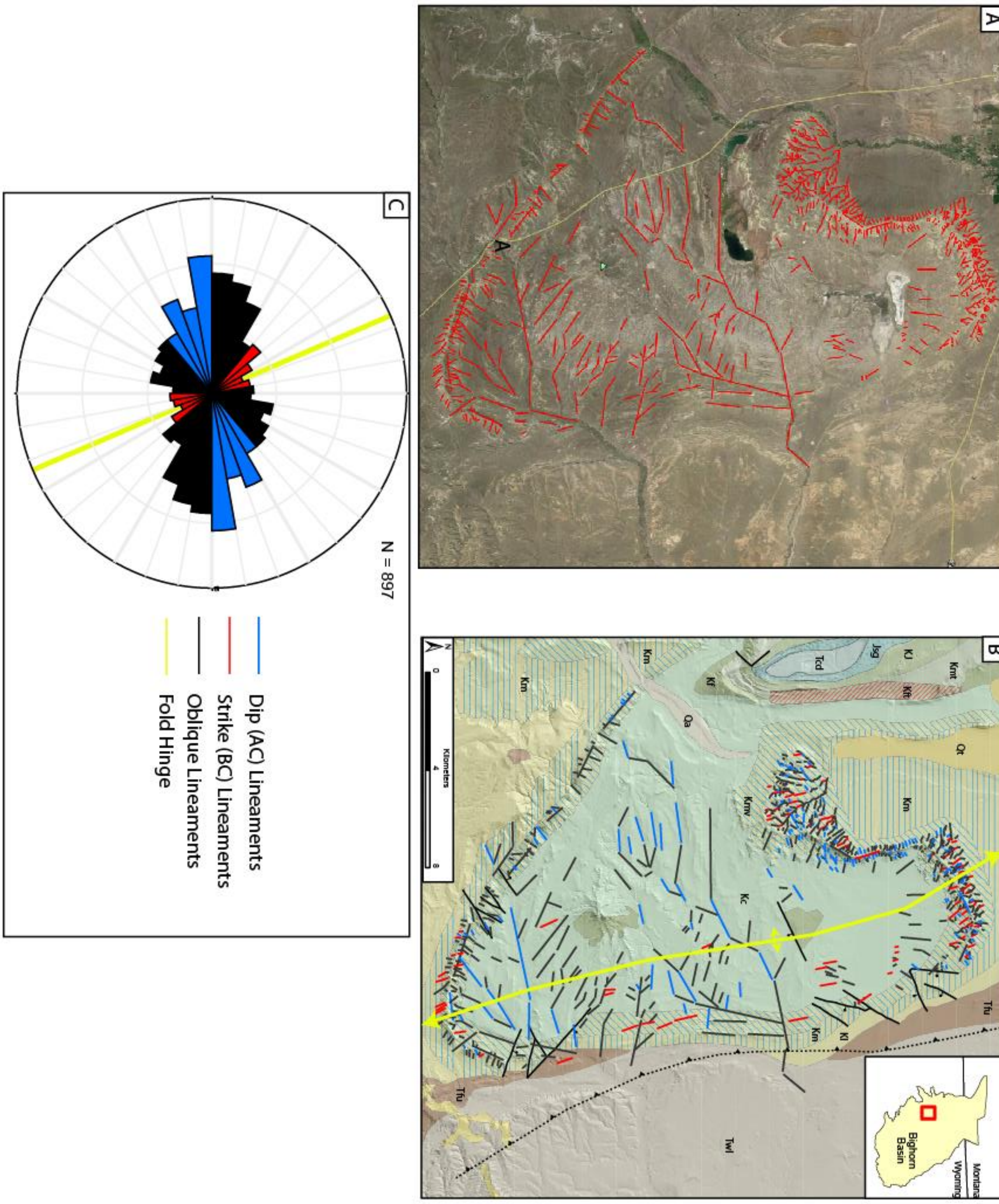

Figure 17: Lineament results of Oregon Basin. A) Lineaments compiled from Google Earth Pro satellite imagery. B) Same lineaments classified by their orientation with respect to the fold hinge trend overlain on the Wyoming State Geological Society geologic map and USGS NED hillshade. For geology units symbology and classification refer to Appendix A. C) Rose diagram of lineaments classified by their orientation to the fold axis. Dip (AC) and strike (BC) lineaments represent a 15° buffer to being perpendicular and parallel to the fold hinge orientation, respectively.

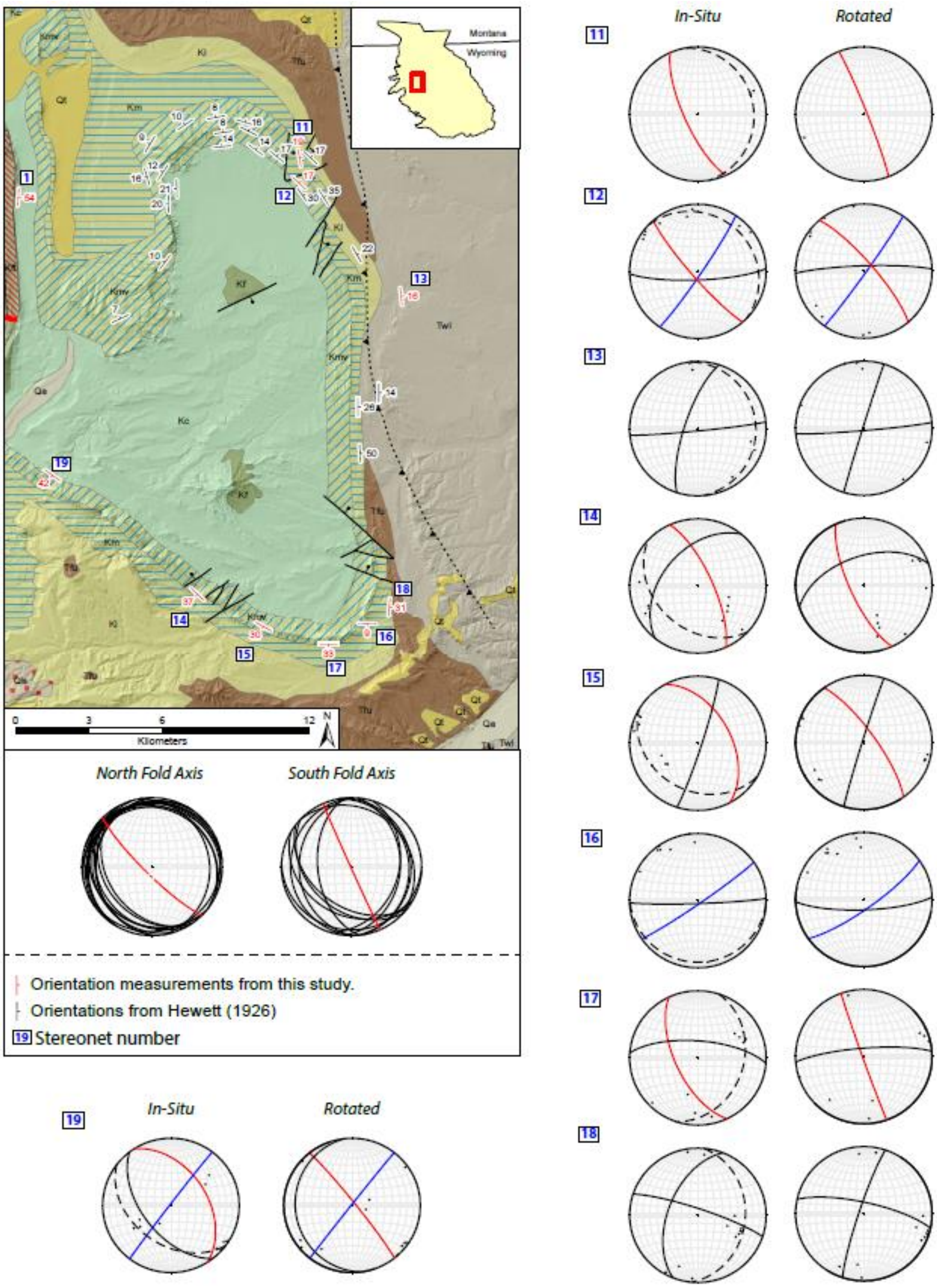

Figure 18: Oregon Basin fracture analysis results. Geologic map above displays outcrop locations as well as bedding orientation measurements. Both in-situ and rotated stereonets are presented for each outcrop location. Dots represent the pole to fracture planes. Blue lines represent AC (dip) fractures and red lines represent BC (strike) fractures in relationship to the fold hinge. Black lines are oblique fractures. Dashed lines represent original bedding orientation. Fold axis classification from bedding orientations are divided by the north and south portion of the anticline.

Rotated Fracture Orientation to Horizontal												
Stereonet #	**AC Strike**	**AC Trend**	**AC Dip**	**BC Strike**	**BC Trend**	**BC Dip**	**O1 Strike**	**O1 Trend**	**O1 Dip**	**O2 Strike**	**O2 Trend**	**O2 Dip**
11				336	156	87						
12	36	36	87	319	139	79				268	88	84
13							198	18	89	85	85	87
14				155	155	73						
15				324	144	76	197	17	88			
16	54	54	79							88	88	77
17				160	160	88				266	86	80
18							199	19	84	282	102	72
19	218	38	89	322	142	86						
Average		**43**	**85**		**149**	**82**		**18**	**87**		**90**	**80**

Table 3: Oregon Basin fracture analysis results. Stereonet/outcrop numbers correlate to numbers listed in Figure 17. All fractures are unfolded and rotated back to horizontal bedding orientation.

trend between 139° and 156° (average 149°) and an average dip of 82°. Dip (AC) fractures occurred in three outcrops with a trend between 36° and 54° (average 43°) and an average dip of 85°. In contrast to other anticlines in this study, the sub-perpendicular oblique fracture sets at an acute angle to the hinge line were not identified in OB. However, a distinct third fracture set exist with two sub-conjugate fractures, classified as oblique 1 and oblique 2. Oblique fracture set 1 trends on average at 18° with a dip of 87°. Oblique fracture set 2 trends on average at 90° with an 80° dip. Both of the oblique fracture sets generally intersect the fold hinge at a high angle.

Little Buffalo Basin

Overview

Little Buffalo Basin (LBB) is located in the west-central part of the BHB, extending 19 km NW-SE and 9.5 km SW-NE with up to 180 m of local topographic relief. It is a non-cylindrical, asymmetrical, doubly-plunging anticline. The Cody Shale is exposed in the anticline core with a majority of the surrounding high relief limbs defined by the Cretaceous Mesaverde Group. On the east limb, sections of Meeteetse and Lance

Formation are exposed. LBB does not have any large scale faults mapped across the surface. A major east dipping thrust fault with an antithetic backthrust define the structure in the subsurface (Banerjee, 2008). Both faults terminate in the Pennsylvanian Amsden Formation deforming the overlying stratigraphy exposed at the surface into anticline seen today.

Fold Classification

The fold axis was calculated from a 37 bedding orientations equally distributed across the limbs within the Cody Shale, Mesaverde Group and Meeteetse Formation. Eight measurements were collected in the field, whereas the remaining 29 are froma map compiled by Hewitt (1926). A hinge line and axial surface was calculated for both the north and south sections of the anticline, but the results were nearly identical; hence only one axis was used for lineament and fracture classification. The north axial plane strikes 336° with an 86°NE dip and the hinge line trends 336° plunging 3° to the north-northwest. Similar to the north, the southern axial plane trends 149° with an 85°SW dip and the hinge line plunges 2° toward 149°. Overall the axis geometry is nearly linear. The west side of the anticline generally has steeper dips (20-39°W) possibly due to the underlying master thrust fault. Different from the west side, the east side dip values are shallow (10-24°E) with the underlying fault being the backthrust off of the master fault.

Lineament Analysis

542 lineaments were measures on Google Earth Pro (Figure 19). Due to the similarity of the north and south fold axis, the lineaments were classified based on an

average between the two axis. Again, dip (AC) lineaments trending at 60-90° outnumber strike (BC) lineaments at 150-180°. LBB also has a pronounced lineament set that consist of two sub-perpendicular lineaments at high angles to the fold axis (trending at 20° and 100°). Different from other anticlines in this study, the core of the anticline is only moderately altered by oil industry infrastructure. Whereas the southern half contains well pads and roads, the northern half remains unaffected, thus permitting lineament extraction from the majority of the anticline. In general strike (BC) lineaments are defined by resistant ridges along the limbs of the anticline and minor drainages on each nose. Drainages on the steep limbs of the anticline flow out of and into the center of the anticline delineating the majority of dip (AC) lineaments. Within the anticline hinge zone, one major east-west drainage dictates the surrounding lineament orientations as all drainages in the core connect with this main one. Lineaments to the north of this drainage trend at a high angle (SE trend) or parallel to the hinge line, whereas the southern lineaments trend NE at a high angle to the hinge line.

Fracture Analysis

Within the LBB eight different outcrops dispersed across the anticline were examined for fracture analysis resulting in a total of 132 fracture orientation measurements (Table 4; Figure 20). Outcrops included sand and siltstone beds within the Cretaceous Cody Shale, Mesaverde Group, and Meeteetse Formation. Out of the eight outcrops studied, four contain dip (AC) fractures, five contain strike (BC) fractures and five contain a perpendicular fracture set where both fractures are at an acute angle to the

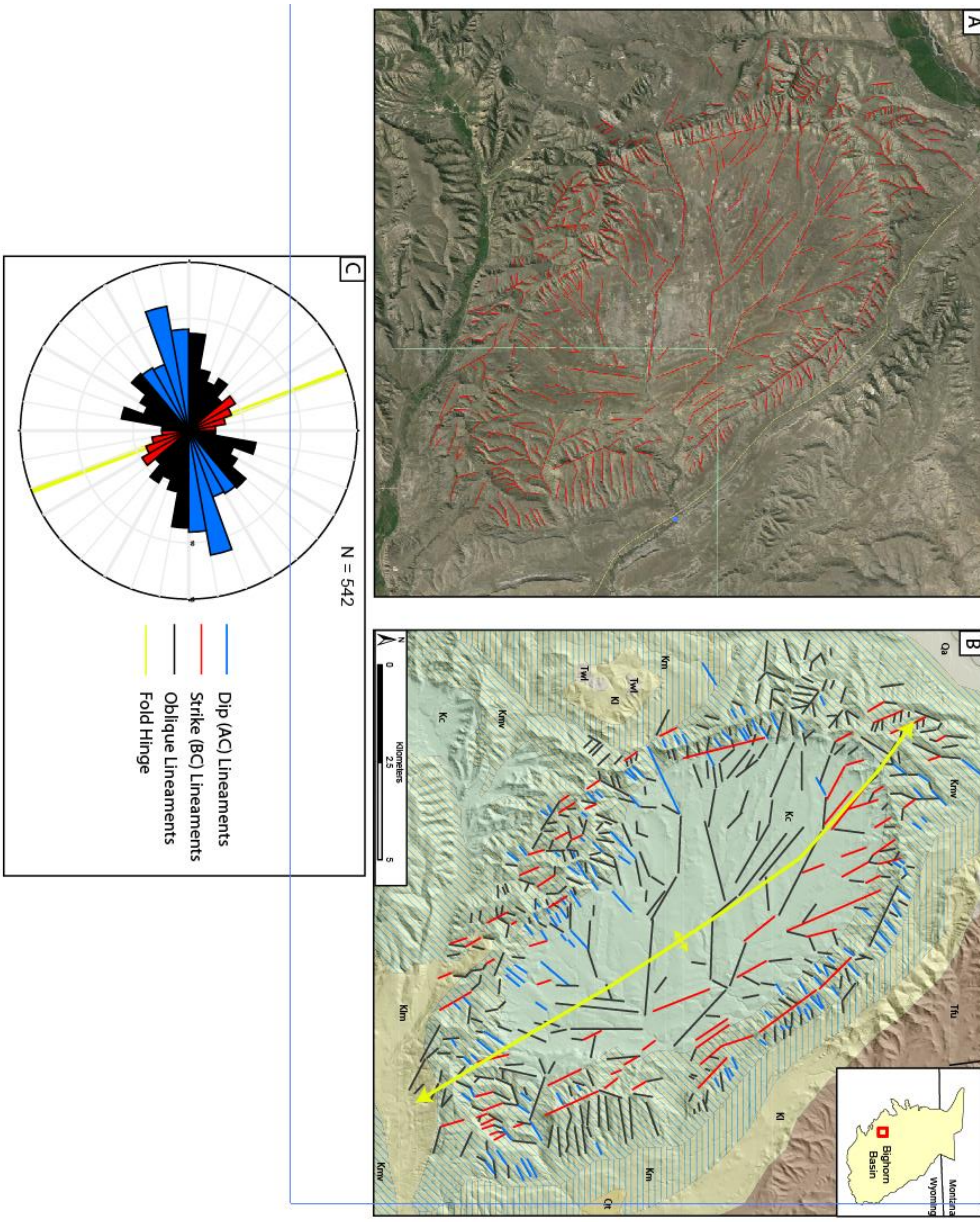

Figure 19: Lineament results of Little Buffalo Basin. A) Lineaments compiled from Google Earth Pro satellite imagery. B) Same lineaments classified by their orientation with respect to the fold hinge trend overlain on the Wyoming State Geological Society geologic map and USGS NED hillshade. For geology units symbology and classification refer to Appendix A. C) Rose diagram of lineaments classified by their orientation to the fold axis. Dip (AC) and strike (BC) lineaments represent a 15° buffer to being perpendicular and parallel to the fold hinge orientation, respectively.

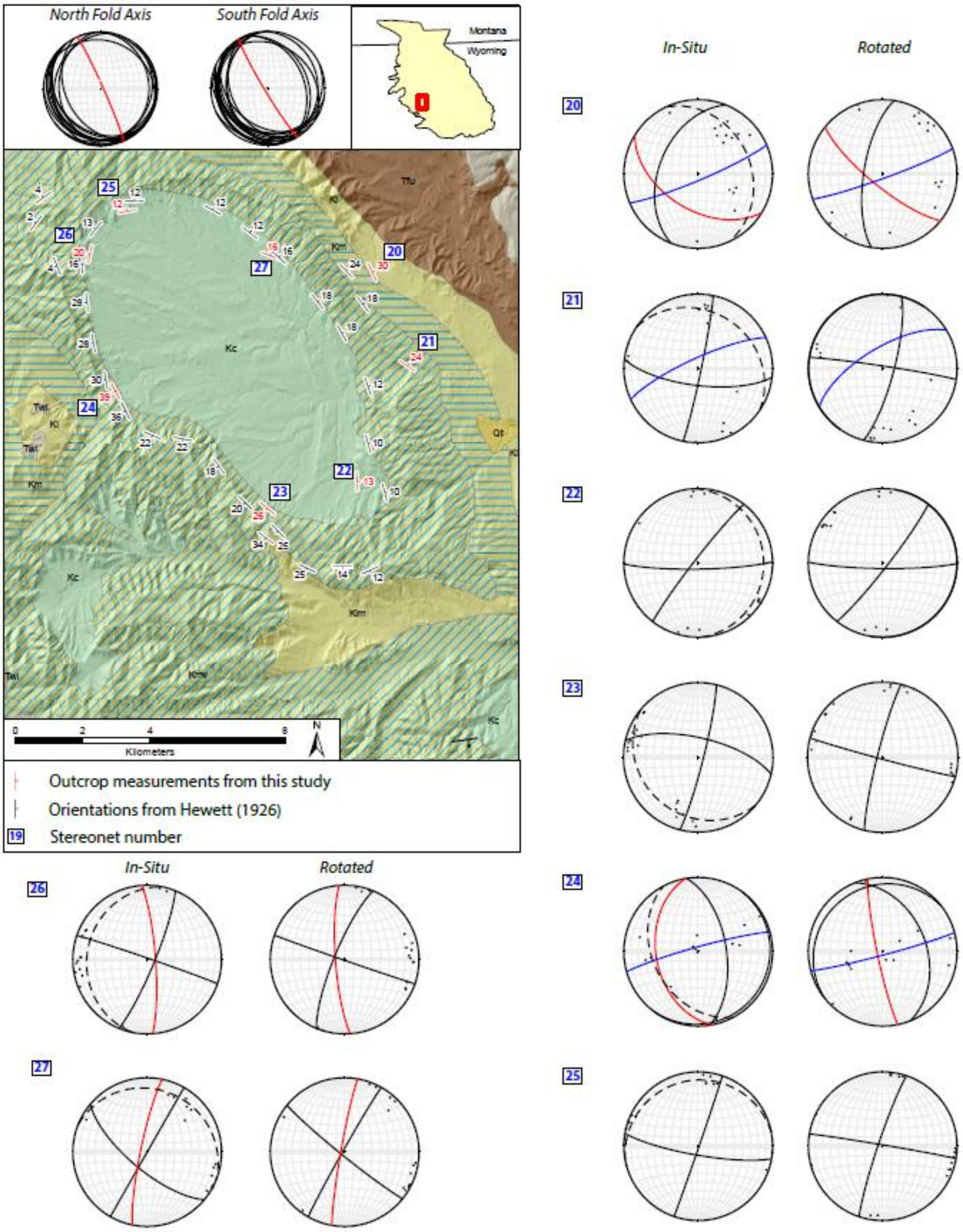

Figure 20: Little Buffalo Basin fracture analysis results. Geologic map above displays outcrop locations as well as bedding orientation measurements. Both in-situ and rotated stereonets are presented for each outcrop location. Dots represent the pole to fracture planes. Blue lines represent AC (dip) fractures and red lines represent BC (strike) fractures in relationship to the fold hinge. Black lines are oblique fractures. Dashed lines represent original bedding orientation. Fold axis classification from bedding orientations are divided by the north and south portion of the anticline.

Rotated Fracture Orientation to Horizontal												
Stereonet #	**AC Strike**	**AC Trend**	**AC Dip**	**BC Strike**	**BC Trend**	**BC Dip**	**O1 Strike**	**O1 Trend**	**O1 Dip**	**O2 Strike**	**O2 Trend**	**O2 Dip**
20	70	70	86	129	129	77	189	9	69			
21	239	59	69				15	15	78	279	99	87
22							38	38	85	91	91	84
23							195	15	84	105	105	88
24	76	76	87	168	168	83						
25							199	19	85	279	99	89
26				176	176	80	203	23	79	109	109	88
27				129	129	86	210	30	88			
Average		**68**	**78**		**158**	**83**		**23**	**83**		**101**	**87**

Table 4: Little Buffalo Basin fracture analysis results. Stereonet/outcrop numbers correlate to numbers listed in Figure 19. All fractures are unfolded and rotated back to horizontal bedding orientation.

hinge line. All three fracture sets display this fracture to hinge line behavior when unfolded and rotated back to horizontal. Dip (AC) fractures trend from a 38° to 76° trend (61° average) with an average dip of 82°. Strike (BC) fractures trend from a 129° to 176° trend (158° average) with an average dip of 80°. The last fracture set that forms a high angle with the fold hinge are perpendicular to each other with an average trend of 18° and 108°, dipping 81° and 88° respectively. Local, non-systematic fractures exist as well.

Grass Creek Anticline

Overview

Grass Creek anticline (GCA) is located just south of Little Buffalo Basin on the southwest margin of the BHB. It has a length and width of 22 km and 9 km, respectively. Like other anticlines, GCA is also a non-cylindrical, asymmetrical, doubly-plunging anticline. The center of the anticline exposes the Cody Shale surrounded by resistant ridges of the Mesaverde Group and Meeteetse Formation with up to 180 m of local topographic relief. Mapped surface faults within the basin are minimal. One small NNW trending normal fault exists at the north nose with minimal offset. The southern nose displays a fault system with a main NW striking normal fault sub-parallel to the hinge line that truncates two smaller NE striking normal faults at a high angle. In the subsurface, GCA has a similar structure as LBB (Banerjee, 2008). A major west-dipping thrust fault terminates several kilometers to the east of GCA in the subsurface (Banerjee, 2008). An antithetic thrust off of this main fault deforms the west limb of the anticline into steep dips (24-58°W). Synthetic to the main thrust and antithetic to the western thrust fault, a smaller west dipping fault deformed the eastern limb of the anticline to a lesser extent (10°-28°E).

Fold Classification

Due to the curvature of the hinge line, two hinge lines were calculated for the north and south section of the anticline. Combining bedding orientations taken in the field with 45 bedding orientations from Hewitt (1926), both fold axis were determined. The southern axial plane strikes at 304° with an 81°NE dip with the fold hinge plunging 5° in the direction of 123°. A clockwise rotation of the axial plane in the north results in a strike of 158° with an 85°E dip. The northern hinge line plunges 9° in the direction of 339°.

Lineament Analysis

Lineaments within GCA exhibit slightly different relationships with the hinge line than other anticlines within in the BHB. A total of 640 lineaments were compiled from GEP with 306 in the northern section and 334 in the southern section of the anticline (Figure 21). The southern section lineaments more closely resemble the orientations of the other anticlines. Dip (AC) lineaments dominate the area in number with a trend of 30° to 60°. However, numerous lineaments have a slight clockwise rotation which may be the result of the clockwise rotation of the hinge line from south to north. When compared to the rose diagram of the northern fold axis, these lineaments clearly fall into the dip (AC) category. Only few strike (BC) lineaments were measured on the anticline.

The northern section of the anticline displays more random lineament orientations. Both the dip (AC) and strike (BC) lineaments have a similar count with the strike (BC) orientation have marginally more. The other oblique lineaments are also systematic. This set consists of two lineament orientations that are perpendicular to each other and lie at a high angle to the fold axis (trending at 20-30° and 110-120°). Dip (AC) lineaments are generally defined by drainages off the side of the anticline limbs, with strike (BC) lineaments following local stratigraphy on the limbs. Within the basin core, several long, hinge parallel drainages also define strike (BC) lineaments. Lineaments along the southwestern limb within the anticline core were not measured due to heavy anthropogenic alteration of farming and hydrocarbon extraction.

Fracture Analysis

Outcrop analysis was limited on this anticline due to land inaccessibility. A combination of private land and active oil rigs operated by Marathon Oil only allowed for two outcrops to be analyzed (Figure 22). 30 fracture orientation measurements were collected over two outcrops (Table 5). Outcrop number 23 has both a dip (AC) and strike (BC) fracture that are sub-perpendicular and sub-parallel to the hinge line, respectively, when bedding is rotated to horizontal. Outcrop number 22 only has a dip (AC)

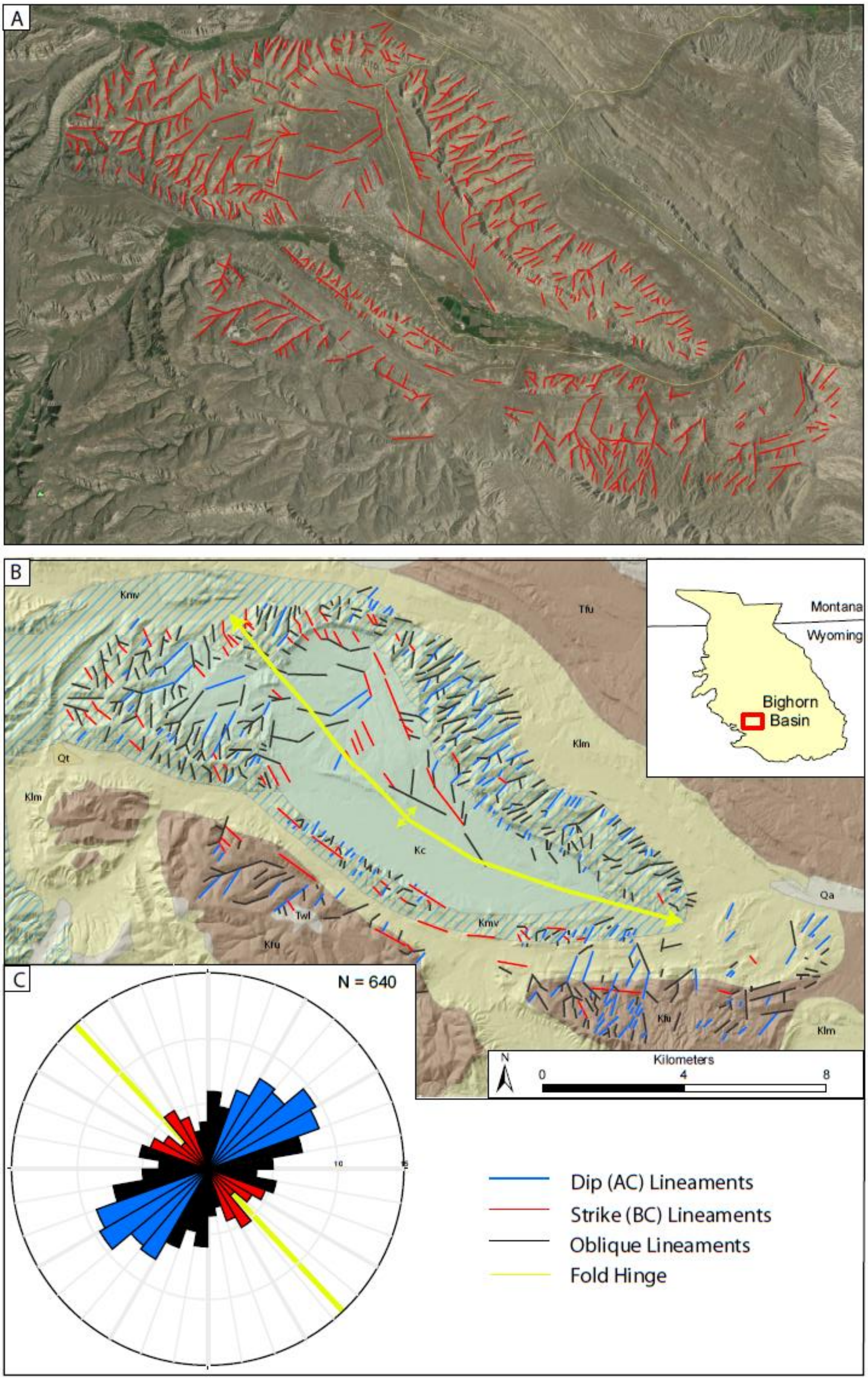

Figure 21: Lineament results of Grass Creek anticline. A) Lineaments compiled from Google Earth Pro satellite imagery. B) Same lineaments classified by their orientation with respect to the fold hinge trend overlain on the Wyoming State Geological Society geologic map and USGS NED hillshade. For geology units symbology and classification refer to Appendix A. C) Rose diagram of lineaments classified by their orientation to the fold axis. Dip (AC) and strike (BC) lineaments represent a 15° buffer to being perpendicular and parallel to the fold hinge orientation, respectively.

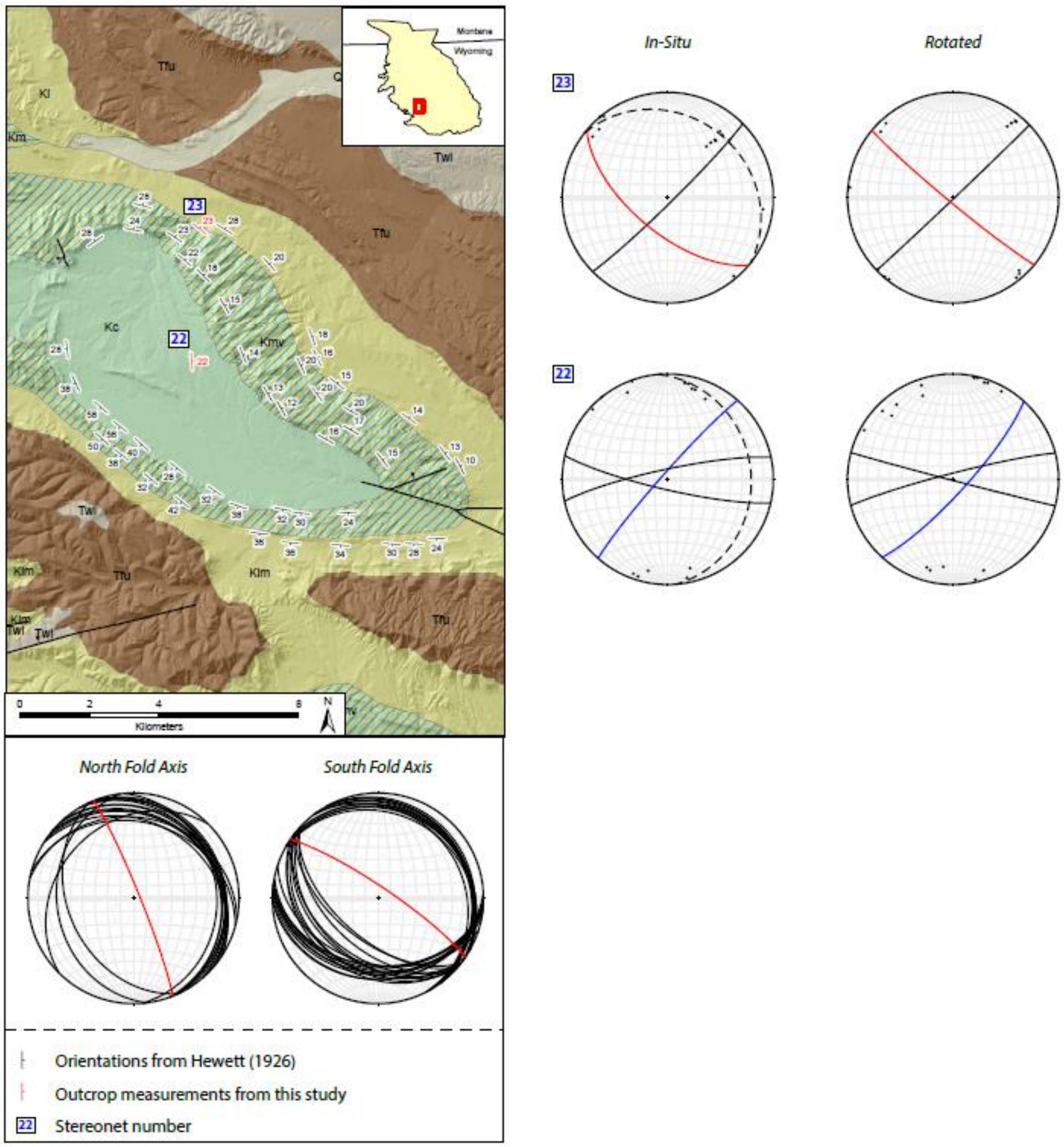

Figure 22: Grass Creek anticline fracture analysis results. Geologic map above displays outcrop locations as well as bedding orientation measurements. Both in-situ and rotated stereonets are presented for each outcrop location. Dots represent the pole to fracture planes. Blue lines represent AC (dip) fractures and red lines represent BC (strike) fractures in relationship to the fold hinge. Black lines are oblique fractures. Dashed lines represent original bedding orientation. Fold axis classification from bedding orientations are divided by the north and south portion of the anticline.

Rotated Fracture Orientation to Horizontal												
Stereonet #	**AC Strike**	**AC Trend**	**AC Dip**	**BC Strike**	**BC Trend**	**BC Dip**	**O1 Strike**	**O1 Trend**	**O1 Dip**	**O2 Strike**	**O2 Trend**	**O2 Dip**
20				130	130	86	47	47	90			
21	255	75	85				42	42	79	104	104	90
Average		**75**	**85**		**130**	**86**		**45**	**79**		**104**	**90**

Table 5: Grass Creek anticline fracture analysis results. Stereonet/outcrop numbers correlate to numbers listed in Figure 21. All fractures are unfolded and rotated back to horizontal bedding orientation.

systematic fracture set with two other oblique fractures at high angles to the hinge line. The small number of outcrops visited at GCA only allows for a very generalized analysis of the fractures. However, LBB is only 4 km north of GCA with similar structures, lithologies, and subsurface fault geometry making it a good candidate as an analogue for this region of the BHB.

Thermopolis Anticline

Overview

Thermopolis anticline (TPA) is the southern-most anticline within the BHB. Overall, it is the largest anticline studied for this project with a fold hinge length of 30 km and a maximum width of 6 km. Due to land accessibility only the northern section to the northwest of Thermopolis, Wyoming, was examined in this study. Different from the other anticlines considered in this study within the BHB, TPA exposes much older rocks within its core. The core of TPA consists of Permian Phosphoria and Triassic Chugwater and Dinwoody Formation. Only Rattlesnake, Sheep, and Little Sheep Mountain anticlines expose rocks of this age. Generally the ridges around the anticline are formed by sandstone beds within the Cloverly, Morrison and Sundance Formations as well as sandstone beds of the Cretaceous Frontier Formation. TPA does not have any surface mapped faults across the structure other than the hinge parallel east dipping thrust fault on its western limb. The western limb of the anticline lies on private land that was not accessible and was not included in the outcrop fracture analysis.

Fold Classification

The folds axial surface was determined from eight field-based bedding measurements and two additional bedding orientations calculated from satellite imagery and USGS NED DEM using a three point method to fill-in data on the west limb. Only the northern axial surface was calculated with a result of a 294° strike and 83°SW dip and the hinge line with plunging 8° in the direction of 330°. Overall, the hinge line is only slightly sinuous. TPA can be classified as a non-cylindrical, asymmetric, doubly-plunging, west verging anticline. Unlike smaller anticlines in the BHB, TPA displays a much steeper with dips of 47° and 65°, the eastern limb's dip ranges from 7° to 21°.

Lineament Analysis

Lineaments within TPA show similar relationships to the fold hinge as the other anticlines studied within the basin. Most of the studied section of TPA provided a natural and unaltered surface for lineament analysis. Only one southwest to northeast swath was avoided due to heavy farming. Of the 406 lineaments, the most common lineament orientation is in the dip (AC) azimuth ranging from 10° to 50° (Figure 23). Strike (BC) lineaments are less dominant at an azimuth of 100° to 140° azimuth. Similar to Little Buffalo Basin, TPA has one distinct lineament set that is oriented 30° to 40 ° to the hinge line with a similar lineament count number as the largest of the dip (AC) rose pedals.

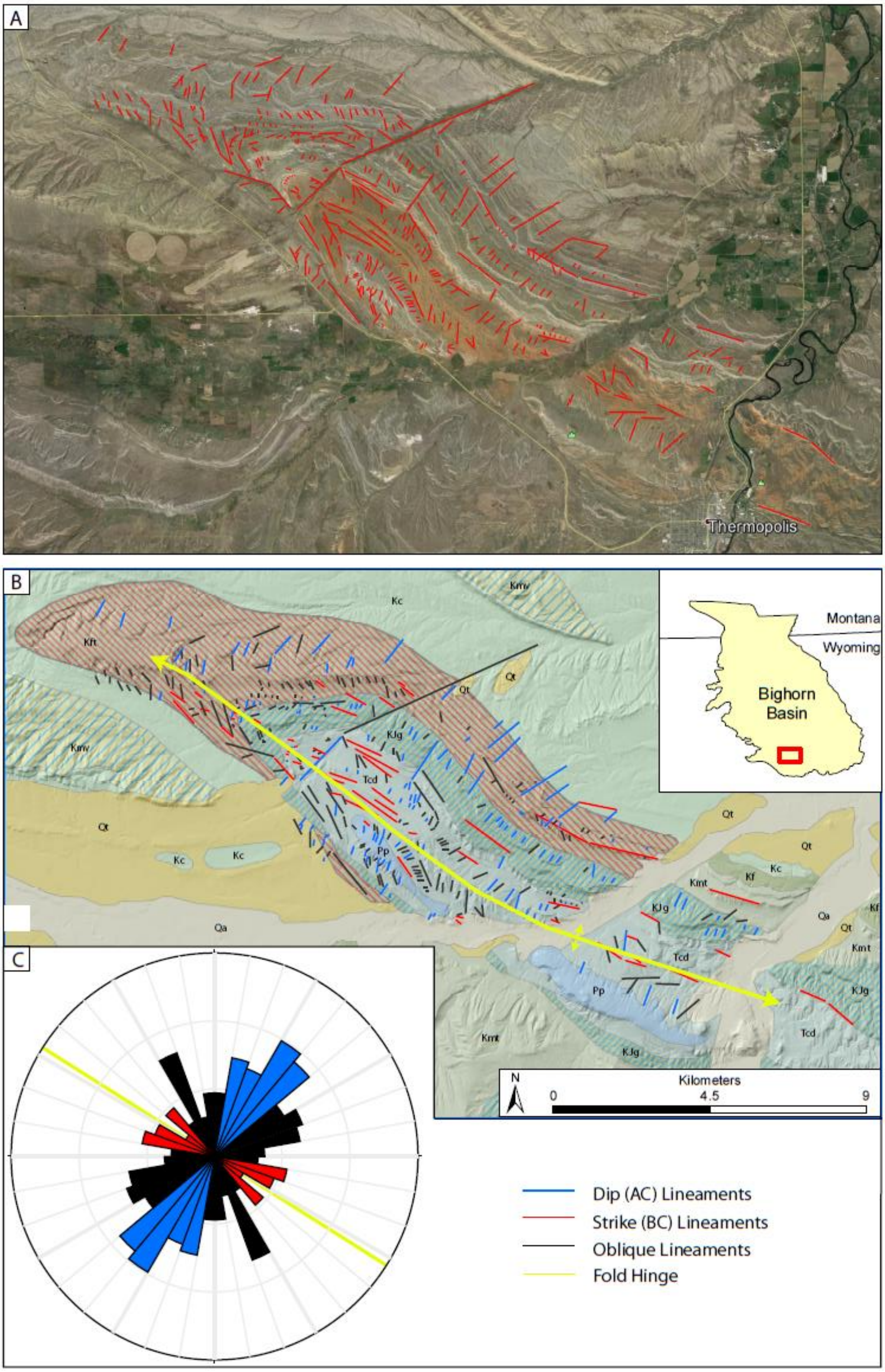

Figure 23: Lineament results of Thermopolis anticline. A) Lineaments compiled from Google Earth Pro satellite imagery. B) Same lineaments classified by their orientation with respect to the fold hinge trend overlain on the Wyoming State Geological Society geologic map and USGS NED hillshade. For geology units symbology and classification refer to Appendix A. C) Rose diagram of lineaments classified by their orientation to the fold axis. Dip (AC) and strike (BC) lineaments represent a 15° buffer to being perpendicular and parallel to the fold hinge orientation, respectively.

Lineaments of this orientation generally occur along the north plunge-nose and northern-most section of the eastern limb. The dip (AC) lineaments again are defined by drainages carved into the dipping strata whereas the strike (BC) lineaments follow ridge lines and adjacent valleys.

Fracture Analysis

Within TPA, 93 fractures were measured across 8 outcrops mainly located on the northern plunge-nose and eastern limb (Table 6; Figure 24). Although both dip (AC)

	Rotated Fracture Orientation to Horizontal											
Stereonet #	**AC Strike**	**AC Trend**	**AC Dip**	**BC Strike**	**BC Trend**	**BC Dip**	**O1 Strike**	**O1 Trend**	**O1 Dip**	**O2 Strike**	**O2 Trend**	**O2 Dip**
61				91	91	72	161	161	78	81	81	90
62							328	148	78	246	66	86
63							339	159	79	73	73	79
64	48	48	61				151	151	73			
65	51	51	68	110	110	71						
66	193	13	86	285	105	86						
67							170	170	79	77	77	77
68										244	64	86
Average		**37**	**72**		**102**	**76**		**158**	**77**		**74**	**83**

Table 6: Thermopolis anticline fracture analysis results. Stereonet/outcrop numbers correlate to numbers listed in Figure 23. All fractures are unfolded and rotated back to horizontal bedding orientation.

and strike (BC) fractures are present across three outcrops, the the most common fracture set were two sub-perpendicular fractures oriented at a high-angle to the fold hinge after rotation to horizontal. The dip (AC) fractures trend between 13-51° (average 37°) with an average dip of 72°; strike (BC) fracture trend between 91-110° (102° average) with an average 76° dip. Fractures at a high angle to the hinge line have an average azimuth of 75° (oblique 1) and 158° (oblique 2), making them nearly orthogonal. Oblique fracture set 1 has a marginally shallower dip of 77° when compared to the 83° dip of oblique fracture set 2. Lastly, a third oblique fracture occurs in two

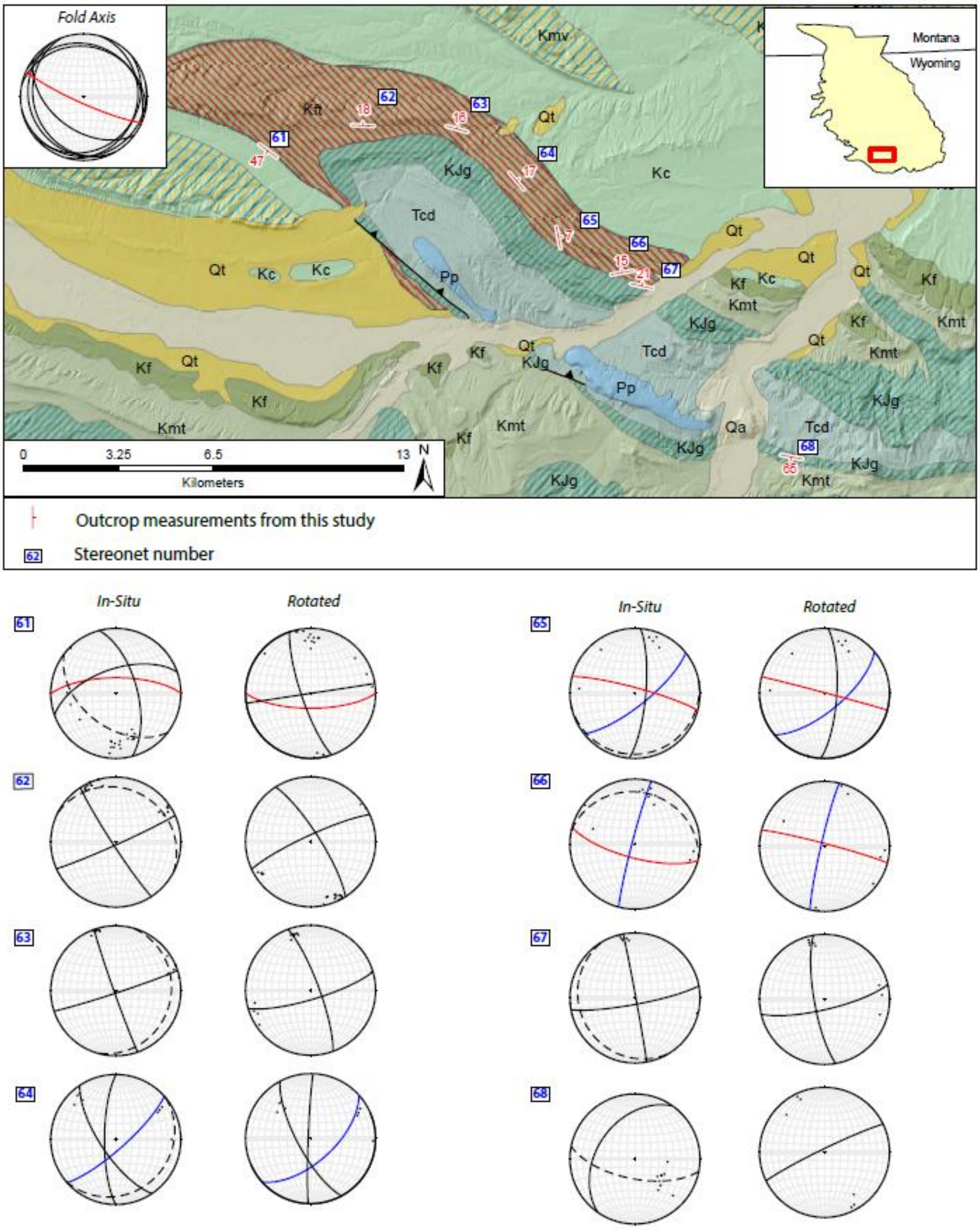

Figure 24: Thermopolis anticline fracture analysis results. Geologic map above displays outcrop locations as well as bedding orientation measurements. Both in-situ and rotated stereonets are presented for each outcrop location. Dots represent the pole to fracture planes. Blue lines represent AC (dip) fractures and red lines represent BC (strike) fractures in relationship to the fold hinge. Black lines are oblique fractures. Dashed lines represent original bedding orientation. Fold axis classification is calculated from bedding orientations.

spatially adjacent outcrops with an azimuth of 3° and an average dip of 81°.

Tensleep Anticline

Overview

Tensleep anticline (TA) is located in the southeastern corner or the basin just south of the locally east-west trending Tensleep fault at the southern end of the Bighorn Mountains. Out of the anticlines studied, TA is the smallest with a length of 5 km and a width of 2 km. It does not resemble the other anticlines in the basin with its surface morphology. The core of the anticline is just as rugged with local vertical relief as high as the limbs on either side. Only the northern plunge-nose was considered, as the southern nose is not well exposed. To the south of the area studied, the west limb is well defined; however, the east limb seems to be truncated by a fault and the southern plunge-nose cannot be identified. The section studied appears to have two anticline noses as seen by the surface morphology on the DEM hillshade, possibly indicating a box fold. Although small in area in comparison to other anticlines, it exposes older rocks than anticlines on the west side of the basin (e.g. Oregon Basin, Grass Creek anticline, Little Buffalo Basin). The core of the anticline contains a small sliver of Jurassic Sundance and Gypsum Spring Formation. Only three faults are mapped across the surface: two northwest trending faults following stratigraphic contacts between the (1) Mowry/Thermopolis Shale and Frontier formation and (2) Cloverly/Morrison Formation and Mowry/Thermopolis Shale are the only faults present. A minor north-south trending fault also exists near the core of the anticline.

Fold Classification

The northern axial surface was calculated from five bedding orientations measured in the field. Additional bedding orientation data was not found in published literature and surface outcrops were not sufficient to calculate bedding orientation from satellite imagery and digital elevation models. The resulting axial surface strikes at 342° with a 79°E dip. Although the northern hinge line was calculated, the hinge line plunges 4° in the direction of 162° which may indicate that this fold is not doubly-plunging like the other anticlines studied. However, TA is an asymmetric, non-cylindrical fold similar to the other anticlines. The hinge line follows a slightly curved path. The basin directed limb, or west limb, dips steeper (30°-59°W) when compared to the east limb (7°-13°E).

Lineament Analysis

Due to the small regional extent of the anticline, only 166 lineaments were collected from Google Earth Pro (Figure 25). Distinction between dip (AC) and strike (BC) lineaments was based on the hinge line as traced out on the geologic map rather than the calculated fold axis from bedding measurements. Dip (AC) lineaments dominate the anticline in numbers and trend between 30°-70°. Strike (BC) lineaments trend between 110°-150° and comparatively have a smaller dip (AC) to strike (BC) lineament ratio when compared to other anticlines. Again strike (BC) lineaments are completely defined by mechanically strong and weak stratigraphy creating ridges and valleys. Most of dip (AC) lineaments follow drainages into the center of the anticline.

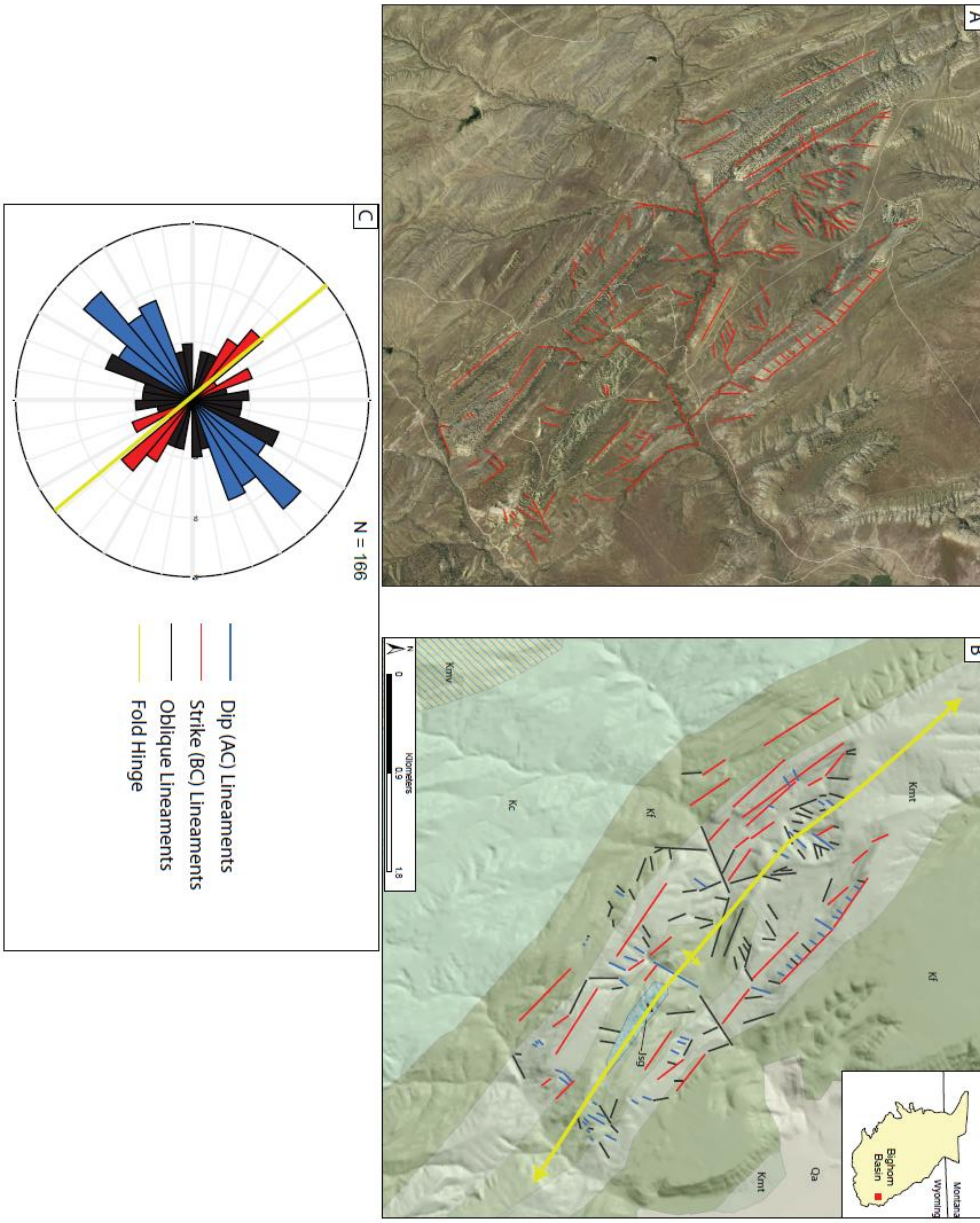

Figure 25: Lineament results of Tensleep anticline. A) Lineaments compiled from Google Earth Pro satellite imagery. B) Same lineaments classified by their orientation with respect to the fold hinge trend overlain on the Wyoming State Geological Society geologic map and USGS NED hillshade. For geology units symbology and classification refer to Appendix A. C) Rose diagram of lineaments classified by their orientation to the fold axis. Dip (AC) and strike (BC) lineaments represent a 15° buffer to being perpendicular and parallel to the fold hinge orientation, respectively.

Fracture Analysis

Across the five outcrops studied for fracture analysis, 76 fractures were measured that fall into three unique systematic fracture sets: (1) dip (AC) fractures, (2) strike (BC) fractures, and (3) two sub-perpendicular fracture sets oblique to the fold axis (Table 7, Figure 26). Dip (AC) fractures are present in three outcrops trending between 76° and

Rotated Fracture Orientation to Horizontal												
Stereonet #	**AC Strike**	**AC Trend**	**AC Dip**	**BC Strike**	**BC Trend**	**BC Dip**	**O1 Strike**	**O1 Trend**	**O1 Dip**	**O2 Strike**	**O2 Trend**	**O2 Dip**
56							38	38	90	308	128	85
57							39	39	78	302	122	87
58	76	76	83				34	34	89	134	134	71
59	279	99	78	152	152	83	30	30	86			
60	273	93	84	173	173	72	213	33	77			
Average		**89**	**82**		**163**	**78**		**35**	**84**		**128**	**81**

Table 7: Tensleep anticline fracture analysis results. Stereonet/outcrop numbers correlate to numbers listed in Figure 25. All fractures are unfolded and rotated back to horizontal bedding orientation.

99° (average 89°) with an 82° dip. Strike (BC) fractures are only found in two outcrops trending between 152° and 173° (average 163°) with a 78° dip. The most common and consistent fractures were the two different oblique sets. The first oblique set trends between 30° and 39° (35° average) with an 84° dip. Almost perfectly perpendicular to this set, the second oblique set trends between 122° and 134° (average 128°) with an 81° dip.

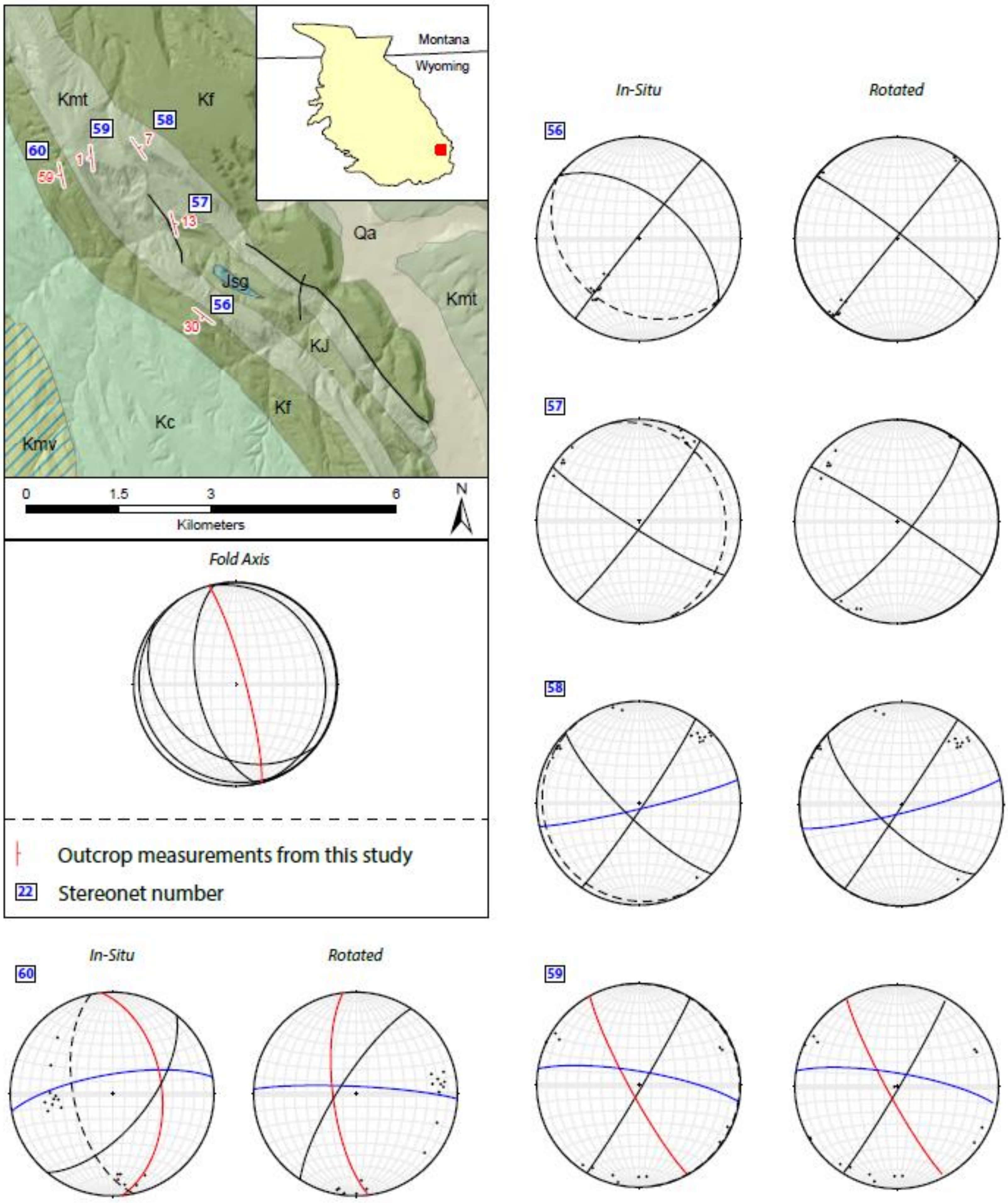

Figure 26: Tensleep anticline fracture analysis results. Geologic map above displays outcrop locations as well as bedding orientation measurements. Both in-situ and rotated stereonets are presented for each outcrop location. Dots represent the pole to fracture planes. Blue lines represent AC (dip) fractures and red lines represent BC (strike) fractures in relationship to the fold hinge. Black lines are oblique fractures. Dashed lines represent original bedding orientation. Fold axis classification is calculated from bedding orientations.

Manderson Anticline

Overview

Manderson anticline (MA) is an elongate (12 km by 3 km) structure located in the east central part of the BHB. Similar to many of the other anticlines included in this study, it exposes Cretaceous Cody Shale at its core. The limbs of the anticline are comprised of Cretaceous Cloverly Formation, Mowry Shale and Frontier Formation. Due to only a thin strip of Cody Shale present in the core, the center of the anticline has more topographic relief than other anticlines studied. From west to east the elevation of the anticline gently rises as much as 100 m with the east limb's ridge representing the highest point. No major surface exposed faults are mapped across the anticline. Only the northern two-thirds of the anticline were studied in outcrop due to limited land accessibility in the south.

Fold Classification

Manderson anticline, like other anticlines in BHB, is a non-cylindrical, asymmetric, doubly-plunging anticline. The folds axial plane was calculated from eight field collected bedding orientation measurements. Only the north axis was calculated. It's axial surface strikes 152° with an 84°SW dip with a fold axis plunging 8° in the direction of 330°. From the geologic map, the fold hinge line displays a linear trend. The eastern limb generally has a steeper dip than the western limb with values of 16°-52E° and 8°-22°W, respectively. This is also apparent from the apparent thickness of formations on the geologic map when comparing the west section to the eastern one.

Lineament Analysis

Across the northern section of MA, 248 lineaments were compiled from Google Earth Pro (Figure 27). Similar to the majority of anticlines, the strike (BC) lineaments are outnumbered by the dip (AC) lineaments. Strike (BC) lineaments trend 110°-150° whereas dip (AC) lineaments trend 30°-70°. Long strike (BC) lineaments define the ridges of the eastern limb and smaller sections of the western limb. Again, the dip (AC) lineaments are shorter in length and follow drainages within the center of the anticline as well as down the anticline limbs. Oblique lineaments are more common in an east-west orientation versus a north-south orientation. Lineaments trending roughly north-south often define erosive contacts between two adjacent lithologies.

Fracture Analysis

Seven outcrop fracture analysis were performed on the north section of the anticline and a single outcrop on the south side resulting in 121 fracture measurements (Table 9, Figure 28). MA outcrops contain four systematic fracture sets as well as one non-systematic set. The four systematic sets consist of the general dip (AC) and strike (BC) fractures as well as two nearly perpendicular fractures at both a high and low angle to the hinge line (oblique 1 and oblique 2). Dip (AC) fractures trend between 43° and 71° (average 61°) with an 80° dip. Strike (BC) fractures trend between 136° and 157° (average 148°) with an 82° dip. Oblique fracture set 1 on average trends at 35° with an81° dip whereas oblique fracture set 2 trends at 114° with an 87° dip, making these two sets nearly perpendicular. Comparing the trends of the oblique fracture sets to the fold

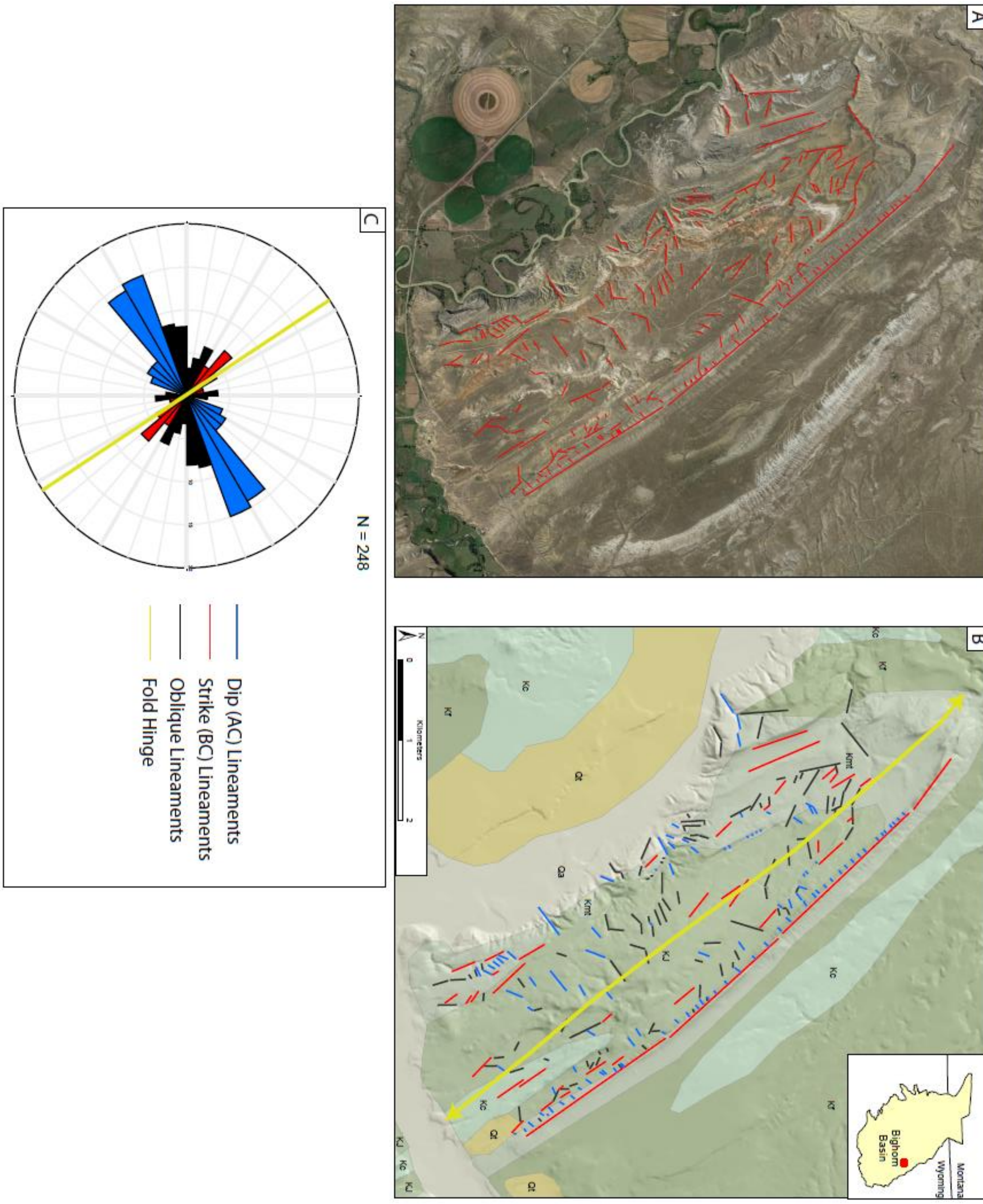

Figure 27: Lineament results of Manderson Anticline. A) Lineaments compiled from Google Earth Pro satellite imagery. B) Same lineaments classified by their orientation with respect to the fold hinge trend overlain on the Wyoming State Geological Society geologic map and USGS NED hillshade. For geology units symbology and classification refer to Appendix A. C) Rose diagram of lineaments classified by their orientation to the fold axis. Dip (AC) and strike (BC) lineaments represent a 15° buffer to being perpendicular and parallel to the fold hinge orientation, respectively.

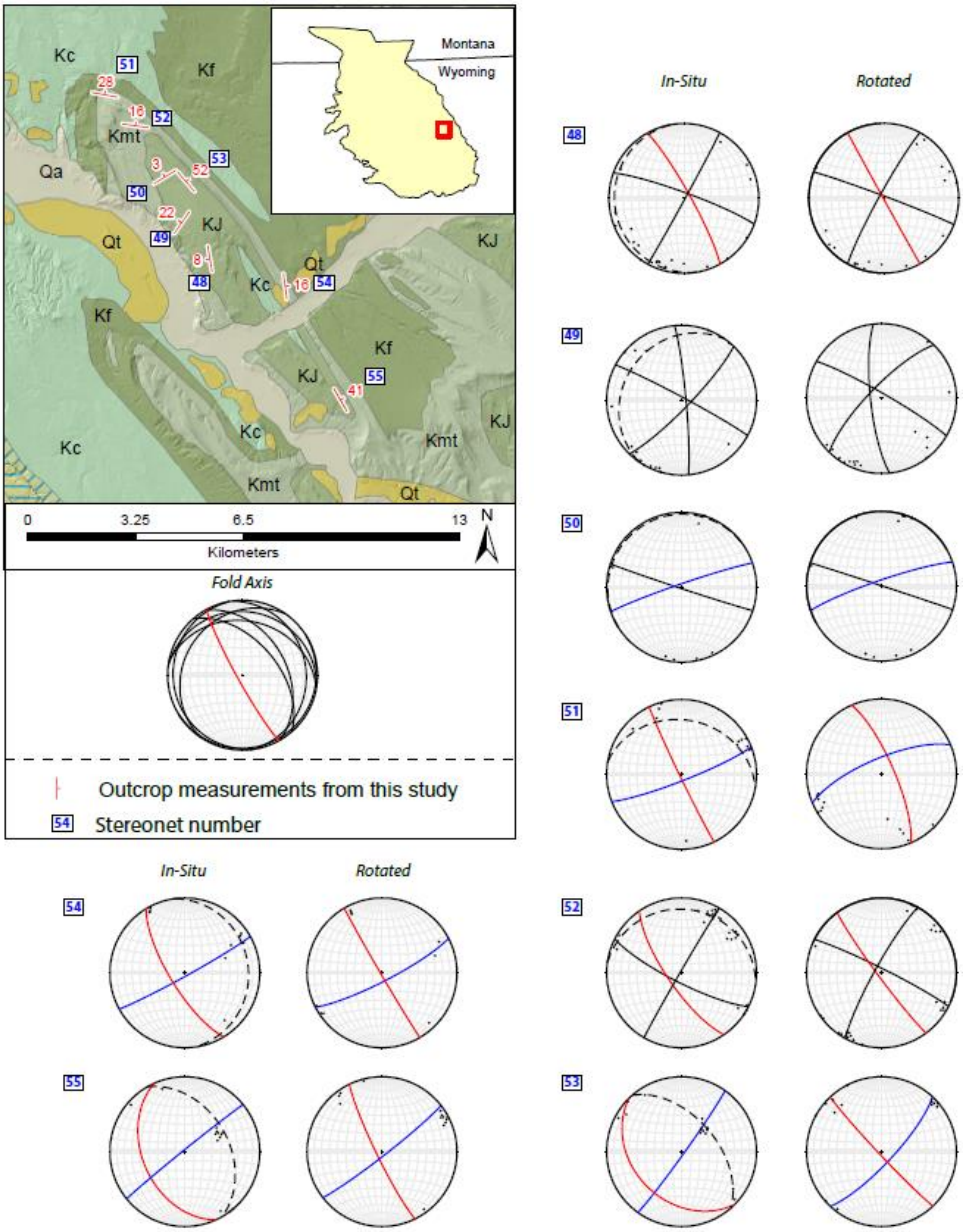

Figure 28: Manderson Anticline fracture analysis results. Geologic map above displays outcrop locations as well as bedding orientation measurements. Both in-situ and rotated stereonets are presented for each outcrop location. Dots represent the pole to fracture planes. Blue lines represent AC (dip) fractures and red lines represent BC (strike) fractures in relationship to the fold hinge. Black lines are oblique fractures. Dashed lines represent original bedding orientation. Fold axis classification is calculated from bedding orientations.

Rotated Fracture Orientation to Horizontal												
Stereonet #	AC Strike	AC Trend	AC Dip	BC Strike	BC Trend	BC Dip	O1 Strike	O1 Trend	O1 Dip	O2 Strike	O2 Trend	O2 Dip
48				152	152	90	210	30	85	291	111	88
49							225	45	77	300	120	84
50	251	71	83							109	109	90
51	247	67	73	337	157	76						
52				144	144	86	209	29	82	297	117	86
53	43	43	78	136	136	87						
54	62	62	87	149	149	73						
55	53	53	86	154	154	84						
Average		**61**	**80**		**148**	**82**		**35**	**81**		**114**	**87**

Table 8: Manderson anticline fracture analysis results. Stereonet/outcrop numbers correlate to numbers listed in Figure 27. All fractures are unfolded and rotated back to horizontal bedding orientation.

axis of 152° indicates that oblique set 1 is at a high angle and oblique set 2 at a low angle to the fold axis.

Garland Basin

Overview

Garland Basin (GB) is located in the north-central part of the BHB just east of Powell, Wyoming. Its dimensions are 18 km by 6.5 km although only the northern two-thirds of the anticline were considered for this study as the southern third is heavily altered by agriculture and inaccessible due to private land ownership. Overall, GB has the least topographic relief of all the anticlines with only 50 m of elevation difference. The core of the anticline is heavily altered by hydrocarbon extraction infrastructure and was thus avoided in both lineament and outcrop fracture analysis. Similar to many other anticlines in the BHB, the core of the anticline exposes Cretaceous Cody Shale surrounded by limbs consisting of Cretaceous Mesaverde Group and Meeteetse Formation. The anticline is also the most heavily faulted structure of this study with faults ranging from 1 km to 10 km in map trace and segmenting the entire anticline. All faults follow a general southwest to northeast trend and are dominantly mapped as normal faults.

Fold Classification

The axial surface was classified from nine bedding orientations measure across the northern section of the anticline with a result of a 136° strike and a 78°SW dip. Similar to the axial surface, the hinge line trend also follows a 136° azimuth and barely plunges at 1° to the northwest. The surface trace of the fold axis is linear. The anticline can be classified as a non-cylindrical, asymmetric, plunging fold. The east limb of the anticline dips at higher angles of 18E° to 54°E when juxtaposed to the low angle west limb of 2°W to 20°W. However, the high density of faulting can also offset these values by local fault block rotation.

Lineament Analysis

Across GB, only 110 lineaments were extracted from Google Earth Pro due to its low structural relief and heavy anthropogenic alteration in its center (Figure 29). The low relief greatly reduces the number of dip (AC) lineaments as these tend to form in drainages on the steep limbs of the anticline. GB is the only anticline included in this study where dip (AC) lineaments actually outnumber the strike (BC) lineaments. Dip (AC) lineaments trend at an azimuth of 20° to 60° whereas strike (BC) lineaments have an azimuth of 110° to 150°. An oblique set of lineaments with an azimuth of

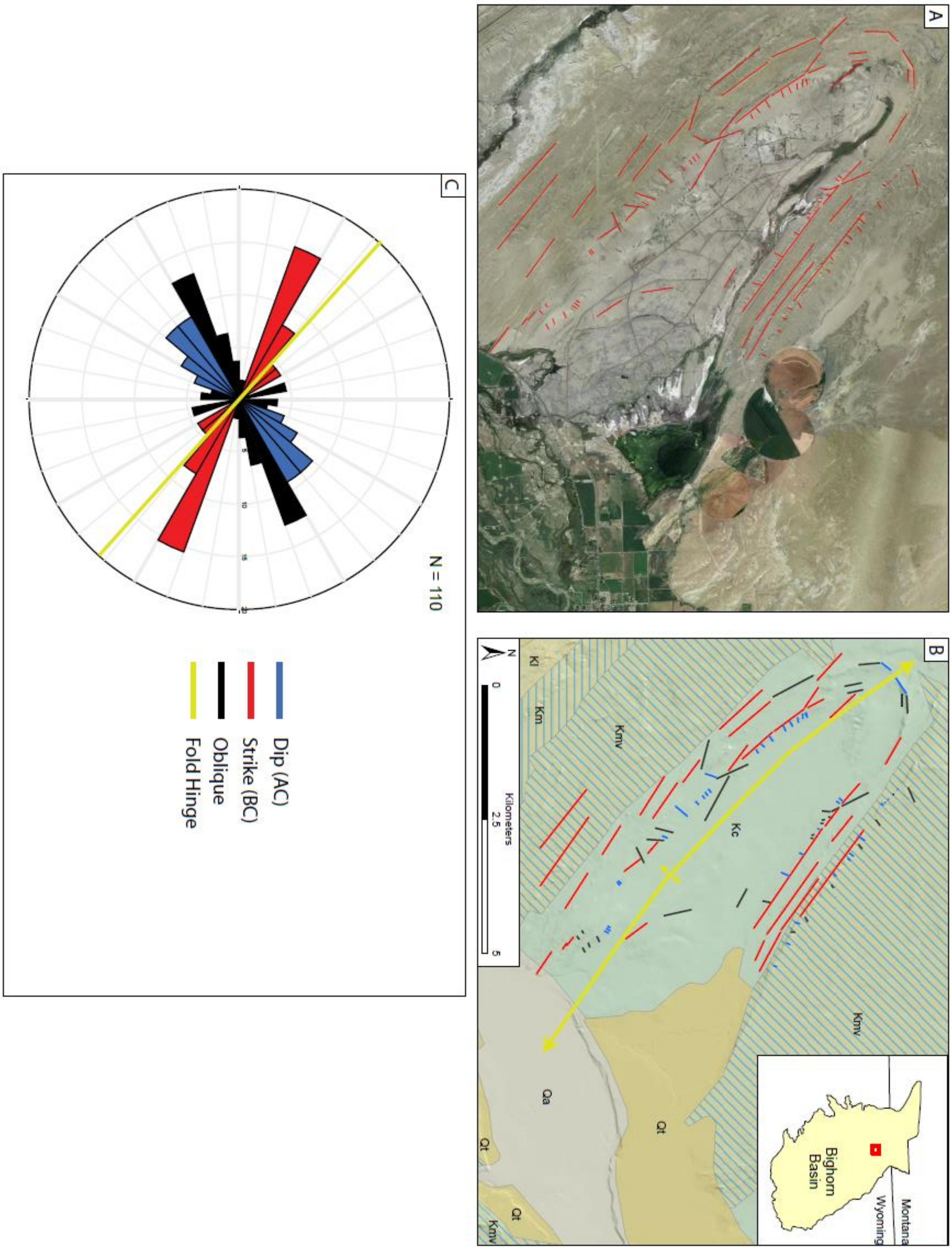

Figure 29: Lineament results of Garland Basin. A) Lineaments compiled from Google Earth Pro satellite imagery. B) Same lineaments classified by their orientation with respect to the fold hinge trend overlain on the Wyoming State Geological Society geologic map and USGS NED hillshade. For geology units symbology and classification refer to Appendix A. C) Rose diagram of lineaments classified by their orientation to the fold axis. Dip (AC) and strike (BC) lineaments represent a 15° buffer to being perpendicular and parallel to the fold hinge orientation, respectively.

approximately 65° have a high occurrence that could be related to a slight clockwise rotation of the fold axis at the northern end of the anticline. Long ridges and valleys associated with mechanically weak and resistant lithologies along the limbs define the strike (BC) lineaments whereas short eroded down dip drainages define the dip (AC) lineaments.

<u>Fracture Analysis</u>

Nine outcrops were examined in the field for fracture measurements located mainly on the northern half of the anticline resulting in 135 fracture measurements (Table 9; Figure 30). The resulting measurements indicate four unique fracture sets when

	Rotated Fracture Orientation to Horizontal											
Stereonet	**AC Strike**	**AC Trend**	**AC Dip**	**BC Strike**	**BC Trend**	**BC Dip**	**O1 Strike**	**O1 Trend**	**O1 Dip**	**O2 Strike**	**O2 Trend**	**O2 Dip**
39										157	157	85
40				147	147	71				175	175	63
41				144	144	72	204	24	86	167	167	72
42	53	53	84	319	139	81	9	9	81			
43	41	41	82	130	130	88						
44	223	43	83							338	158	81
45	39	39	87	311	131	81						
46							31	31	75	342	162	89
47										351	171	61
Average		**44**	**84**		**138**	**79**		**21**	**81**		**165**	**75**

Table 9: Garland Basin fracture analysis results. Stereonet/outcrop numbers correlate to numbers listed in Figure 29. All fractures are unfolded and rotated back to horizontal bedding orientation.

the bedding planes are unfolded and rotated back to horizontal: (1) dip (AC) fractures, (2) strike (BC) fractures, (3) oblique 1 fractures, and (4) oblique 2 fractures. Dip (AC) fractures trend between 39° and 53° with an average dip of 84°. Approximate perpendicular to the dip (AC) fractures, the strike (BC) fractures trend at between 130° and 147° with an average dip of 79°. The oblique fractures in this anticline have a

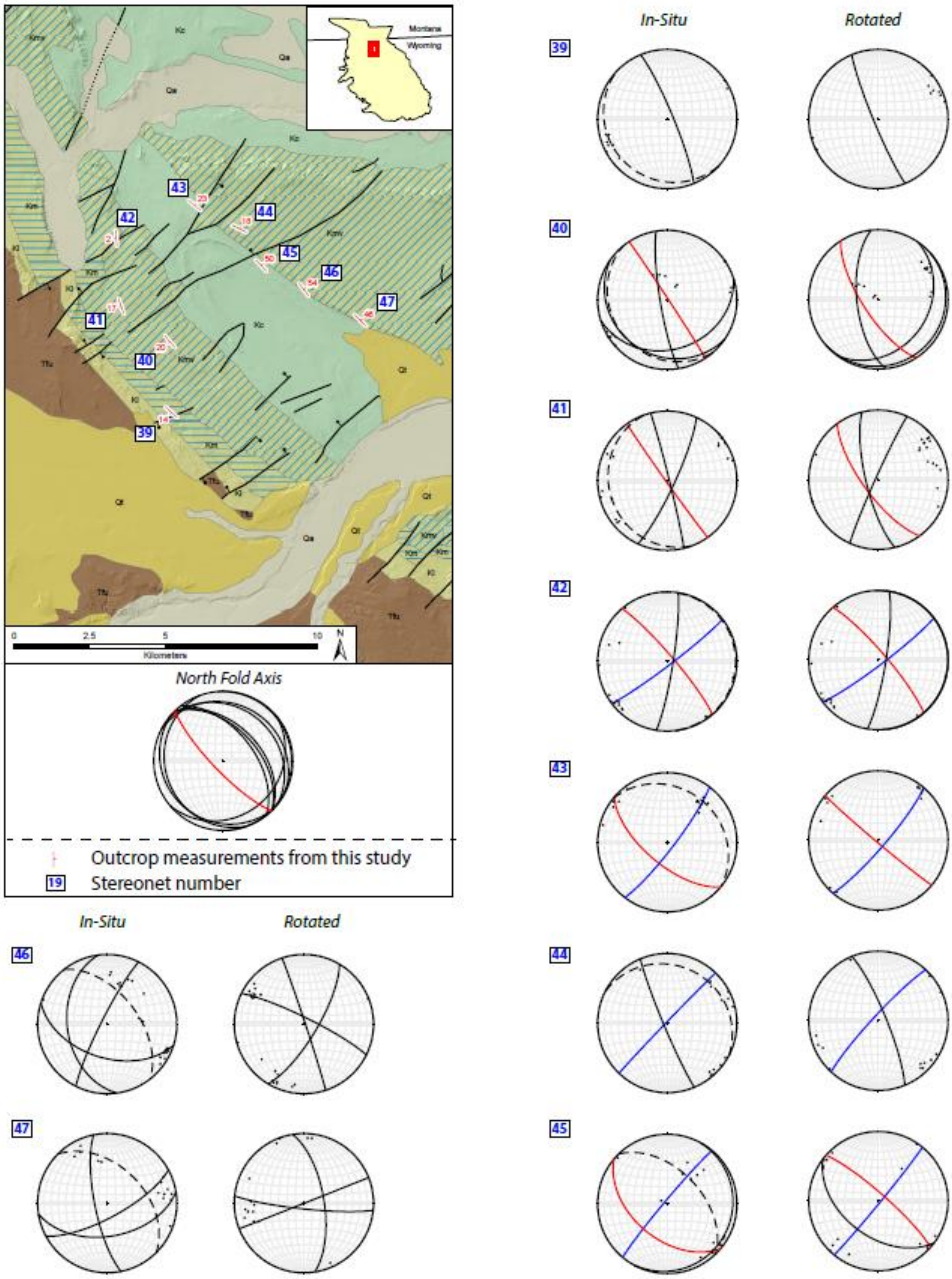

Figure 30: Garland Basin fracture analysis results. Geologic map above displays outcrop locations as well as bedding orientation measurements. Both in-situ and rotated stereonets are presented for each outcrop location. Dots represent the pole to fracture planes. Blue lines represent AC (dip) fractures and red lines represent BC (strike) fractures in relationship to the fold hinge. Black lines are oblique fractures. Dashed lines represent original bedding orientation. Fold axis classification is calculated from bedding orientations.

different relationship to each other when compared to other studied anticlines in the basin. The two oblique fracture sets do not occur near perpendicular or conjugate to each other as seen in other anticlines. Oblique fracture set 1 are not as common, only occurring in three outcrops, and trend on average at 21° with an 81° dip. Oblique fracture set 2 however, occur in six outcrops with an average trend of 165° and a dip of 75°. This places them 140° apart from each other giving them a different relationship than elsewhere in the basin.

Results Summary

Across the nine anticlines examined in the BHB, 953 fractures were measured, resulting in four dominant fracture sets were identified across all anticlines, but were not present at every outcrop studied. When rotated back to horizontal these four sets are: (1) sub-parallel to the hinge line labeled as strike (BC) fractures (average angle from hinge line of 9°), (2) sub-perpendicular labeled as dip (AC) fracture (average angle from hinge line of 86°), (3) oblique to the hinge line trending SSW-NNE labeled oblique 1 (average acute angle from hinge line of 54°), and (4) oblique to hinge line trending SSE-NNW labeled oblique 2 (average acute angle from hinge line of 45°) (Table 10; Figure 31). Fracture formation is highly determined by the buckling and bending of layers associated with folding. Thus, fracture sets were determined based on their relationship to the hinge line trend as this method provided a correlation across an individual anticline that can be compared to adjacent anticline.

Rotated Fracture Orientations to Horizontal					
Anticline	**Fold Axis (FA) Trend**	**AC Trend**	**BC Trend**	**Oblique 1 (O1) Trend**	**Oblique 2 (O2) Trend**
North Elk Basin	155	78	160	38	131
South Elk Basin	182		175	41	126
Horse Center Anticline	165	86	185	28	132
North Oregon Basin	135	36	150	18	86
South Oregon Basin	149	46	150	18	92
North Little Buffalo Basin	156	73	150	20	104
South Little Buffalo Basin	149	59		23	98
Grass Creek Anticline	158	75	130	45	104
Garland Basin	136	44	138	21	81
Manderson Anticline	152	61	148	35	114
Tensleep Anticline	162	89	163	35	128
Thermopolis Anticline	114	37	102	22	74
Average without Thermopolis	**154**	**65**	**155**	**29**	**109**
Standard Deviation w/o Thermopolis	**13**	**18**	**15**	**9**	**19**

Table 10: Fracture comparison of all studied anticlines across the basin. Anticlines with a sinuous fold axis are divided up into a northern and southern section. Fracture orientations are listed by trends rather than strike for easier comparison. Basin wide average values calculated at the bottom of the table exclude Thermopolis anticline as it behaves differently from the rest of the anticlines. See the discussion section for further information on Thermopolis anticline.

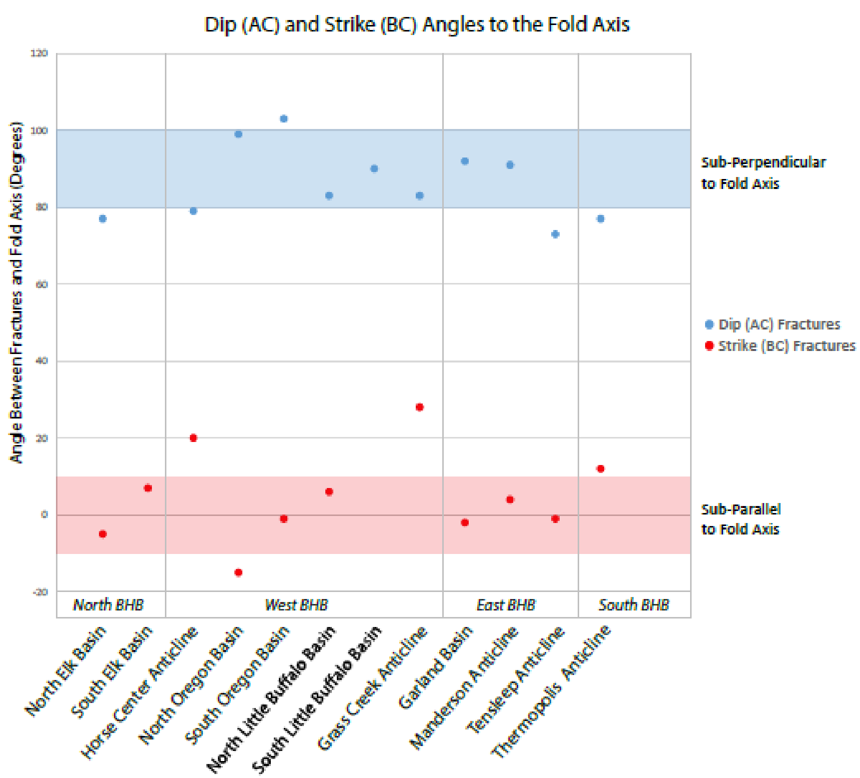

Figure 31: Dip (AC) and strike (BC) fracture relationships to the respective hinge line trend. Dots represent the angle of each fracture set to the hinge line calculated from fracture set averages of each anticline. Grass Creek anticline only includes two measurements, which may result in the large offset of strike (BC) fractures.

Furthermore, the fold's axial surface governs the hinge line trend and orientation of surrounding limbs. Fold hinge lines across the western and eastern sides of the BHB trend at a more SSE-NWN orientation when compared to Thermopolis anticline in the south which trends at a SEE-WNW azimuth, thus an individual fold scale comparison is required. A simple, direct comparison of fracture orientation regardless of hinge line trend across all folds across the entire basin reveals no systematic sets.

Dip (AC) and strike (BC) fractures are the most consistent across the basin. Dip (AC) fractures have a standard deviation of 9° from being perfectly perpendicular to the hinge line. Strike (BC) fractures have a standard deviation of 11° from the hinge line. Oblique fracture set 1 and set 2 have a standard deviation of 9° and 11° respectively. Another geometric measurement considered is the inter-angle between both dip (AC) and strike (BC) fractures as well as oblique sets 1 and 2. As expected, the angle between dip (AC) and strike (BC) fractures is close to perpendicular with an average of 85°; however, with a standard deviation of 15°. The average between oblique set 1 and oblique set 2 is 77° with a standard deviation of 14°.

Anticline	Fold Axis (FA) Trend	AC Angle to FA	BC Angle to FA	O1 Angle to FA	O2 Angle to FA	Angle b/w O1 and O2	Angle b/w AC and BC
North Elk Basin	155	77	5	63	24	93	82
South Elk Basin	182		7	39	56	85	
Horse Center Anticline	165	79	20	43	33	104	81
North Oregon Basin	135	99	15	63	49	68	114
South Oregon Basin	149	103	1	49	57	74	104
North Little Buffalo Basin	156	83	6	44	52	84	77
South Little Buffalo Basin	149	90		54	51	75	
Grass Creek Anticline	158	83	28	67	54	59	55
Garland Basin	136	92	2	65	55	60	94
Manderson Anticline	152	91	4	63	38	79	87
Tensleep Anticline	162	73	1	53	34	93	74
Thermopolis Anticline	114	77	12	44	40	52	65
Average without Thermopolis	**154**	**86**	**9**	**54**	**45**	**77**	**85**
Standard Deviation w/o Thermopolis	**13**	**9**	**11**	**9**	**11**	**14**	**15**

Table 11: Angular relationships between individual fracture sets and respective anticline fold axis. Average trend values for each fracture sets are compiled from the individual anticline result tables listed above. Total average values and standard deviations calculated for each anticline exclude Thermopolis anticline due to its unique structural orientation.

DISCUSSION

Overview

The following discussion relates the lineament and fracture analysis results starting at the scale of an individual anticline to regional tectonic domains within the BHB, and finally to the regional shortening direction of the Laramide Orogeny. Whereas entire publications, dissertations and decade long research have been dedicated to studying fractures within one anticline to determine geometric, kinematic, and confident age relationships between fractures, this study attempts to relate a basin wide geometric study of fractures to regional structural features (Bellahsen et al., 2006; Fiore, 2006; Beaudoin et al., 2011; Beaudoin et al., 2012)

Correlation of Google Earth Pro Lineaments and Outcrop Fractures

With increasing availability of high resolution aerial imagery draped over a terrain interpolated from digital elevation models, the ability to conduct fast, inexpensive preliminary geologic research on an area has increased dramatically. The lineament collection methods included in this research, first developed by Lageson et al. (2012), were field checked with rock outcrop fracture measurements. Overall there is a positive correlation between the trends of lineaments and fracture trends in the field.

The four fracture sets consistently identified in the field (dip (AC), strike (BC), oblique set 1, and oblique set 2) are well expressed in rose diagrams. Dip (AC) lineaments dominate all anticlines in number (except Tensleep anticline) with strike (BC) lineaments mainly representing the least common set. The two oblique sets are locally expressed as lineaments, but never outnumber the dip (AC) lineaments. Similar to fracture orientations, lineament orientations are most easily correlated to the trend of the hinge line rather than a regionally dictated orientation. Since fractures in the field were not collected based on a density method, the correlation between the numbers of lineaments versus fracture density cannot be concluded from this study. However, the author believes that the identification of systematic lineaments is a valid preliminary method and can be used on large regions otherwise impossible to study. For example, Erslev and Koenig (2009) conducted a regional (Montana, Utah, Wyoming, Colorado, New Mexico) wide study based on orientations of fold axis and faults extracted from geologic maps to show systematic changes of Laramide shortening direction. Although this study included surface mapped data (not remotely sensed), the ability to extract lineaments at any given scale can provide a new scale that was previously not possible to study remotely.

Fractures Associated with an Individual Anticline

Fracture Complexity

Over the past half century, many publications have dealt with the complex topic of how fractures form in a rock, how they propagate, and the controlling rock properties that determine natural fracture formation (Nelson, 1985; Fjaer et al., 1992; Lorenz, 1997). The current standing of research indicates that some of the main variables determining fracture formation and spacing are: stress orientation, bed thickness, brittle rock constituents, Young's modulus, rock tensile strength and porosity (Cooper et al., 2001). In order to most successfully understand the formation, propagation, and timing of fractures, all of these factors must be considered. Geologists have derived many mathematical equations from empirical data in attempts to model these parameters, especially focusing on bed thickness and its influence on fracture density (Hobbs, 1967; Price, 1966; Ladeira and Price, 1981; Bai and Pollard, 2000).

Bed thickness as well as bed composition are two of the main governing factors of fracture formation and density. Bed thickness can vary systematically based on depositional environments, but it can also change during the folding of strata of different mechanical competency. Hayes and Hanks (2008) examined a detachment fold in the Carboniferous Lisburne Group in Alaska and determined that a less competent mudstone bed situated between two more competent beds thickened towards the hinge during folding and displayed different fracture sets than the surrounding competent units. Although the stratigraphy in Hayes and Hanks (2008) is different from that studied in the BHB, the underlying concept holds true. The main stratigraphy included in this study, Jurassic and Cretaceous units, are interbedded mudstone, siltstone and sandstone. Each one of these lithologies has a different competency and even within one single, continuous sandstone bed, differences in porosity and cementation can exist leading to mechanical differences. These changes in lithology can lead to localized fracture formation.

Fracture formation in a fold is further complicated by changes in local stress regimes. Although the general trend of the hinge line is determined by the more regional stress orientation, which also has a large influence on fracture formation, local stress changes associated with the flexing and bending of folds also dictate fracture formation (Price and Cosgrove, 1990). The highest density of fractures is usually related to the maximum curvature of the fold at the fold hinge (Savage et al., 2010). As an individual layer flexes, its outer arc tends to be pulled apart creating a series of tensile fractures whereas the inner arc produces its own fractures (Figure 32). Utilizing the plate bending theory, the along strike joints formed on the outer arc are perpendicular to the joints formed on the inner arc (Savage et al., 2010).This idea has both been modeled in laboratories as well as confirmed in the field (Savage et al., 2010). Cooke (1997) identified the hinge joint set on East Kaibab Monocline, Utah as he had predicted by numerical models with only small discrepancies resulting from the heterogeneous nature of the natural rock versus his models assumption. Savage et al. (2010) expanded this idea by moving away from Cooke's simple monocline to examining the north plunging nose of Sheep Mountain anticline in the BHB. At Sheep Mountain anticline Savage et al. (2008) identified joints with orientations of both the outer and inner arc; however, the joints were more related to mechanically competent and incompetent layers. The reviewed research here suggests that fracture complexity across the hinge zone and the noses of the anticline can be much more intricate that either of the dipping limbs.

Lastly, local less than 10 km long faults across anticlines or anticlines near greater than 10 km in length faults (e.g. Owl Creek Fault System and Tensleep Fault) can cause a local stress rotation resulting in fracture orientations not found elsewhere in the basin (Savage et al., 2010). The Nye-Bowler lineament to the north, although not one through

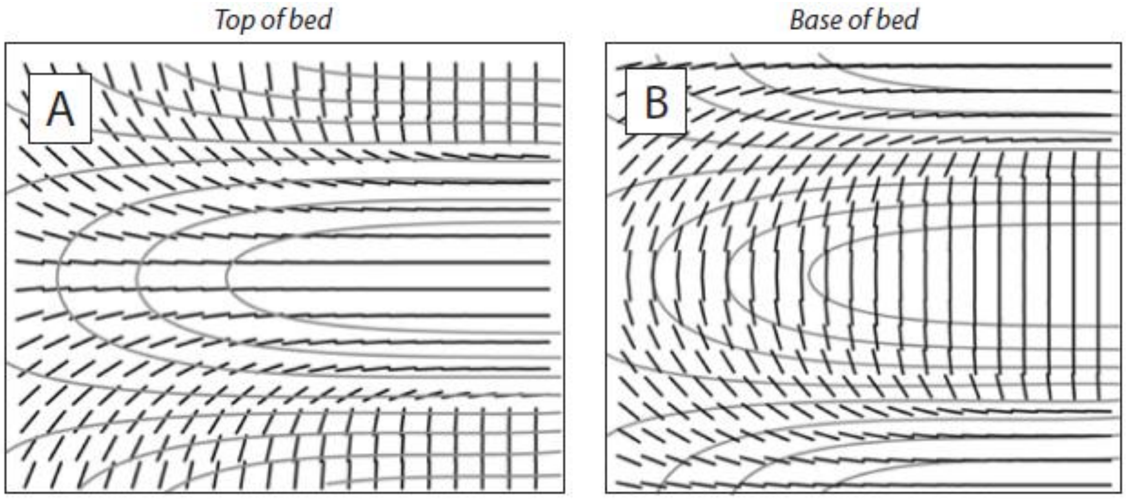

Figure 32: Predicted joint orientation and patterns across a plunging fold. Gray lines in the background are structure contours of the fold. A) Strike orientation joints at the top of a folded bed as suggested by a numerical plate bending model with maximum curvature at the top of the bed. B) Strike orientation joints at the base of a folded bed as suggested by a numerical plate bending model with maximum curvature at the top of the bed. Figure modified from Savage et al. (2010).

going fault, can also be considered as one of these structures. All three of these faults (Tensleep fault, Nye-Bowler Lineament, Owl Creek Mountain's faults) trend roughly east-west. Assuming a Laramide shortening direction of 055-060° N, the faults' oblique orientation suggest a combination of dip-slip and strike-slip movement across the surface. Although this geometry and mechanism does not directly apply fault block rotation, minimal rotation may occur. From the fracture complexities explained above, fault block rotation probably contributes the least amount to changes in fracture orientation but is a fracture complexity to be considered.

<u>Fracture Timing Based on Geometry</u>

There is a systematic relationship between fracture orientations rotated to original horizontal bedding and the trend of the fold axis, as shown by measurements in this study. Combining the geometry of fractures in relationship to (1) the hinge line of each individual anticline as well as average fracture to hinge line relationship values across the basin, (2) the assumed Laramide shortening direction of 055-060°, and (3) previous related fracture formation studies, inferences can be made about relative timing of fracture formation. Over the past half century, numerous studies across the BHB and the greater Laramide province focused on fracture formation and orientations (Allison, 1983; Garfield et al., 1992; Englender et al., 1997; Cooper et al., 1998; Hennings et al., 2000; Wicks et al., 2000; Silliphant et al., 2002; Bellahsen et al., 2006, Fiore, 2006; Beaudoin et al., 2011, Beaudoin et al., 2012). These studies mainly focused on individual, or sections of, folded structures with methods including strictly geometric, microscopic fracture, calcite twins, x-ray diffraction, cathodoluminescence, stable isotope analysis and rock core interpretations. Although not all focused on the BHB, the combination of knowledge gathered from these Laramide related studies provide valuable insight on the mechanism and timing fracture formation as a result of the Laramide orogeny.

The four fracture sets classified in this study are best analyzed based on their geometry as this is the most dominant and complete data set collected along with outcrop field notes. Past field studies on fracture formation and timing in anticlines as well as laboratory models with deep seated thrust faults provide a preliminary basis for extracting the geometric history of fractures in the BHB (Cooke, 1997; Bergbauer et al., 2004; Hayes et al., 2008; Savage et al., 2010). The fracture sets identified in this study can be associated with different stages of folding when comparing their geometry to the

Laramide shortening direction and previous detailed studies on timing of region wide fractures.

Pre-Folding fractures

Oblique fracture set 2, is a mode I fracture set ranging from trends of 81-128° across the BHB (average 101°, excluding east-west trending Thermopolis anticline) and is a commonly accepted as a pre-folding fracture set across the Laramide province (Figure 33). Hennings et al. (2000) identified this set at Oil Mountain, Wyoming, Silliphant et al. (2002) at Split Mountain, Utah, Bergbauer et al. (2004) at Emigrant Gap anticline, Wyoming and Wicks et al., (2000) in the Black Hills of northeastern Wyoming all determining this as the earliest set. Evidence that these fractures predate folding stems from the occurrence of these fractures in undeformed strata surrounding anticlines as well as systematically distributed across entire anticlines with younger fracture abutting onto them (Bergbauer et al., 2004). A similar orientation fracture set is also identified at the Tensleep fault but of younger age and associated with movement on the fault (Allison, 1983). Since joints form in a direction parallel to the maximum principle stress, the orientation of this joint set indicates an earlier east-west directed shortening before a counterclockwise rotation to the Laramide shortening direction. Although abutting relationships in the field were often difficult to determine due to lack of along dip exposure, outcrop numbers 23, 48, 52 and 57 display oblique fracture set 2 terminating both oblique fracture set 1 and strike (BC) fractures (Figure 34). However, at certain outcrops the trend of oblique set 1 and strike (BC) are within 15° of each other and may be considered a single fracture set.

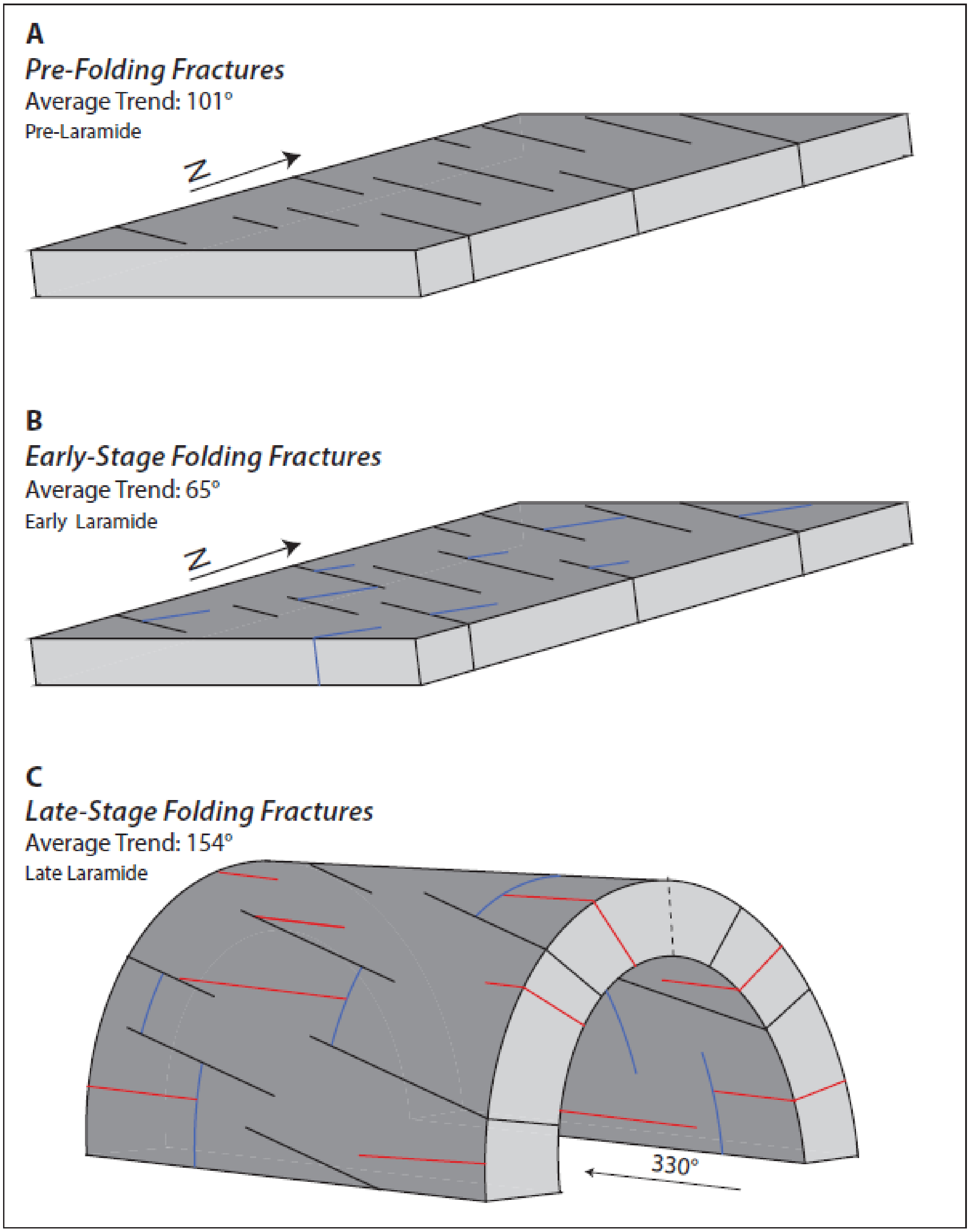

Figure 33: Timing and orientation of fracture formation across anticlines within the Bighorn Basin. A) Pre-folding fractures oriented at an average trend of 101°. B) Onset of folding produces a fold hinge and bedding perpendicular fracture set with an average trend of 65° correlating well with Laramide shortening direction. C) Late-stage folding fractures sub-parallel to the fold hinge and perpendicular to bedding with an average trend of 154°.

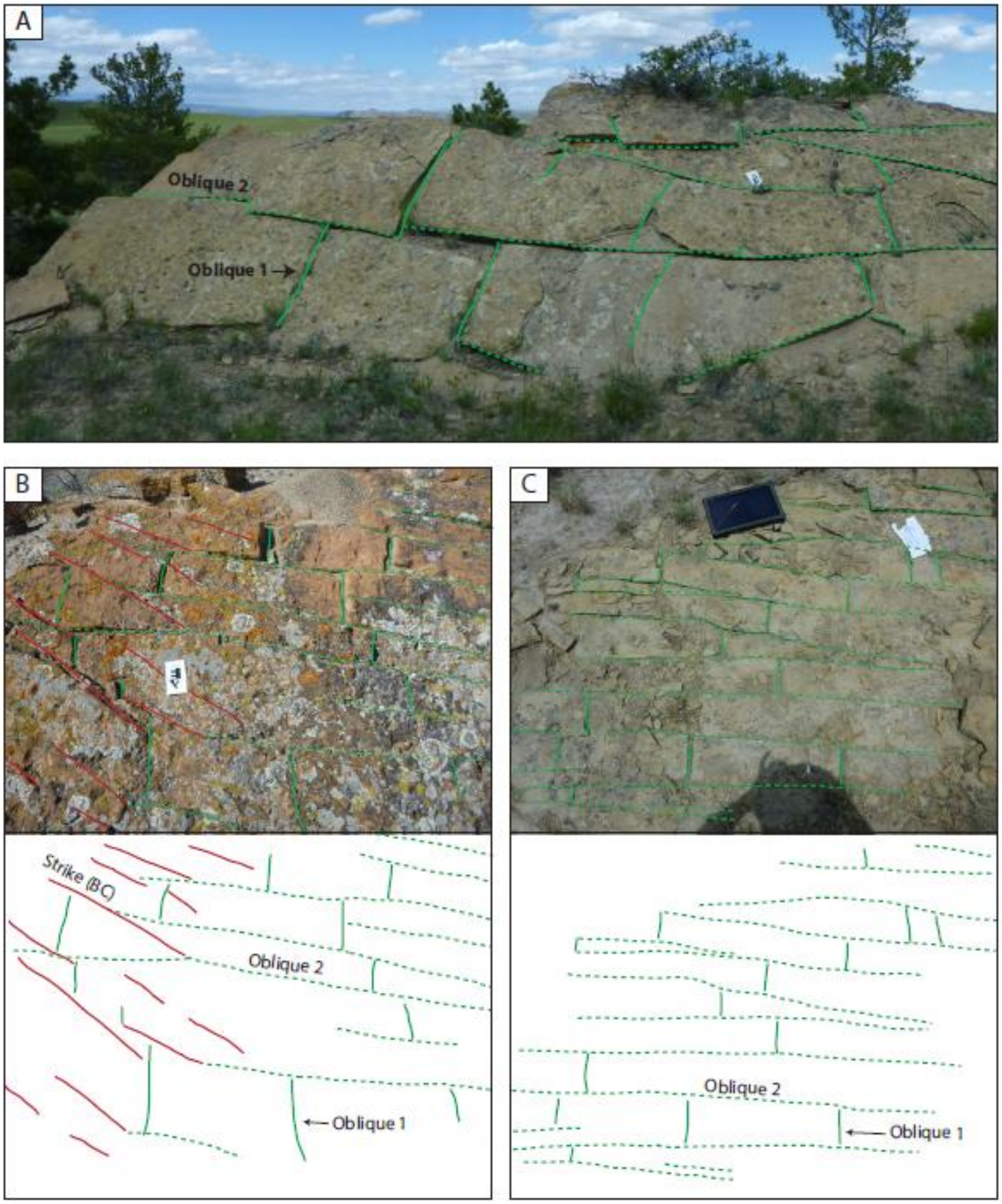

Figure 34: Field evidence indicating pre-folding fractures. Abutting relationship indicates oblique 2 fractures pre-dating both oblique 1 and strike (BC) fractures. North arrow in picture is approximately 20 cm long for scale.

<u>Early-Stage Folding Fractures</u>

As Laramide shortening continued and the early stages of fold growth began, dip (AC) fractures formed sub-perpendicular to the fold hinge sub-parallel to Laramide shortening direction of 055-060° N (Neely and Erslev, 2009). Excluding Thermopolis anticline due to its more east-west directed fold axis, the average trend of these bedding perpendicular fractures across all other anticlines is 65° with an 18° standard deviation. This fracture set is interpreted to be related to the onset of Laramide shortening due to its average trend correlating to the expected joint formation orientation parallel to maximum compression (δ_1). The large standard deviation value may be related to local perturbations away from the central portions of each limb. Moving away from the limb regions into the noses, local stress changes change due to the doubly-plunging nature of the anticlines. As described in Savage et al., (2010) in both a mathematical model and proven in the field, the outer arc of a bed experiences different local stress regimes in the nose region of a plunging fold (Figure 32). In the model, dip (AC) joints gradually turn towards a fold parallel orientation as they reach the hinge line on the nose of the anticline possibly creating the large standard deviation.

Outcrop number 12 in Oregon Basin depicts strike (BC) joints terminating against dip (AC) joints. No consistent age relationship was determined between dip (AC) fractures and oblique fracture set 2 in the field. Where both fracture sets occurred in the same outcrop, poor lateral exposure hindered from extracting cross cutting relationships, thus the analysis of timing presented here is based on geometry and previous research.

Late-Stage Folding Fracture

The last-stage folding fractures are related to the fold reaching its maximum curvature at the fold hinge and increased influence of local stress regimes over the previously governing Laramide shortening direction. These strike (BC) fractures are related to the outer arc of a bed being extended in a direction perpendicular to the fold hinge creating joint sets bedding perpendicular and sub-parallel to the fold axis. The average trend of folds across the basin (excluding the genetically unique Thermopolis anticline) is 154° with a standard deviation of 13°. This trend accurately lines up with the average strike (BC) fractures with an average trend of 147° and a standard deviation of 10. Similar fractures were both observed at Teapot Dome and Emigrant Gap anticline, Wyoming (Cooper et al., 2001; Bergbauer et al., 2004). In the field at outcrop numbers 12 in Oregon Basin and at 69 in Horse Center anticline abutting relationships display strike (BC) joints terminating against dip (AC) joints.

Oblique fracture set 1 is also most likely associated with late stage folding. The general orientation of these fractures (SSW-NNE) is at an acute angle to the fold axis, thus relating them closer to strike (BC) fractures than dip (AC) fractures. A distinction between strike (BC) fractures and oblique fracture set 1 was sometimes difficult. Since the classification of strike (BC) fractures is based on being sub-parallel to the fold axis and many of the anticlines suggest a sinuous or curved fold axis the angle at a specific location between a fracture and the fold axis can be difficult to determine accurately. Oblique 1 fractures were also more dominant on fold limbs than towards the noses of anticlines. Stearns and Friedman (1972) identified a similar set of fractures on anticlines with the maximum principle stress perpendicular to the fold hinge However, their model accounted this fracture to be part of a conjugate fracture set about the maximum shortening direction. Although on at some outcrops this assumption holds true with the previously denoted temporally first fracture set, oblique set 2, being the conjugate pair, other anticlines display these two fractures perpendicular to each other (Figure 35). Definite age relationship between oblique fracture set 1 and the previously described fractures were not able to be determined in the field based on abutting relationships

Accuracy of Age Relationships

The fracture evolution described above is based on a combination of previous literature within the BHB, geometric studies of fracture formation in folds, as well as field data collected within this study. The broad scope of this project, examining nine anticline across the entire basin, makes accurate determination of ages difficult. Only Rattlesnake Mountain and Sheep Mountain anticlines within the BHB have fracture age relationships confidently determined. The amount of data and subsequent analysis required for extracting relative fracture ages confidently was outside of the scope of this project. A strictly geometric approach, as applied in this study, does not allow for accurate determination of ages. The timing of fractures discussed above were not present across all outcrops. Some fracture abutting relationships within the field reject the hypothesis presented in this study. Also, outcrops like number 4 in Horse Center anticline suggest three contemporaneous fracture sets as non truncate or offset each other (Figure 36). Thus, the conclusion of fracture formation and timing is only a preliminary idea based on

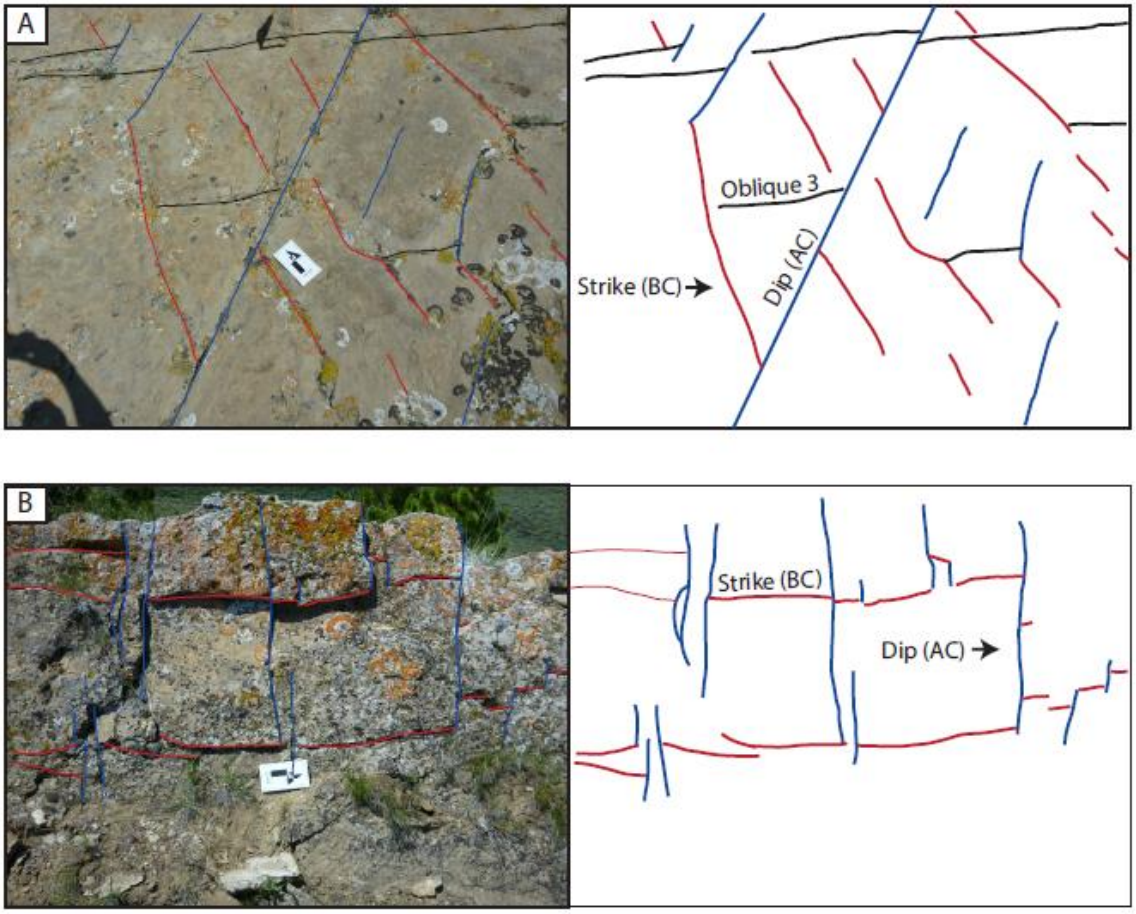

Figure 35: Field evidence indicating late-stage folding fractures. Abutting relationship indicates dip (AC) fractures pre-dating both oblique 3 and strike (BC) fractures. North arrow in picture is approximately 20 cm long for scale.

the combination of geometry and previous in-depth studies on individual anticlines. Many variables including relative location in the basin, stratigraphy exposed, subsurface fault geometry, size of anticline and rock properties all determine the fracture formation and timing. The scope of this research is to comment on basin wide variations of fracture orientations as related to adjacent large scale structures. This idea will be examined in the following section.

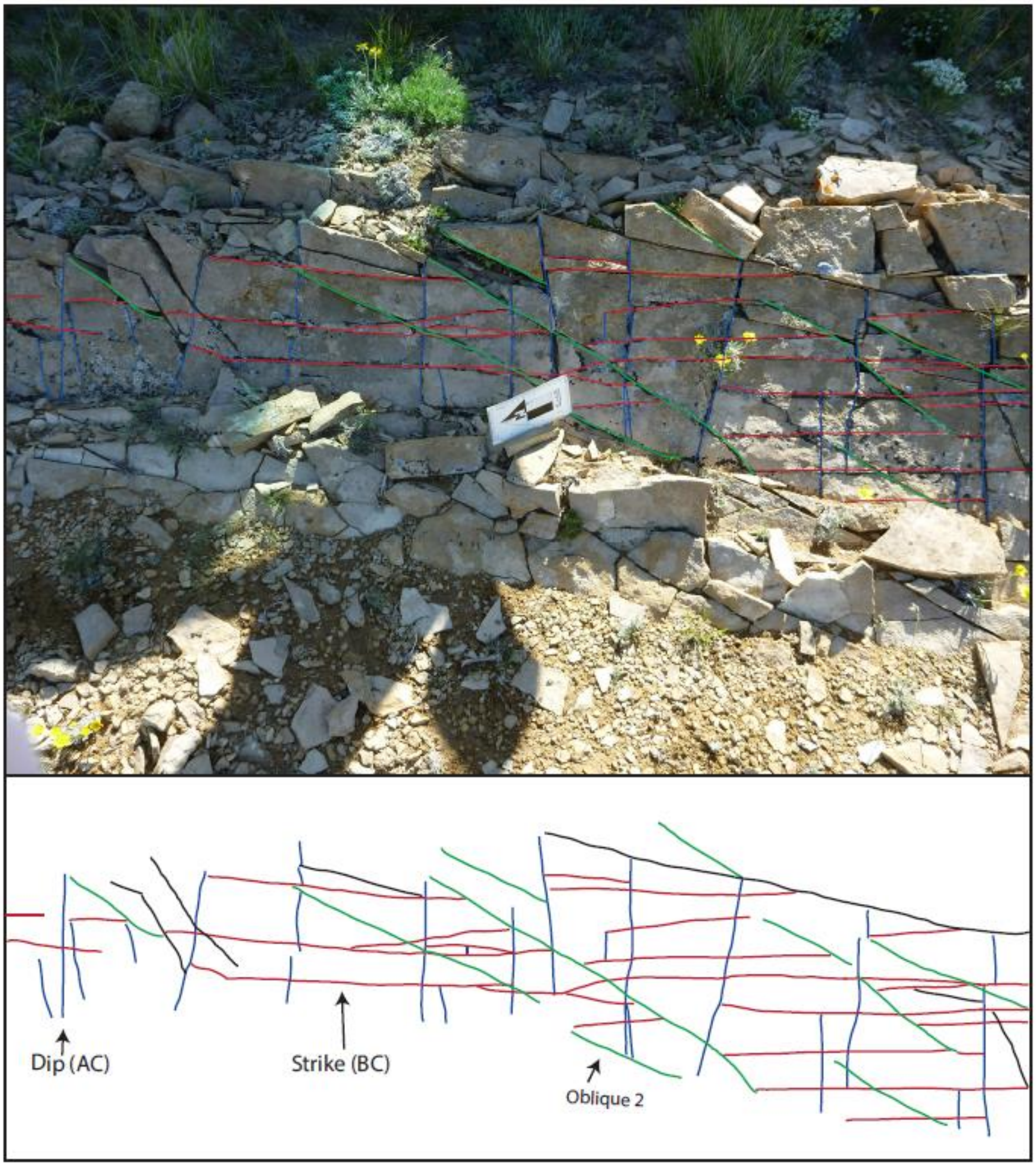

Figure 36: Field evidence of contemporaneous fractures. Outcrops similar to this one were encountered multiple times in the field. There is no evidence in this outcrop of age relationships between fractures from either abutting relationships or offset across fractures. North arrow approximately 20 cm for scale..

Tectonic Domains within the Bighorn Basin

West and East Tectonic Domain

The west and east side of the basin contain the majority of the anticlines examined in this study. Anticlines including Horse Center, Oregon Basin, Little Buffalo Basin, and Grass Creek anticlines define the west side of the basin, whereas Tensleep, Manderson, and Garland Basin anticlines define the east side. Overall, recorded fracture orientations in the field do not vary systematically between the anticlines. All have a sub-equal number of dip (AC), strike (BC) and oblique fractures. The fracture orientations are mainly governed by the trend of the hinge line. The average trend of the hinge lines on the west and east side of the BHB is 154° with a standard deviation of 13°. According to Brown (1993) thrust faults creating these anticlines form at an angle perpendicular to Laramide shortening. Even though the majority of published literature assumes a Laramide shortening direction of 045-055° N, Neely and Erslev (2009) determined a clockwise rotation of shortening moving north out of Utah into Colorado and Wyoming to a value of 060° N in northern Wyoming and the BHB. This new shortening direction is sub-perpendicular to the hinge line orientation of 154° correlating well with Brown's (1993) predicting of thrust fault and anticline orientation as related to the Laramide shortening direction.

The trend of individual hinge line across this domain vary between linear (Manderson anticline), to slightly curved (Little Buffalo Basin, Tensleep anticline), to significantly curved (Grass Creek anticline). The increased fold axis complexity in Little Buffalo Basin and Grass Creek anticline can be explained by the interplay of thrust faults in the subsurface and their relative geometry (Banerjee, 2008). However, the northward clockwise rotation of Tensleep anticline's hinge line may be related to another regional structure, the Tensleep Fault. This fault has been documented by Darton (1906), Wilson (1938) and Stone (1962, 2004) and is assumed to be a Precambrian involved fault. It trends roughly east-west and separates the northern Bighorn Mountains from the southern Bighorn Mountains. Throughout its history the fault underwent multiple phases of motion beginning with an early pre-Laramide normal motion (Allison, 1983). Subsequently, the faults 30° angle to Laramide shortening forced it into a compressional regime creating a reverse-sinistral high angle fault. Allison (1983) measured over 8000 structural features including joints, stylolites, plumose structures, faults and slickenside, gypsum veins and gypsum fibers across an approximately 20 km by 3 km swath near the town of Tensleep. From this data she concluded sinistral movement along the fault during the Laramide that effected the axial traces of adjacent Sherard Dome and South Nowood Dome. The author here believes that a similar structural relationship may exist between the clockwise rotations of the Tensleep Anticline's hinge line due to the sinistral motion of the fault. Although situated 10 km to the south of the Tensleep fault, the estimated throw of 120-300 m on the fault could still affect the fold axis. No subsurface control exists on Tensleep anticline as it is not actively producing and seismic sections were not found, thus relating the axial trace curvature to faults is not possible at this time.

North and South Tectonic Domain

Only two anticlines examined in this study fall in this domain: Elk Basin (north) and Thermopolis anticline (south). Each of these structures lies within proximity of larger east-west trending Laramide structure, Nye-Bowler lineament and Owl Creek Mountains, respectively. Relating the east-west orientation of these structures to the Laramide shortening direction suggests a sinistral, oblique-reverse motion across them (Brown, 1993). Whereas Thermopolis anticline clearly reflects the sinistral motion in its hinge line trend, Elk Basin's change in hinge line trace cannot be associated with sinistral movement on the Nye-Bowler lineament.

Elk Basin exhibits a defined counter clockwise rotation in its northern axial trace at a higher degree than other anticlines included in this study. The anticline is located approximately 30 km south of the Nye-Bowler lineament which defines the northern extent of the BHB. Wilson (1936) was the only author to contribute significant research to this structural feature stretching from the Pryor Mountains on the east to the Beartooth Mountain front on the west. Although no single surface fault is exposed, this sinistral transpression zone is defined by a series of NE directed én echelon normal faults and associated domes and half domes (Figure 37). Mapped normal faults across the zone are less than 3 km in length. The structure is thought to be basement involved where weaker overlying Paleozoic strata accommodate subsurface movement through the series of en echelon faults. Although first suggested that Elk Basin anticline, with its proximity to the Nye-Bowler lineament, should reflect the sinistral motion in its fold axis and fractures, it is not supported by data in this study. Elk Basin fracture orientations do not differ from fracture orientations at the east and west side of the basin. Furthermore, the hinge line changes bearings from 334° in the south to approximately 301° at the northern end. This

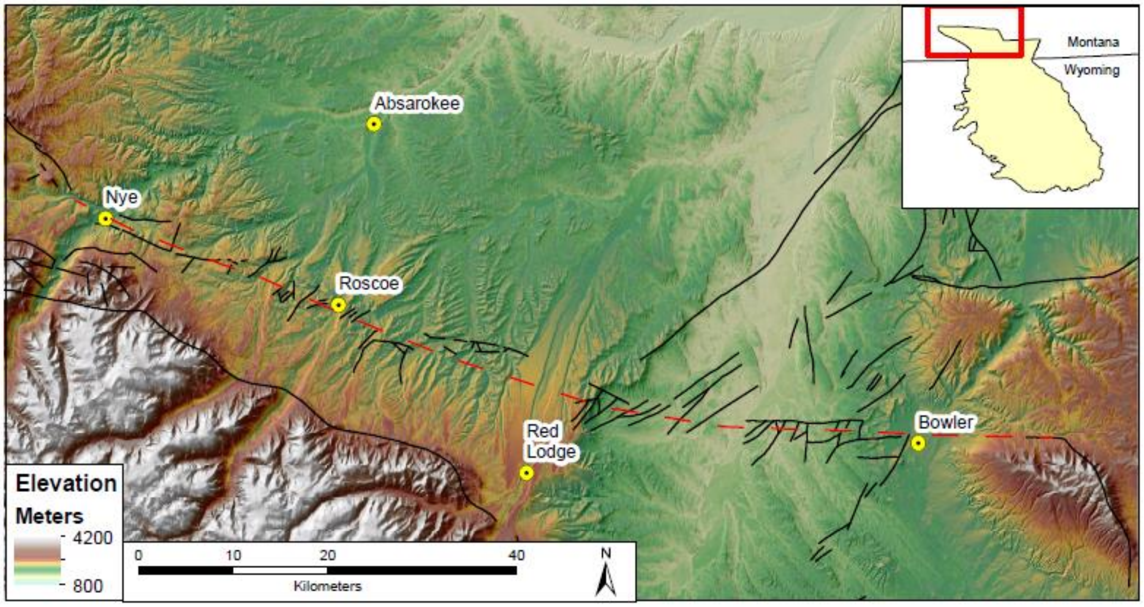

Figure 37: Regional structural setting of the Nye-Bowler lineament. Black lines indicate mapped faults compiled from the Montana Bureau of Mines and Geology. Red dashed line represents approximate location of subsurface basement weakness as described by Wilson (1936).

counter clockwise rotation is the opposite of what would be expected for a sinistral accommodation zone to the north. If the hinge line were to be affected by the Nye-Bowler lineament to the north it should display a clockwise rotation. The noticeable change in hinge line orientation must be due to other local structural features and most likely related to subsurface fault geometry that formed the anticline.

The southern tectonic domain is defined by Thermopolis anticline located approximately 20-25 km from the northern extent of the Owl Creek Mountains. Over the past half century, published literature has argued two main mechanisms for forming these east-west oriented Laramide arches (e.g. Owl Creek Mountains and Casper Mountain) over the typical northwest-southeast arches (e.g. Bighorn, Beartooth Mountains, Wind River and Laramie Range). The debate was previously between east-west arches forming due to a change in the principle shortening orientation throughout multiple deformation phases (Chapin and Cather, 1983; Gries, 1983; Bergh and Snoke, 1992) and a single northeast compression phase (Sales, 1968, Stone, 1969, Brown, 1988, Blackstone, 1990, Erslev, 1993, Paylor and Yin, 1993, Molzer and Erslev, 1995). However, the recent studies in the 1990's provide enough geometric and kinematic data from fault and slickenline orientations (stress inversion calculations) as well as subsurface geometry and relationships of faults to confidently express that only a single northeast compression phase caused the uplift of the Owl Creek Mountains. The Owl Creek Mountains can be divided up into the western and eastern part based on their exposure of Precambrian rocks (Figure 1; Figure 38). Two recent publications have focused on the structures present in west (Paylor and Yin, 1993) and east Owl Creek Mountains (Molzer and Erslev, 1995).

Thermopolis anticline roughly falls just north-northwest of the eastern Owl Creek Mountains and east-northeast of the western Owl Creek Mountains and is influenced by these structures. Whereas the western Owl Creek Mountain's main fault kinematically links two typical northwest striking thrust faults (Black Mountain and Mud Creek thrust) through sinistral slip motion, the eastern Owl Creek Mountains are defined by a zone of sinistral-oblique faults underlain by the dominant sinistral Owl Creek thrust fault (Figure 37). Different from Elk Basin, Thermopolis anticline clearly shows evidence in its hinge line and fracture orientation of the local stress regime created by the Owl Creek Mountains' orientation and associated fault geometry.

Hinge lines in domain 1 trend on average at 154°, Thermopolis anticline trends in a more counterclockwise rotated direction of 114°. This rotation of orientation is

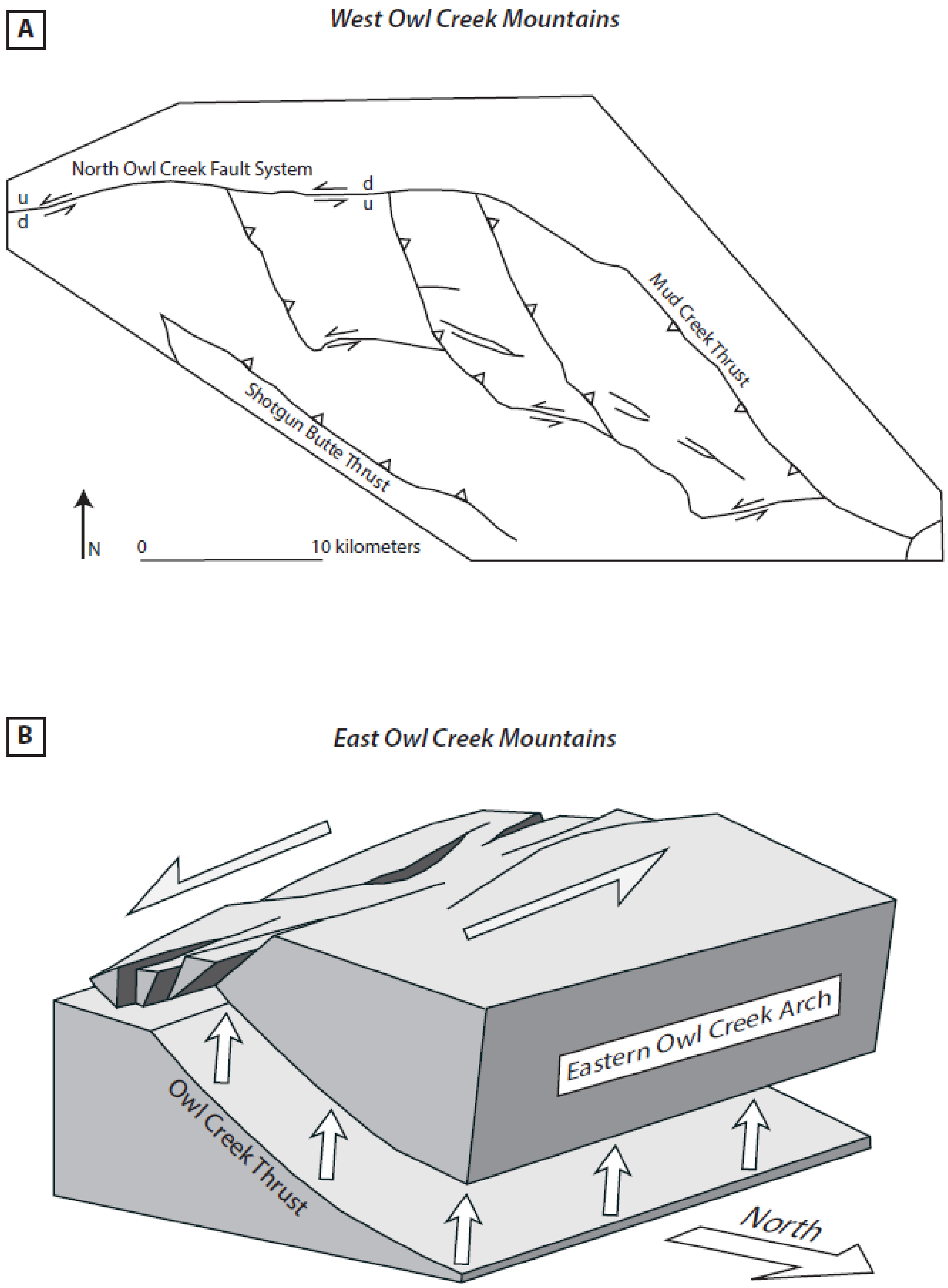

Figure 38: Comparison of (A) West Owl Creek Mountains' and (B) East Owl Creek Mountains' fault geometry. Both regions experienced a sinistral transpressional stress regime during Laramide shortening. The West Owl Creek Mountains contain several thrust faults associated with Laramide shortening direction with motion on adjacent thrust faults accommodated by a series of sinistral strike-slip faults. The East Owl Creek Mountains formed by an underlying main oblique-slip fault which created a series of strike-slip faults in the Paleozoic stratigraphy at the surface. Modified from Yin and Paylor (1993) and Molzer and Erslev (1995).

expected with a sinistral motion to the south and can be genetically linked to the Owl Creek Mountains. The fractures however, do not display orientations different from other anticlines in the basin when related to the trend of the fold axis. The four fracture sets defined are still found throughout the structure. Interestingly though, when comparing the average angle between dip (AC) and strike (BC) fractures (which should be 90°) of Thermopolis anticline to the average of the east and west domain there is a noticeable difference. The average angle for the east and west domain is 86° whereas Thermopolis average lies at 65°. Since dip (AC) fracture are suggested to form earlier than strike (BC) fractures, there may have been a slight sinistral rotation already reducing the interangle between the two fracture sets. However, this hypothesis is purely derived from geometric data and not confirmed by kinematic data or field evidence.

Overall, with the fracture data provided it is more reasonable to link the counterclockwise rotation of Thermopolis anticline to the structures within the Owl Creek Mountains, than it is to relate Elk Basin anticline in the north to the Nye-Bowler lineament. The author of this study believes that further detailed fracture analysis within the domes and half-domes of the Nye-Bowler lineament may reveal direct evidence for the sinistral nature of the structure.

Implications for Hydrocarbon Production

The results explained in the discussion above allow for general suggestions to be made about the occurrence and extraction of hydrocarbons in the BHB. When comparing domain 1 and domain 2 with relative past hydrocarbon production it is clear that domain 1 has a higher potential for overall hydrocarbon extraction. The western shoulder of the basin has been a prolific source for hydrocarbons (Finn et al. 2010). This may relate to the asymmetry of the BHB and the relative depth source rocks on the western versus the eastern shoulder. Elk Basin and Oregon Basin have produced the most hydrocarbons since their discovery with lesser quantities extracted from Little Buffalo Basin and Grass Creek anticline. Horse Center anticline does not have any hydrocarbon production which may relate to the larger structural relief and older units exposed at the surface. On the east shoulder of the basin, from the anticlines included in this study, only Manderson anticline produces hydrocarbon. Both Manderson and Tensleep anticlines have not been drilled for hydrocarbon extraction.

Different from domain 1, domain 2 does not produce any hydrocarbons. Thermopolis anticline, like Horse Center anticline, exposes much older units at the surface when compared to producing anticlines in the BHB. Another cause of a lack of production may be related to its relationship to the sinistral accommodation zone to the south. Since Thermopolis anticline is rotated counterclockwise, one might suggest a higher proportion of mode III (shear) or hybrid fractures compared to mode I (joints). Whereas other anticlines within the BHB generally display mode I (joints), open fractures, shear fractures generally have lower permeability leading to less hydrocarbon migration. This may relate to the absence of hydrocarbon production from domain 2.

CONCLUSION

The purpose this study was to the relate fold hinge line and fracture orientations within nine anticlines across the BHB to larger Laramide structures around the basin (e.g. Beartooth Mountains, Bighorn Mountains, Owl Creek Mountains and Nye-Bowler Lineament) to suggest compartmentalized tectonic domains displaying differences in local stress regime. Results indicate a good correlation between hinge line trend and fracture orientations within individual anticlines across the entire basin. The average trend of hinge line of anticlines on the east and west side of the basin (tectonic domain 1) is 154° which agrees with the Laramide shortening direction of 060° N as defined by Neely and Erslev (2009) (Figure 39). Even the northern most anticline, Elk Basin, has a northern fold axis of 155° indicating a lesser influence of the sinistral movement of the Nye-Bowler lineament to the north. However, its southern fold axis trends at 2° which may suggest influence of sinistral rotation. The fracture sets identified in tectonic domain 1 align with previous published orientations of Rattlesnake Mountain and Sheep Mountain anticline (Fiore, 2006; Bellahasen et al., 2006, Beaudoin et al., 2011, Beaudoin et al., 2012). This correlation suggests that both anticlines on the east and west side of the BHB formed from the same local stress regime and there is no variance in shortening along the adjacent uplifts.

Only Thermopolis anticline shows a distinctly different fold orientation that is related to the sinistral movement on major faults of the Owl Creek Mountains to the south and can thus be classified in its own tectonic domain. Evidence for this lies both within the 36° counterclockwise rotation when compared to the average of fold axis

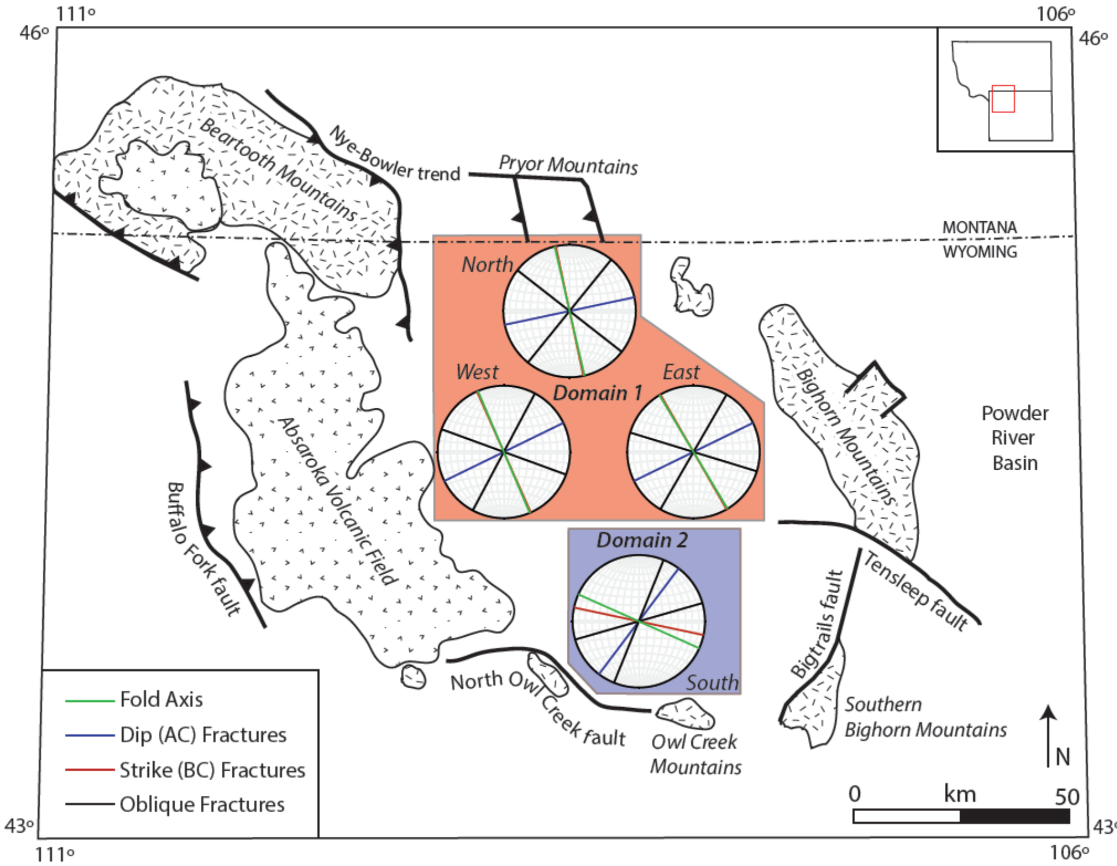

Figure 39: Bighorn Basin tectonic domains as identified from outcrop fracture analysis in this study. Stereonets show average fold axis and fracture measurements for each side of the basin. Note dip (AC) fractures in domain 1 almost perfectly align with the fold axis. Reference map modified from Blackstone (1986).

within the rest of within the rest of the basin as well as the rotation of associated fracture sets. The clear sense of sinistral movement on Thermopolis anticline versus no shear movement of Elk Basin anticline in the north may be due to relative displacement on the adjacent sinistral accommodation zones (Owl Creek Mountains versus Nye-Bowler lineament. Whereas the eastern Owl Creek Mountains have suggested vertical separation of over 7900 m (Blackstone, 1990) and sinistral separation of 2000 m (Hamil, 1971, Caldwell, 1977), the lack of research and seismic support data on movement on the Nye-Bowler lineament does not allow for a direct comparison.

REFRENCES CITED

RFERENCES CITED

Allison, M. L., 1983, Deformation styles along the Tensleep fault, Bighorn Basin, Wyoming, Wyoming Geological Association Guidebook, 34th Annual Field Conference.

Armstrong, R. L., 1968, Sevier orogenic belt in Nevada and Utah, Geological Society of America Bulletin, v. 79, p. 429-458.

Bai, T., and Pollard, D. D., 2000, Fracture spacing in layered rocks: a new explanation based on the stress transition: Journal of Structural Geology, v. 22, p. 43-57.

Banerjee, S., 2008, Structural analysis of basement-involved anticlines along the western margin of the Bighorn Basin, Wyoming, Doctoral Dissertation, University of Oklahoma.

Beaudoin, N., Bellahsen, N., Lacombe, O., and Emmanuel, L., 2011, fracture-controlled paleohydrogeology in a basement-cored, fault-related fold: Sheep Mountain Anticline, Wyoming, United States, Geochemisty Geophysics Geosystems, v. 12, n. 6, p. 1-15.

Beaudoin, N., Lepretre, R., Bellahsen, N., Lacombe, O., Amrouch, K., Callot, J.P., Emmanuel, L., and Daniel, J.M., 2012, Structural and microstructural evolution of the Rattlesnake Mountain Anticline (Wyoming, USA): New insights into the Sevier and Laramide orogenic stress build-up in the Bighorn Basin, Tectonophysics, v. 576-577, p. 20-45.

Bellahsen, N., Fiore, P., and Pollard, D. D., 2006, The role of fractures in the structural interpretation of the Sheep Mountain Anticline, Wyoming, Journal of Structural Geology, v. 28, p. 850-867.

Berg, R. R., 1962, Mountain flank thrusting in Rocky Mountain foreland, Wyoming and Colorado: American Association of Petroleum Geologists Bulletin, v. 46, p. 2019-2032.

Bergh, S. G., and A. W. Snoke, 1992, Polyphase Laramide deformation in the Shirley Mountains, south central Wyoming foreland: The Mountain Geologist, v. 29., p. 85-100.

Bird, P., 1998, Kinematic history of the Laramide orogeny in latitudes 35-49N, western United States, Tectonics, v.17, n. 5, p. 780-801.

Bird, P., 2002, Stress direction history of the western United States and Mexico since 85 Ma, Tectonics, v. 21, no. 3, p. 1-12.

Blackstone, D. L., 1940, Structure of the Pryor Mountains, Montana, The Journal of Geology, v. 48, n. 6, p. 590-618.

Blackstone, D. L., 1986, Foreland compressional tectonics: southern Bighorn Basin and adjacent areas, Wyoming, Report of Investigations No. 34, Geological Survey of Wyoming, p. 1-32.

Blackstone, D. L., 1990, Rocky Mountain foreland structure exemplified by the Owl Creek Mountains, Bridger Range and Casper arch, central Wyoming, *in* R. W. Specht, ed., Wyoming sedimentation and tectonics: Casper, Wyoming, Wyoming Geological Association 41st Field Conference Guidebook, p. 151-166.

Brown, W. G., 1988, Deformation style in Laramide uplifts in the Wyoming foreland, *in* C. J. Schmidt and W. J. Perry, Jr., eds., Interaction of the Rocky Mountain foreland and the Cordilleran thrust belt: Geological Society of America Memoir 171, p. 1-25.

Brown, W. G., 1993, Structural style of Laramide basement-cored uplifts and associated folds, Geology of Wyoming, Geological Survey of Wyoming, v. 5, p. 312-371.

Caldwell, J. P., 1977, Geology of the Red Canyon-Buffalo basin area, Owl Creek Mountains, Wyoming: Master's thesis, University of Iowa, Iowa City, Iowa, 99 p.

Cardozo, N., and Allmendinger, R. W., 2013, Spherical projections with OSX Stereonet, Computers and Geoscience, v. 51, p. 193-205.

Chamberlain, R.T., 1945, Basement control in Rocky Mountain deformation, American Journal of Science, no. 243, p. 98-116.

Chapin, C E., and S. M. Cather, 1983, Eocene tectonics and sedimentation in the Colorado Plateau; Rocky Mountain area, *in* J. D. Lowell ed., Rocky Mountain foreland basins and uplifts: Rocky Mountain Association of Geologists, p. 33-56.

Cook, M. L., 1997, Predicting fracture localization in folded strata from mechanical stratigraphy and fold shape: Case study of East Kaibab Monocline, Utah

Cooper, S. P., Goodwin, L. B., Lorenz, J. C., Teufel, L. W., and Hart, B. S., 1998, Geometric and genetic relationships between fractures, normal faults, and a doubly-plunging anticline; Teapot Dome, Wyoming, Geological Society of America, Abstracts with Programs 30, p. 62.

Cooper, S. P., Lorenz, J. C., and Goodwin, L. B., 2001, Lithologic and structural controls on natural fracture characteristics Teapot Dome, Wyoming, United States Department of Energy, Washington, DC, 73 p.

Crowley, P. D., Reiners, P. W., Reuter, J. M., and Kaye, G. D., Laramide exhumation of the Bighorn Mountains, Wyoming: an apatite (U-Th)/He thermochronology study, Geology, v. 30, n. 1, p. 27-30.

Cerveny, P. F., 1990, Fission-track thermochronology of the Wind River range and other basement cored uplifts in the Rocky Mountain foreland: University of Wyoming, 180 p.

Darton, N. H., 1906, Geology of the Bighorn Mountains, United States Geological Survey, Professional Paper 51.

DeCelles, P. G., and Mitra, G., 1995, History of the Sevier orogenic wedge in terms of critical taper models, northeast Utah and southwest Wyoming, Geological Society of America Bulletin, v. 107, p. 454-462.

Dickinson, W. R., Klute, M. A., Hayes, M. J., Janecke, S. U., Lundin, E. R., McKittrick, M. A., and Olivares, M. D., 1988, Paleogeographic and paleotectonic setting of Laramide sedimentary basins in the central Rocky Mountain region, Geological Society of America Bulletin, v. 100, p. 1023-1039.

Durdella, M. J., 2001, Mechanical Modeling of fault-related Folds: West Flank of the Bighorn Basin, Wyoming. Master’s Thesis, Purdue University.

Eicher, D. L., 1962, Biostratigraphy of the Thermopolis, Muddy, and Shell Creek Formation, *in* Enyert, R. L., and Curry, W. H., eds., Symposium on Early Cretaceous rocks of Wyoming and adjacent areas: Wyoming Geological Association 17th Annual Field Conference, p. 72-93.

Englelder, T., Gross, M. R., Pinkerton, P., 1997. An analysis of join development in thick sandstone beds of the Elk Basin Anticline, Montana-Wyoming, Rocky Mountain Association of Geologists 1997 Guidebook, Denver, Colorado, p. 1-18.

Erslev, E. A., 1991, Trishear fault-propagation folding, Geology, v. 19, p. 617-620.

Erslev, E. A., 1993, Thrusts, back-thrusts, and detachment of the Rocky Mountain foreland arches, *in* Schmidt, C. J., Chase, R. B., and Erslev, E. A., eds., Laramide Basement Deformation in the Rocky Mountain Foreland of the Western United States: Boulder, Colorado, Geological Society of American Special Paper 280.

Erslev, E. A. and Koenig, N. V., 2009, Three-dimensional kinematics of Laramide, basement-involved Rocky Mountain deformation, USA: Insights from minor faults and GIS-enhanced structure maps, Geological Society of America Memoirs, v. 204, p.125-150.

Garfield, T. R., Hurley, N. F., and Budd, D. A., 1992, Little Sand Draw File, Bighorn Basin, Wyoming: a hybrid dual-porosity and single-porosity reservoir in the Phosphoria Formation, American Association of Petroluem Geologists Bulletin 76, 371-391.

Gries, R., 1983, North-south compression of the Rocky Mountain foreland structures, *in* J. D. Lowell, ed., Rocky Mountain foreland basins and uplifts: Rocky Mountain Association of Geologists, p. 9-32.

Finn, T. M., Kirschbaum, M. A., Roberts, S. B., Condon, S. M., Roberts, L. N. R., and Johnson, R. C., 2010, Cretaceous-tertiary composite total petroleum system (503402), bighorn basin, Wyoming and Montana. U.S.Geological Survey Digital Data Series, p. 159.

Fiore, P. E., 2006, 3D characterization and mechanics of brittle deformation in thrust fault related folds, Doctoral Dissertation, Stanford University

Fjaer, E., Holt, R. M., Horsrud, P., Raaen, A.M., and Risnes, R., 1992, Petroleum related rock mechanics: New York Elsevier Science Publishing Company Inc., 388 p.

Foose, R. M., Wise, D. U., and Garbarini, G. S., 1961, Structural geology of the Beartooth mountains, Montana and Wyoming, Geological Society of America Bulletin, v.72, p. 1143-1172.

Hafner, W., 1951, Stress distribution and faulting, Geological Society of America Bulletin, v. 62, p. 373-398.

Hamil, M. M., 1971, Metamorphic and structural environment of Copper Mountain, Wyoming, Ph.D. dissertation, University of Missouri, Columbia, Missouri, 77 p.

Harris, R., and Boberg, W. W., 1983, Uranium and thorium in the Bighorn Basin, 34th annual field conference, Wyoming Geological Association, v. 34, p. 171-177.

Haun, J.D., and Barlow, J.A., 1962, Lower Cretaceous stratigraphy of Wyoming, *in* Enyert, R.L., and Curry, W.H., eds., Symposium on Early Cretaceous rocks of Wyoming and adjacent areas: Wyoming Geological Association 17th Annual Field Conference Guidebook, p. 15–22.

Hayes, M., Hanks, C. L., 2008, Evolving mechanical stratigraphy during detachment folding, Journal of Structural Geology, v. 30, n. 5, p. 548-564.

Hennings, P. H., Olson, J. E., and Thompson, L. B., 2000, Combining outcrop data and three-dimensional structural models to characterize fractures reservoirs; an example from Wyoming, American Association of Petroleum Geologists Bulletin 84, p. 830-849.

Hobbs, D. W., 1967, The formation of tension joints in sedimentary rocks: an explanation: Geological Magazine, v. 104, n. 6, p. 550-556.

Hunt, T. S., 1861, Bitumens and mineral oils: Montreal Gazette, March 1.

Keefer, W. R., and Love, J. D., 1963, Laramide vertical movements in central Wyoming, Contributions to Geology, v. 2, p. 47-54.

Keefer, W.R., Finn, T.M., Johnson, R.C., and Keighin, C.W., 1998, Regional stratigraphy and correlation of Cretaceous and Paleocene rocks, Bighorn Basin, Wyoming and Montana, *in* Keefer, W.R., and Goolsby, J.E., eds., Cretaceous and Lower Tertiary rocks of the Bighorn Basin, Wyoming and Montana: Wyoming Geological Association 49th Guidebook, p. 1–30.

Kirkup, L., 2002, Data Analysis with Excel, Cambridge University Press, 446 p.

Ladeira, F. L., and Price, N. J., 1981, Relationship between fracture spacing and bed thickness: Journal of Structural Geology, v. 3, p. 179-183.

Lageson, D.R., Larsen, M.C., Lynn, H.B., and Treadway, W.A., 2012, Applications of Google Earth Pro to fracture and fault studies of Laramide anticlines in the Rocky Mountain foreland, *in* Whitmeyer, S.J., Bailey, J.E., De Paor, D.G., and Ornduff, T., eds., Google Earth and Virtual Visualizations in Geoscience Education and Research: Geological Society of America Special Paper 492, p. 1–12.

Lorence, J. C., 1997, Heartburn in predicting natural fractures: The effects of differential fracture susceptibility in heterogeneous lithologies, *in* Hoak, T. E., Klawitter, A. L. and Blomquist, P. K., eds., Fractures reservoirs: Characterization and modeling: Rocky Mountain Association of Geologists Guidebook, p.57-66.

Lowell, J. D., 1983, Foreland Deformation, *in* J. D. Lowell, ed., Rocky Mountain foreland basins and uplifts: Rocky Mountain Association of Geologists, p. 1-9.

Neely, T. G., and Erslev, E. A., 2009, The interplay of fold mechanisms and basement weaknesses at the transition between Laramide basement-involved arches, north-central Wyoming, USA, Journal of Structural Geology, no. 31, p. 1012-1027.

Marshak, S., and Mitra, G., 1988, Basic Methods of Structural Geology, Prentice Hall, New Jersey, p. 105-124.

Mills, N.K., 1956, Subsurface stratigraphy of the pre-Niobrara Formations in the Bighorn Basin, Wyoming, Wyoming Stratigraphy, Part I, Subsurface stratigraphy of the pre-Niobrara Formations in Wyoming: Wyoming Geological Association, p. 9–22.

Mitra, S., and Mount, V. S., 1998, Foreland basement-involved structures, American Association of Petroleum Geologists Bulletin, v. 82, p. 70-109.

Molzer P. C., and Erslev, E. A., 1995, Oblique convergence during northeast-southwest Laramide compression along the east-east Owl Creek and Casper Mountain Arches, Central Wyoming, American Association of Petroleum Geologists Bulletin, v. 79, n. 9, p. 1377-1394.

Nuccio, V. F., and Finn, T. M., 1998, Thermal maturity and petroleum generation history of cretaceous and tertiary source rocks, bighorn basin, Wyoming and Montana. Wyoming Geological Association, v. 49, p. 211-232.

Omar, G. I., Lutz, T. M., and Giegengack, R., 1994, Apatite fission-track evidence for Laramide and post-Laramide uplift and anomalous thermal regime at the Beartooth overthrust, Montana-Wyoming: Geological Society of America Bulletin, v. 106, p. 74-85.

Pavlis, G. L., Sigloch, K., Burdick, S., Fouch, M. J., and Vernon, F. L., 2012, Unraveling the geometry of the Farallon plate: Synthesis of three-dimensional imaging results from USArray, Tectonophysics, v. 532-535, p. 82-102.

Paylor, E. D., and Yin, A., 1993, Left-slip evolution of the North Owl Creek fault system, Wyoming, during Laramide shortening, *in* Schmidt, C. J., Chase, R. B., and Erslev, E. A., eds., Laramide Basement Deformation in the Rocky Mountain Foreland of the Western United States: Boulder, Colorado, Geological Society of American Special Paper 280.

Peyton, S. L., 2009, Low-temperature thermochronology of the laramide ranges and eastward translation of shortening in the sevier belt. Wyoming, Utah, and Montana, Doctoral Dissertation, University of Arizona.

Price, N. J., 1966, Fault and join development: Oxford, Pergamon Press, 176 p.

Price, N. J., and Cosgrove, J. W., 1990, Analysis of Geologic Structures. Cambridge University Press.

Prucha, J. J., Graham, J. A., and Nickelsen, R. P., 1965, Basement-controlled deformation in Wyoming province of Rocky Mountain foreland: American Association of Petroleum Geologists Bulletin, v.49, p. 966-992.

Raines, G. L., and Johnson, B. R., 1995, Digital representation of the Montana state geologic map; contribution to the Interior Columbia River basin ecosystem management project: U.S. Geological Survey Open-File Report 95-691, 20 p.

Ramsay, J. G., and Huber, R. M., 1987, The techniques of modern structural geology, Volume 2: folds and fractures, Elsevier Science, 697 p.

Sales, J. K., 1968. Crustal mechanics of Cordilleran foreland deformation; a regional and scale-model approach, The American Association of Petroleum Geologists Bulletin, v. 52, p. 2016-2044.

Savage, H. M., Shackleton, J. R., Cooke, M. L., and Riedel, J. J., 2010, Insights into fold growth using fold-related joint patterns and mechanical stratigraphy, Journal of Structural Geology, v. 32, n. 10, p. 1466-1475.

Silliphant, L. J., Engelder, T., and Gross, M. R., 2002, The state of stress in the limb of Split Mountain anticline, Utah: constraints placed by transected joints, Journal of Structural Geology 24, p. 155-172.

Stearns, D., 1975, Laramide basement deformation in the Bighorn Basin, Annual field conference, Wyoming Geological Survey, vol. 27, p. 149-158.

Stone, D. S., 1962, Wrench faulting in Rocky Mountain tectonics, Mountain Geologist, v. 6, p. 67-79.

Stone, D., 2004, Structures of the Rocky Mountain foreland, Mountain Geologist, v. 41, n. 3, p. 140-142.

Thom, W., 1947, Structural features of the Bighorn Basin rim, Field conference in the Bighorn Basin, Wyoming Geological Association, v. 12, p. 173-177.

Thomas, L., Sedimentation and structural development of the Big Horn Basin, American Association of Petroleum Geologists Bulletin, v. 49, p. 1867-1877.

Usui, T., Nakamura, E., Kobayashi, K.M., Maruyama, S., Helmstaedt, H., 2003. Fate of the subducted Farallon plate inferred from eclogite xenoliths in the Colorado Plateau. Geology, v. 31, p. 589–592.

van der Pluijm, B. A., and Marshak, S., 2004, Earth structure: An introduction to structural geology and tectonics (2nd edition): New York, W.W. Norton and Company, 656 p.

Weil, A. B., and Yonkee, W. A., 2012, Layer-parallel shortening across the Sevier fold-thrust belt and Laramide foreland of Wyoming: spatial and temporal evolution of a complex geodynamic system, Earth and Planetary Science Letters, v. 357, p. 405-420.

Weinberg, D. M., 1979, Experimental folding of rocks under confining pressure, Tectonophysics, v. 54, p. 1-24.

White, I.C., 1885, The geology of natural gas: Science (June and July).

Wicks, J. L., Dean, S. L., and Kulander, B. R., 2000, regional tectonics and fracture patters in the Fall River Formation (Lower Cretaceous) around the Black Hills foreland uplifts, western South Dakota and northeastern Wyoming, *in* Cosgrove, J. W., Ameen, M. S. (Eds.), Forced Folds and Fractures, Geological Society of London Special Publication 169, p. 145-165.

Wilson, C. W., 1936, Geology of the Nye-Bowler lineament, Stillwater and Carbon Counties, Montana, American Association of Petroleum Geologists Bulletin, v. 20, n. 9, p. 1161-1188.

Yin, A, and Ingersoll, R. V., 1997, A model for the evolution of Laramide axial basins in the Southern Rocky Mountains, U.S.A., International Geology Review, v. 39, p. 1113-1123.

Zietz, I., Hearn, B. C., Higgins, M. W., Robinson, G. D., and Swanson, D. A., 1971, Geological Society of America Bulletin, v. 82, p. 3347-3372.

APPENDICES

APPENDIX A

STRATIGRAPHY LEGEND FOR GEOLOGIC MAPS OF EACH ANTICLINE AND CORRELATION OF MONTANA AND WYOMING FORMATIONS

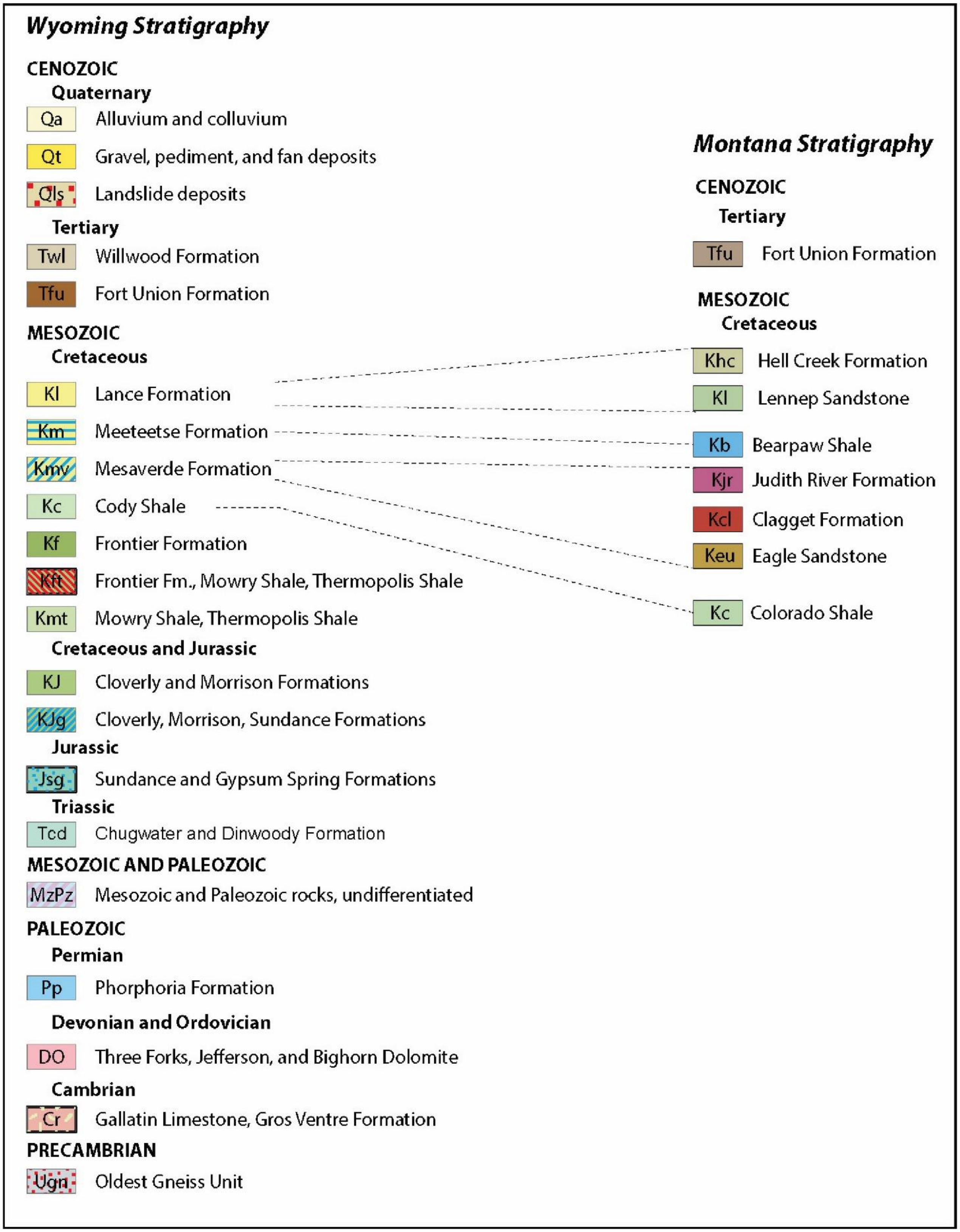
Wyoming Stratigraphy
CENOZOIC
Quaternary
Qa Alluvium and colluvium
Qt Gravel, pediment, and fan deposits
Qls Landslide deposits
Tertiary
Twl Willwood Formation
Tfu Fort Union Formation
MESOZOIC
Cretaceous
Kl Lance Formation
Km Meeteetse Formation
Kmv Mesaverde Formation
Kc Cody Shale
Kf Frontier Formation
Kft Frontier Fm., Mowry Shale, Thermopolis Shale
Kmt Mowry Shale, Thermopolis Shale
Cretaceous and Jurassic
KJ Cloverly and Morrison Formations
KJg Cloverly, Morrison, Sundance Formations
Jurassic
Jsg Sundance and Gypsum Spring Formations
Triassic
Tcd Chugwater and Dinwoody Formation
MESOZOIC AND PALEOZOIC
MzPz Mesozoic and Paleozoic rocks, undifferentiated
PALEOZOIC
Permian
Pp Phorphoria Formation
Devonian and Ordovician
DO Three Forks, Jefferson, and Bighorn Dolomite
Cambrian
Cr Gallatin Limestone, Gros Ventre Formation
PRECAMBRIAN
Ugn Oldest Gneiss Unit
Montana Stratigraphy
CENOZOIC
Tertiary
Tfu Fort Union Formation
MESOZOIC
Cretaceous
Khc Hell Creek Formation
Kl Lennep Sandstone
Kb Bearpaw Shale
Kjr Judith River Formation
Kcl Clagget Formation
Keu Eagle Sandstone
Kc Colorado Shale

APPENDIX B

LIST OF FRACTURE MEASUREMENTS

Outcrop/ Stereonet #	Anticline	Bedding Dip Direction	Bedding Dip	Fracture Dip Direction	Fracture Dip
1	Horse Center Anticline	293	54	90	38
1	Horse Center Anticline			84	33
1	Horse Center Anticline			91	35
1	Horse Center Anticline			180	83
1	Horse Center Anticline			198	90
1	Horse Center Anticline			177	76
1	Horse Center Anticline			172	78
1	Horse Center Anticline			176	72
1	Horse Center Anticline			188	85
2	Horse Center Anticline	198	4	186	83
2	Horse Center Anticline			110	82
2	Horse Center Anticline			115	87
2	Horse Center Anticline			116	84
2	Horse Center Anticline			122	85
2	Horse Center Anticline			175	85
2	Horse Center Anticline			65	65
2	Horse Center Anticline			41	70
3	Horse Center Anticline	256	38	132	76
3	Horse Center Anticline			312	87
3	Horse Center Anticline			302	90
3	Horse Center Anticline			307	62
3	Horse Center Anticline			152	18
3	Horse Center Anticline			143	39
3	Horse Center Anticline			146	31
3	Horse Center Anticline			180	43
4	Horse Center Anticline	275	40	8	77
4	Horse Center Anticline			345	78
4	Horse Center Anticline			2	80
4	Horse Center Anticline			0	88
4	Horse Center Anticline			3	90
4	Horse Center Anticline			350	82
4	Horse Center Anticline			95	48
4	Horse Center Anticline			86	48
4	Horse Center Anticline			86	41
4	Horse Center Anticline			90	31
4	Horse Center Anticline			103	40
4	Horse Center Anticline			108	47
4	Horse Center Anticline			105	52
5	Horse Center Anticline	36	24	280	79
5	Horse Center Anticline			265	74
5	Horse Center Anticline			274	80
5	Horse Center Anticline			264	87
5	Horse Center Anticline			182	64
5	Horse Center Anticline			158	70
5	Horse Center Anticline			172	65
5	Horse Center Anticline			184	69
5	Horse Center Anticline			238	64
5	Horse Center Anticline			240	57
5	Horse Center Anticline			231	63
6	Horse Center Anticline	319	6	345	90
6	Horse Center Anticline			177	83
6	Horse Center Anticline			176	74

Outcrop/ Stereonet #	Anticline	Bedding Dip Direction	Bedding Dip	Fracture Dip Direction	Fracture Dip
4	Horse Center Anticline			95	48
4	Horse Center Anticline			86	48
4	Horse Center Anticline			86	41
4	Horse Center Anticline			90	31
4	Horse Center Anticline			103	40
4	Horse Center Anticline			108	47
4	Horse Center Anticline			105	52
5	Horse Center Anticline	36	24	280	79
5	Horse Center Anticline			265	74
5	Horse Center Anticline			274	80
5	Horse Center Anticline			264	87
5	Horse Center Anticline			182	64
5	Horse Center Anticline			158	70
5	Horse Center Anticline			172	65
5	Horse Center Anticline			184	69
5	Horse Center Anticline			238	64
5	Horse Center Anticline			240	57
5	Horse Center Anticline			231	63
6	Horse Center Anticline	319	6	345	90
6	Horse Center Anticline			177	83
6	Horse Center Anticline			176	74
6	Horse Center Anticline			181	84
6	Horse Center Anticline			1	89
6	Horse Center Anticline			89	90
6	Horse Center Anticline			89	82
6	Horse Center Anticline			88	86
6	Horse Center Anticline			72	84
6	Horse Center Anticline			84	80
6	Horse Center Anticline			76	82
7	Horse Center Anticline	246	45	159	72
7	Horse Center Anticline			151	88
7	Horse Center Anticline			151	87
7	Horse Center Anticline			351	84
7	Horse Center Anticline			149	90
7	Horse Center Anticline			131	61
7	Horse Center Anticline			112	58
7	Horse Center Anticline			139	76
7	Horse Center Anticline			153	68
8	Horse Center Anticline	222	24	139	88
8	Horse Center Anticline			143	80
8	Horse Center Anticline			141	82
8	Horse Center Anticline			144	89
8	Horse Center Anticline			145	89
8	Horse Center Anticline			81	86
8	Horse Center Anticline			81	64
8	Horse Center Anticline			90	64
8	Horse Center Anticline			91	67
9	Horse Center Anticline	63	14	299	81
9	Horse Center Anticline			300	81
9	Horse Center Anticline			116	77
9	Horse Center Anticline			309	89
9	Horse Center Anticline			300	86
9	Horse Center Anticline			119	82

Outcrop/ Stereonet #	Anticline	Bedding Dip Direction	Bedding Dip	Fracture Dip Direction	Fracture Dip
9	Horse Center Anticline			222	83
9	Horse Center Anticline			171	69
9	Horse Center Anticline			204	78
9	Horse Center Anticline			213	86
9	Horse Center Anticline			211	82
10	Horse Center Anticline	45	19	287	64
10	Horse Center Anticline			103	80
10	Horse Center Anticline			110	81
10	Horse Center Anticline			111	88
10	Horse Center Anticline			108	74
10	Horse Center Anticline			298	90
10	Horse Center Anticline			115	80
10	Horse Center Anticline			209	79
10	Horse Center Anticline			206	86
10	Horse Center Anticline			212	85
10	Horse Center Anticline			200	85
11	Oregon Basin	80	19	248	72
11	Oregon Basin			250	71
11	Oregon Basin			247	78
11	Oregon Basin			230	74
12	Oregon Basin	44	17	175	82
12	Oregon Basin			169	72
12	Oregon Basin			180	78
12	Oregon Basin			125	85
12	Oregon Basin			121	83
12	Oregon Basin			128	87
12	Oregon Basin			142	80
12	Oregon Basin			222	80
12	Oregon Basin			233	86
13	Oregon Basin	85	16	175	77
13	Oregon Basin			175	89
13	Oregon Basin			173	88
13	Oregon Basin			344	87
13	Oregon Basin			174	90
13	Oregon Basin			284	69
13	Oregon Basin			291	78
13	Oregon Basin			325	77
14	Oregon Basin	223	37	290	40
14	Oregon Basin			325	53
14	Oregon Basin			304	44
14	Oregon Basin			311	48
14	Oregon Basin			315	81
14	Oregon Basin			65	68
14	Oregon Basin			62	76
14	Oregon Basin			68	67
14	Oregon Basin			94	75
15	Oregon Basin	210	30	115	82
15	Oregon Basin			115	85
15	Oregon Basin			105	90
15	Oregon Basin			104	89
15	Oregon Basin			101	85
15	Oregon Basin			108	80
15	Oregon Basin			57	47

Outcrop/ Stereonet #	Anticline	Bedding Dip Direction	Bedding Dip	Fracture Dip Direction	Fracture Dip
15	Oregon Basin			71	47
15	Oregon Basin			55	45
15	Oregon Basin			64	64
16	Oregon Basin	182	9	117	85
16	Oregon Basin			142	85
16	Oregon Basin			173	90
16	Oregon Basin			177	76
16	Oregon Basin			145	89
16	Oregon Basin			351	82
16	Oregon Basin			152	75
16	Oregon Basin			144	83
17	Oregon Basin	108	33	236	55
17	Oregon Basin			347	79
17	Oregon Basin			240	66
17	Oregon Basin			251	60
17	Oregon Basin			248	65
17	Oregon Basin			243	58
17	Oregon Basin			15	47
17	Oregon Basin			45	84
17	Oregon Basin			3	71
18	Oregon Basin	95	31	291	58
18	Oregon Basin			290	38
18	Oregon Basin			290	56
18	Oregon Basin			295	56
18	Oregon Basin			300	54
18	Oregon Basin			287	56
18	Oregon Basin			29	87
18	Oregon Basin			20	70
18	Oregon Basin			5	84
18	Oregon Basin			171	85
18	Oregon Basin			186	80
18	Oregon Basin			271	45
19	Oregon Basin	217	42	305	84
19	Oregon Basin			314	82
19	Oregon Basin			312	88
19	Oregon Basin			303	89
19	Oregon Basin			303	87
19	Oregon Basin			238	50
19	Oregon Basin			231	61
19	Oregon Basin			58	54
19	Oregon Basin			32	26
19	Oregon Basin			65	42
19	Oregon Basin			55	46
20	Little Buffalo Basin	65	30	205	61
20	Little Buffalo Basin			206	48
20	Little Buffalo Basin			225	65
20	Little Buffalo Basin			219	45
20	Little Buffalo Basin			200	55
20	Little Buffalo Basin			1	80
20	Little Buffalo Basin			315	59
20	Little Buffalo Basin			298	45
20	Little Buffalo Basin			209	70
20	Little Buffalo Basin			297	39

Outcrop/ Stereonet #	Anticline	Bedding Dip Direction	Bedding Dip	Fracture Dip Direction	Fracture Dip
20	Little Buffalo Basin			159	87
20	Little Buffalo Basin			290	45
20	Little Buffalo Basin			155	80
20	Little Buffalo Basin			216	54
20	Little Buffalo Basin			223	56
20	Little Buffalo Basin			233	76
21	Little Buffalo Basin	34	24	181	68
21	Little Buffalo Basin			189	74
21	Little Buffalo Basin			186	75
21	Little Buffalo Basin			339	80
21	Little Buffalo Basin			190	89
21	Little Buffalo Basin			335	70
21	Little Buffalo Basin			333	87
21	Little Buffalo Basin			2	89
21	Little Buffalo Basin			193	62
21	Little Buffalo Basin			175	90
21	Little Buffalo Basin			192	52
21	Little Buffalo Basin			109	90
21	Little Buffalo Basin			100	85
21	Little Buffalo Basin			301	51
21	Little Buffalo Basin			187	70
21	Little Buffalo Basin			96	85
21	Little Buffalo Basin			105	90
22	Little Buffalo Basin	87	13	301	85
22	Little Buffalo Basin			124	85
22	Little Buffalo Basin			302	85
22	Little Buffalo Basin			303	86
22	Little Buffalo Basin			303	90
22	Little Buffalo Basin			316	89
22	Little Buffalo Basin			16	87
22	Little Buffalo Basin			9	78
22	Little Buffalo Basin			359	79
22	Little Buffalo Basin			185	83
22	Little Buffalo Basin			174	79
22	Little Buffalo Basin			176	86
22	Little Buffalo Basin			315	81
22	Little Buffalo Basin			316	87
22	Little Buffalo Basin			301	85
23	Little Buffalo Basin	220	26	101	71
23	Little Buffalo Basin			104	83
23	Little Buffalo Basin			95	84
23	Little Buffalo Basin			102	85
23	Little Buffalo Basin			110	70
23	Little Buffalo Basin			111	83
23	Little Buffalo Basin			98	85
23	Little Buffalo Basin			138	90
23	Little Buffalo Basin			130	84
23	Little Buffalo Basin			129	84
23	Little Buffalo Basin			110	80
23	Little Buffalo Basin			114	79
23	Little Buffalo Basin			23	65
23	Little Buffalo Basin			5	75
23	Little Buffalo Basin			2	82

Outcrop/ Stereonet #	Anticline	Bedding Dip Direction	Bedding Dip	Fracture Dip Direction	Fracture Dip
23	Little Buffalo Basin			25	57
23	Little Buffalo Basin			25	54
23	Little Buffalo Basin			4	71
23	Little Buffalo Basin			15	68
23	Little Buffalo Basin			20	74
24	Little Buffalo Basin	242	39	345	83
24	Little Buffalo Basin			81	61
24	Little Buffalo Basin			240	85
24	Little Buffalo Basin			240	61
24	Little Buffalo Basin			261	47
24	Little Buffalo Basin			38	50
24	Little Buffalo Basin			50	1
24	Little Buffalo Basin			176	18
24	Little Buffalo Basin			104	70
24	Little Buffalo Basin			83	54
24	Little Buffalo Basin			136	8
24	Little Buffalo Basin			135	4
24	Little Buffalo Basin			257	39
25	Little Buffalo Basin	349	12	289	87
25	Little Buffalo Basin			92	90
25	Little Buffalo Basin			99	90
25	Little Buffalo Basin			104	90
25	Little Buffalo Basin			115	88
25	Little Buffalo Basin			95	88
25	Little Buffalo Basin			109	88
25	Little Buffalo Basin			110	90
25	Little Buffalo Basin			275	90
25	Little Buffalo Basin			115	82
25	Little Buffalo Basin			75	90
25	Little Buffalo Basin			197	77
25	Little Buffalo Basin			190	85
25	Little Buffalo Basin			194	75
25	Little Buffalo Basin			187	76
25	Little Buffalo Basin			187	74
25	Little Buffalo Basin			184	86
26	Little Buffalo Basin	282	20	92	79
26	Little Buffalo Basin			80	88
26	Little Buffalo Basin			68	87
26	Little Buffalo Basin			92	78
26	Little Buffalo Basin			115	81
26	Little Buffalo Basin			116	80
26	Little Buffalo Basin			110	82
26	Little Buffalo Basin			109	83
26	Little Buffalo Basin			190	87
26	Little Buffalo Basin			196	85
26	Little Buffalo Basin			17	88
26	Little Buffalo Basin			20	85
26	Little Buffalo Basin			21	86
26	Little Buffalo Basin			20	89
26	Little Buffalo Basin			87	85
26	Little Buffalo Basin			82	81
26	Little Buffalo Basin			76	79
26	Little Buffalo Basin			89	83

Outcrop/ Stereonet #	Anticline	Bedding Dip Direction	Bedding Dip	Fracture Dip Direction	Fracture Dip
27	Little Buffalo Basin	22	16	303	89
27	Little Buffalo Basin			290	82
27	Little Buffalo Basin			298	90
27	Little Buffalo Basin			298	89
27	Little Buffalo Basin			297	89
27	Little Buffalo Basin			303	85
27	Little Buffalo Basin			299	90
27	Little Buffalo Basin			118	82
27	Little Buffalo Basin			221	70
27	Little Buffalo Basin			230	56
27	Little Buffalo Basin			226	71
27	Little Buffalo Basin			200	71
27	Little Buffalo Basin			206	71
27	Little Buffalo Basin			216	78
27	Little Buffalo Basin			283	81
27	Little Buffalo Basin			280	83
28	Grass Creek Anticline	38	23	227	69
28	Grass Creek Anticline			221	68
28	Grass Creek Anticline			219	60
28	Grass Creek Anticline			220	60
28	Grass Creek Anticline			218	56
28	Grass Creek Anticline			218	69
28	Grass Creek Anticline			217	51
28	Grass Creek Anticline			140	90
28	Grass Creek Anticline			277	80
28	Grass Creek Anticline			142	88
28	Grass Creek Anticline			135	81
28	Grass Creek Anticline			129	81
28	Grass Creek Anticline			320	87
29	Grass Creek Anticline	85	22	205	73
29	Grass Creek Anticline			197	78
29	Grass Creek Anticline			17	86
29	Grass Creek Anticline			190	82
29	Grass Creek Anticline			192	82
29	Grass Creek Anticline			190	83
29	Grass Creek Anticline			195	78
29	Grass Creek Anticline			155	80
29	Grass Creek Anticline			133	87
29	Grass Creek Anticline			300	76
29	Grass Creek Anticline			160	89
29	Grass Creek Anticline			141	90
29	Grass Creek Anticline			314	83
29	Grass Creek Anticline			20	85
29	Grass Creek Anticline			12	78
29	Grass Creek Anticline			346	76
29	Grass Creek Anticline			349	85
30	Elk Basin	175	6	276	78
30	Elk Basin			283	76
30	Elk Basin			282	81
30	Elk Basin			289	77
30	Elk Basin			279	73
30	Elk Basin			300	80
30	Elk Basin			290	71

Outcrop/ Stereonet #	Anticline	Bedding Dip Direction	Bedding Dip	Fracture Dip Direction	Fracture Dip
30	Elk Basin			294	79
30	Elk Basin			42	88
30	Elk Basin			16	89
30	Elk Basin			7	73
30	Elk Basin			36	85
30	Elk Basin			45	85
30	Elk Basin			49	82
30	Elk Basin			37	74
30	Elk Basin			50	81
30	Elk Basin			220	90
31	Elk Basin	231	24	84	81
31	Elk Basin			119	71
31	Elk Basin			85	77
31	Elk Basin			95	78
31	Elk Basin			108	88
31	Elk Basin			90	78
31	Elk Basin			91	74
31	Elk Basin			86	71
31	Elk Basin			82	77
31	Elk Basin			135	90
31	Elk Basin			136	90
31	Elk Basin			147	88
31	Elk Basin			320	88
31	Elk Basin			333	87
31	Elk Basin			336	86
31	Elk Basin			128	90
31	Elk Basin			156	90
31	Elk Basin			34	75
31	Elk Basin			27	65
31	Elk Basin			29	73
31	Elk Basin			30	75
32	Elk Basin	326	18	89	84
32	Elk Basin			84	89
32	Elk Basin			78	86
32	Elk Basin			70	87
32	Elk Basin			76	90
32	Elk Basin			85	90
32	Elk Basin			74	87
32	Elk Basin			81	70
32	Elk Basin			78	74
32	Elk Basin			132	85
32	Elk Basin			140	75
32	Elk Basin			139	88
32	Elk Basin			149	88
32	Elk Basin			142	83
32	Elk Basin			138	78
32	Elk Basin			40	78
32	Elk Basin			35	82
33	Elk Basin	274	18	76	82
33	Elk Basin			79	78
33	Elk Basin			75	80
33	Elk Basin			73	83
33	Elk Basin			83	75

Outcrop/ Stereonet #	Anticline	Bedding Dip Direction	Bedding Dip	Fracture Dip Direction	Fracture Dip
33	Elk Basin			76	86
33	Elk Basin			80	80
33	Elk Basin			78	78
33	Elk Basin			72	82
33	Elk Basin			72	75
33	Elk Basin			150	90
33	Elk Basin			155	90
33	Elk Basin			345	81
33	Elk Basin			5	79
33	Elk Basin			154	78
33	Elk Basin			111	64
33	Elk Basin			116	56
33	Elk Basin			116	65
33	Elk Basin			115	62
33	Elk Basin			208	59
33	Elk Basin			354	62
33	Elk Basin			25	54
33	Elk Basin			27	53
34	Elk Basin	315	20	36	89
34	Elk Basin			37	87
34	Elk Basin			213	88
34	Elk Basin			210	84
34	Elk Basin			38	86
34	Elk Basin			34	83
34	Elk Basin			40	90
34	Elk Basin			25	79
34	Elk Basin			43	68
34	Elk Basin			35	75
34	Elk Basin			88	81
34	Elk Basin			93	76
34	Elk Basin			94	78
34	Elk Basin			85	80
34	Elk Basin			68	87
34	Elk Basin			81	81
34	Elk Basin			64	90
34	Elk Basin			66	90
34	Elk Basin			125	63
34	Elk Basin			116	70
34	Elk Basin			114	76
34	Elk Basin			121	90
35	Elk Basin	13	19	243	81
35	Elk Basin			251	80
35	Elk Basin			247	86
35	Elk Basin			248	79
35	Elk Basin			244	69
35	Elk Basin			250	83
35	Elk Basin			244	71
35	Elk Basin			246	82
35	Elk Basin			249	80
35	Elk Basin			249	79
35	Elk Basin			170	65
35	Elk Basin			152	75
35	Elk Basin			152	56

Outcrop/ Stereonet #	Anticline	Bedding Dip Direction	Bedding Dip	Fracture Dip Direction	Fracture Dip
35	Elk Basin			180	68
35	Elk Basin			170	72
35	Elk Basin			176	71
36	Elk Basin	55	33	216	44
36	Elk Basin			213	56
36	Elk Basin			224	70
36	Elk Basin			217	52
36	Elk Basin			216	52
36	Elk Basin			217	40
36	Elk Basin			220	49
36	Elk Basin			218	50
36	Elk Basin			123	83
36	Elk Basin			293	81
36	Elk Basin			124	90
36	Elk Basin			302	78
36	Elk Basin			137	80
36	Elk Basin			310	89
37	Elk Basin	275	9	306	77
37	Elk Basin			306	65
37	Elk Basin			336	74
37	Elk Basin			322	77
37	Elk Basin			318	81
37	Elk Basin			225	90
37	Elk Basin			224	90
37	Elk Basin			41	83
37	Elk Basin			252	80
38	Elk Basin	115	13	29	81
38	Elk Basin			24	85
38	Elk Basin			20	80
38	Elk Basin			21	83
38	Elk Basin			24	85
38	Elk Basin			28	77
38	Elk Basin			34	80
38	Elk Basin			23	84
38	Elk Basin			318	71
38	Elk Basin			313	79
38	Elk Basin			330	80
38	Elk Basin			324	90
38	Elk Basin			299	78
38	Elk Basin			316	81
39	Garland Basin	223	14	62	89
39	Garland Basin			65	76
39	Garland Basin			64	76
39	Garland Basin			51	78
39	Garland Basin			243	86
39	Garland Basin			69	82
39	Garland Basin			236	89
39	Garland Basin			75	76
39	Garland Basin			76	80
39	Garland Basin			66	82
40	Garland Basin	230	20	236	90
40	Garland Basin			58	82
40	Garland Basin			57	87

Outcrop/ Stereonet #	Anticline	Bedding Dip Direction	Bedding Dip	Fracture Dip Direction	Fracture Dip
40	Garland Basin			49	89
40	Garland Basin			236	89
40	Garland Basin			58	90
40	Garland Basin			259	83
40	Garland Basin			263	80
40	Garland Basin			62	88
40	Garland Basin			55	81
40	Garland Basin			213	21
40	Garland Basin			212	18
40	Garland Basin			163	31
40	Garland Basin			156	30
40	Garland Basin			150	34
40	Garland Basin			175	28
41	Garland Basin	250	17	228	90
41	Garland Basin			232	90
41	Garland Basin			232	89
41	Garland Basin			237	89
41	Garland Basin			50	80
41	Garland Basin			44	75
41	Garland Basin			50	83
41	Garland Basin			236	78
41	Garland Basin			234	80
41	Garland Basin			53	82
41	Garland Basin			72	73
41	Garland Basin			250	82
41	Garland Basin			76	88
41	Garland Basin			253	88
41	Garland Basin			81	84
41	Garland Basin			114	74
41	Garland Basin			114	84
41	Garland Basin			97	90
42	Garland Basin	85	2	43	84
42	Garland Basin			48	83
42	Garland Basin			44	83
42	Garland Basin			55	89
42	Garland Basin			60	86
42	Garland Basin			52	86
42	Garland Basin			50	80
42	Garland Basin			52	87
42	Garland Basin			52	81
42	Garland Basin			284	87
42	Garland Basin			106	76
42	Garland Basin			111	63
42	Garland Basin			87	88
42	Garland Basin			142	88
42	Garland Basin			325	86
43	Garland Basin	39	23	223	58
43	Garland Basin			222	63
43	Garland Basin			216	63
43	Garland Basin			219	72
43	Garland Basin			227	52
43	Garland Basin			218	62
43	Garland Basin			216	61

Outcrop/ Stereonet #	Anticline	Bedding Dip Direction	Bedding Dip	Fracture Dip Direction	Fracture Dip
43	Garland Basin			226	70
43	Garland Basin			123	82
43	Garland Basin			127	87
43	Garland Basin			143	85
43	Garland Basin			105	85
43	Garland Basin			130	80
44	Garland Basin	27	18	315	84
44	Garland Basin			301	87
44	Garland Basin			320	87
44	Garland Basin			318	89
44	Garland Basin			319	82
44	Garland Basin			153	75
44	Garland Basin			308	87
44	Garland Basin			230	71
44	Garland Basin			226	75
44	Garland Basin			243	88
44	Garland Basin			247	74
44	Garland Basin			256	87
44	Garland Basin			248	84
45	Garland Basin	46	50	133	87
45	Garland Basin			328	80
45	Garland Basin			315	83
45	Garland Basin			310	76
45	Garland Basin			307	88
45	Garland Basin			317	86
45	Garland Basin			300	84
45	Garland Basin			302	84
45	Garland Basin			298	-8
45	Garland Basin			308	85
45	Garland Basin			226	50
45	Garland Basin			227	61
45	Garland Basin			223	41
45	Garland Basin			206	56
45	Garland Basin			207	40
46	Garland Basin	52	54	111	88
46	Garland Basin			294	85
46	Garland Basin			297	80
46	Garland Basin			296	84
46	Garland Basin			302	79
46	Garland Basin			301	86
46	Garland Basin			294	81
46	Garland Basin			307	85
46	Garland Basin			292	82
46	Garland Basin			292	84
46	Garland Basin			205	60
46	Garland Basin			201	49
46	Garland Basin			197	52
46	Garland Basin			195	50
46	Garland Basin			210	61
46	Garland Basin			198	48
46	Garland Basin			259	38
46	Garland Basin			230	58
46	Garland Basin			266	43

Outcrop/ Stereonet #	Anticline	Bedding Dip Direction	Bedding Dip	Fracture Dip Direction	Fracture Dip
46	Garland Basin			183	60
46	Garland Basin			184	64
47	Garland Basin	45	46	259	64
47	Garland Basin			267	81
47	Garland Basin			290	86
47	Garland Basin			249	72
47	Garland Basin			257	78
47	Garland Basin			265	70
47	Garland Basin			262	83
47	Garland Basin			261	72
47	Garland Basin			245	78
47	Garland Basin			152	72
47	Garland Basin			155	80
47	Garland Basin			145	71
47	Garland Basin			172	50
47	Garland Basin			168	52
48	Manderson Anticline	260	8	15	84
48	Manderson Anticline			23	80
48	Manderson Anticline			213	79
48	Manderson Anticline			49	78
48	Manderson Anticline			44	76
48	Manderson Anticline			35	90
48	Manderson Anticline			0	76
48	Manderson Anticline			23	82
48	Manderson Anticline			11	73
48	Manderson Anticline			68	88
48	Manderson Anticline			341	86
48	Manderson Anticline			60	70
48	Manderson Anticline			324	89
48	Manderson Anticline			115	82
48	Manderson Anticline			78	83
48	Manderson Anticline			254	82
48	Manderson Anticline			242	85
48	Manderson Anticline			302	89
48	Manderson Anticline			21	80
49	Manderson Anticline	305	22	41	81
49	Manderson Anticline			18	85
49	Manderson Anticline			35	89
49	Manderson Anticline			220	89
49	Manderson Anticline			47	80
49	Manderson Anticline			144	70
49	Manderson Anticline			137	80
49	Manderson Anticline			201	90
49	Manderson Anticline			85	83
49	Manderson Anticline			313	75
49	Manderson Anticline			30	90
49	Manderson Anticline			25	87
49	Manderson Anticline			16	90
49	Manderson Anticline			21	86
49	Manderson Anticline			34	87
49	Manderson Anticline			130	89
50	Manderson Anticline	328	3	195	77
50	Manderson Anticline			204	89

Outcrop/ Stereonet #	Anticline	Bedding Dip Direction	Bedding Dip	Fracture Dip Direction	Fracture Dip
50	Manderson Anticline			196	88
50	Manderson Anticline			197	90
50	Manderson Anticline			160	89
50	Manderson Anticline			348	87
50	Manderson Anticline			335	86
50	Manderson Anticline			198	90
50	Manderson Anticline			13	84
50	Manderson Anticline			6	87
50	Manderson Anticline			106	85
51	Manderson Anticline	10	28	240	77
51	Manderson Anticline			250	89
51	Manderson Anticline			247	85
51	Manderson Anticline			250	86
51	Manderson Anticline			240	82
51	Manderson Anticline			242	73
51	Manderson Anticline			241	88
51	Manderson Anticline			156	71
51	Manderson Anticline			161	82
51	Manderson Anticline			164	88
51	Manderson Anticline			356	78
51	Manderson Anticline			133	78
52	Manderson Anticline	8	16	210	84
52	Manderson Anticline			210	83
52	Manderson Anticline			216	78
52	Manderson Anticline			208	78
52	Manderson Anticline			206	82
52	Manderson Anticline			210	78
52	Manderson Anticline			203	78
52	Manderson Anticline			208	85
52	Manderson Anticline			204	63
52	Manderson Anticline			206	74
52	Manderson Anticline			210	72
52	Manderson Anticline			204	74
52	Manderson Anticline			195	75
52	Manderson Anticline			214	78
52	Manderson Anticline			237	75
52	Manderson Anticline			236	80
52	Manderson Anticline			233	80
52	Manderson Anticline			230	72
52	Manderson Anticline			233	65
52	Manderson Anticline			236	69
52	Manderson Anticline			302	78
52	Manderson Anticline			110	81
52	Manderson Anticline			300	90
52	Manderson Anticline			303	90
52	Manderson Anticline			121	87
52	Manderson Anticline			296	87
53	Manderson Anticline	49	52	212	43
53	Manderson Anticline			228	39
53	Manderson Anticline			220	34
53	Manderson Anticline			230	37
53	Manderson Anticline			226	33
53	Manderson Anticline			233	33

Outcrop/ Stereonet #	Anticline	Bedding Dip Direction	Bedding Dip	Fracture Dip Direction	Fracture Dip
53	Manderson Anticline			225	29
53	Manderson Anticline			222	32
53	Manderson Anticline			147	79
53	Manderson Anticline			306	74
53	Manderson Anticline			312	85
53	Manderson Anticline			118	85
53	Manderson Anticline			133	88
53	Manderson Anticline			124	78
54	Manderson Anticline	82	16	236	78
54	Manderson Anticline			239	61
54	Manderson Anticline			243	77
54	Manderson Anticline			235	81
54	Manderson Anticline			250	48
54	Manderson Anticline			152	88
54	Manderson Anticline			151	85
54	Manderson Anticline			150	83
54	Manderson Anticline			320	72
55	Manderson Anticline	60	41	241	42
55	Manderson Anticline			240	39
55	Manderson Anticline			233	44
55	Manderson Anticline			245	45
55	Manderson Anticline			251	38
55	Manderson Anticline			248	42
55	Manderson Anticline			238	42
55	Manderson Anticline			243	47
55	Manderson Anticline			329	82
55	Manderson Anticline			131	85
55	Manderson Anticline			323	90
55	Manderson Anticline			160	78
55	Manderson Anticline			320	90
56	Tensleep Anticline	217	30	37	64
56	Tensleep Anticline			40	57
56	Tensleep Anticline			41	57
56	Tensleep Anticline			44	57
56	Tensleep Anticline			38	53
56	Tensleep Anticline			39	54
56	Tensleep Anticline			35	62
56	Tensleep Anticline			38	51
56	Tensleep Anticline			35	62
56	Tensleep Anticline			45	40
56	Tensleep Anticline			40	38
56	Tensleep Anticline			125	90
56	Tensleep Anticline			133	90
56	Tensleep Anticline			130	88
56	Tensleep Anticline			311	88
56	Tensleep Anticline			308	88
56	Tensleep Anticline			310	88
57	Tensleep Anticline	75	13	205	88
57	Tensleep Anticline			211	79
57	Tensleep Anticline			219	76
57	Tensleep Anticline			212	79
57	Tensleep Anticline			203	90
57	Tensleep Anticline			215	85

Outcrop/ Stereonet #	Anticline	Bedding Dip Direction	Bedding Dip	Fracture Dip Direction	Fracture Dip
57	Tensleep Anticline			208	82
57	Tensleep Anticline			138	87
57	Tensleep Anticline			128	82
57	Tensleep Anticline			129	85
57	Tensleep Anticline			118	84
57	Tensleep Anticline			127	84
58	Tensleep Anticline	236	7	225	74
58	Tensleep Anticline			226	77
58	Tensleep Anticline			220	79
58	Tensleep Anticline			225	81
58	Tensleep Anticline			227	87
58	Tensleep Anticline			225	88
58	Tensleep Anticline			218	73
58	Tensleep Anticline			223	77
58	Tensleep Anticline			322	82
58	Tensleep Anticline			126	86
58	Tensleep Anticline			124	86
58	Tensleep Anticline			125	87
58	Tensleep Anticline			125	83
58	Tensleep Anticline			118	85
58	Tensleep Anticline			165	87
58	Tensleep Anticline			170	82
59	Tensleep Anticline	83	1	16	81
59	Tensleep Anticline			29	82
59	Tensleep Anticline			355	79
59	Tensleep Anticline			35	85
59	Tensleep Anticline			12	87
59	Tensleep Anticline			0	79
59	Tensleep Anticline			120	79
59	Tensleep Anticline			305	87
59	Tensleep Anticline			122	86
59	Tensleep Anticline			115	90
59	Tensleep Anticline			295	86
59	Tensleep Anticline			239	90
59	Tensleep Anticline			238	90
59	Tensleep Anticline			245	77
59	Tensleep Anticline			247	78
60	Tensleep Anticline	258	59	91	51
60	Tensleep Anticline			80	50
60	Tensleep Anticline			75	55
60	Tensleep Anticline			83	56
60	Tensleep Anticline			84	44
60	Tensleep Anticline			75	43
60	Tensleep Anticline			85	48
60	Tensleep Anticline			88	46
60	Tensleep Anticline			352	79
60	Tensleep Anticline			356	68
60	Tensleep Anticline			338	75
60	Tensleep Anticline			354	68
60	Tensleep Anticline			345	82
60	Tensleep Anticline			356	73
60	Tensleep Anticline			115	56
60	Tensleep Anticline			136	66

Outcrop/ Stereonet #	Anticline	Bedding Dip Direction	Bedding Dip	Fracture Dip Direction	Fracture Dip
61	Thermopolis Anticline	217	47	5	72
61	Thermopolis Anticline			6	82
61	Thermopolis Anticline			5	64
61	Thermopolis Anticline			345	55
61	Thermopolis Anticline			2	72
61	Thermopolis Anticline			355	74
61	Thermopolis Anticline			345	61
61	Thermopolis Anticline			355	63
61	Thermopolis Anticline			1	66
61	Thermopolis Anticline			340	64
61	Thermopolis Anticline			356	68
61	Thermopolis Anticline			336	51
61	Thermopolis Anticline			108	45
61	Thermopolis Anticline			135	88
61	Thermopolis Anticline			91	64
61	Thermopolis Anticline			76	61
61	Thermopolis Anticline			6	63
61	Thermopolis Anticline			335	58
61	Thermopolis Anticline			338	64
61	Thermopolis Anticline			54	58
62	Thermopolis Anticline	27	18	167	78
62	Thermopolis Anticline			150	81
62	Thermopolis Anticline			153	80
62	Thermopolis Anticline			157	84
62	Thermopolis Anticline			150	84
62	Thermopolis Anticline			157	90
62	Thermopolis Anticline			153	87
62	Thermopolis Anticline			156	90
62	Thermopolis Anticline			156	86
62	Thermopolis Anticline			164	90
62	Thermopolis Anticline			165	89
62	Thermopolis Anticline			151	86
62	Thermopolis Anticline			236	85
62	Thermopolis Anticline			240	82
62	Thermopolis Anticline			240	74
62	Thermopolis Anticline			235	70
62	Thermopolis Anticline			235	87
62	Thermopolis Anticline			237	86
63	Thermopolis Anticline	106	16	159	89
63	Thermopolis Anticline			164	87
63	Thermopolis Anticline			156	82
63	Thermopolis Anticline			161	88
63	Thermopolis Anticline			161	86
63	Thermopolis Anticline			162	88
63	Thermopolis Anticline			165	84
63	Thermopolis Anticline			165	87
63	Thermopolis Anticline			258	89
63	Thermopolis Anticline			252	74
63	Thermopolis Anticline			247	90
63	Thermopolis Anticline			250	85
63	Thermopolis Anticline			236	85
64	Thermopolis Anticline	140	17	236	70
64	Thermopolis Anticline			235	76

Outcrop/ Stereonet #	Anticline	Bedding Dip Direction	Bedding Dip	Fracture Dip Direction	Fracture Dip
64	Thermopolis Anticline			237	66
64	Thermopolis Anticline			270	75
64	Thermopolis Anticline			139	79
64	Thermopolis Anticline			130	72
64	Thermopolis Anticline			142	79
64	Thermopolis Anticline			140	68
65	Thermopolis Anticline	169	7	201	82
65	Thermopolis Anticline			208	69
65	Thermopolis Anticline			194	78
65	Thermopolis Anticline			15	84
65	Thermopolis Anticline			199	74
65	Thermopolis Anticline			142	74
65	Thermopolis Anticline			95	75
66	Thermopolis Anticline	12	21	196	78
66	Thermopolis Anticline			185	70
66	Thermopolis Anticline			196	65
66	Thermopolis Anticline			203	70
66	Thermopolis Anticline			206	57
66	Thermopolis Anticline			128	87
66	Thermopolis Anticline			286	77
66	Thermopolis Anticline			277	80
66	Thermopolis Anticline			110	58
66	Thermopolis Anticline			188	74
67	Thermopolis Anticline	240	15	166	88
67	Thermopolis Anticline			174	78
67	Thermopolis Anticline			167	84
67	Thermopolis Anticline			168	80
67	Thermopolis Anticline			172	82
67	Thermopolis Anticline			284	88
67	Thermopolis Anticline			75	90
67	Thermopolis Anticline			85	89
68	Thermopolis Anticline	191	65	316	47
68	Thermopolis Anticline			323	50
68	Thermopolis Anticline			314	70
68	Thermopolis Anticline			302	39
68	Thermopolis Anticline			275	42
68	Thermopolis Anticline			308	36
68	Thermopolis Anticline			302	40
68	Thermopolis Anticline			312	42